


Forschungsberichte  
aus dem



**Institut für Werkstofftechnik  
Metallische Werkstoffe**

der **U N I K A S S E L  
V E R S I T Ä T**

Herausgeber: Prof. Dr.-Ing. T. Niendorf  
Prof. Dr.-Ing. B. Scholtes

kassel  
university   
press

Band 29

Arnaud Magnier

**Residual stress analysis in polymer materials  
using the hole drilling method – basic principles  
and applications**

Forschungsberichte  
aus dem



**Institut für Werkstofftechnik  
Metallische Werkstoffe**

der

**U N I K A S S E L  
V E R S I T Ä T**

Herausgeber: Prof. Dr.-Ing. T. Niendorf  
Prof. Dr.-Ing. B. Scholtes

---

Band 29

Arnaud Magnier

**Residual stress analysis in polymer materials  
using the hole drilling method – basic principles  
and applications**

Forschungsberichte aus dem Institut für Werkstofftechnik - Metallische Werkstoffe  
der Universität Kassel  
Band 29

Herausgeber:

Prof. Dr.-Ing. T. Niendorf  
Prof. Dr.-Ing. B. Scholtes  
Institut für Werkstofftechnik  
Metallische Werkstoffe  
Universität Kassel  
Mönchebergstr. 3  
34109 Kassel

Die vorliegende Arbeit wurde vom Fachbereich Maschinenbau der Universität Kassel  
als Dissertation zur Erlangung des akademischen Grades eines Doktors der  
Ingenieurwissenschaften (Dr.-Ing.) angenommen.

Erster Gutachter: Prof. Dr.-Ing. habil. Berthold Scholtes  
Zweiter Gutachter: Prof. Dr. rer. nat. Thomas Tröster  
Tag der mündlichen Prüfung: 15. Oktober 2018

Bibliografische Information der Deutschen Nationalbibliothek  
Die Deutsche Nationalbibliothek verzeichnet diese Publikation in der Deutschen  
Nationalbibliografie; detaillierte bibliografische Daten sind im Internet über  
<http://dnb.ddb.de> abrufbar

Zugl.: Kassel, Univ., Diss. 2018  
ISBN 978-3-7376-0644-8 (print)  
ISBN 978-3-7376-0645-5 (e-book)  
DOI: <http://dx.medra.org/10.19211/KUP9783737606455>  
URN: <https://nbn-resolving.org/urn:nbn:de:0002-406459>

© 2019, kassel university press GmbH, Kassel  
[www.upress.uni-kassel.de](http://www.upress.uni-kassel.de)

Druck und Verarbeitung: docupoint GmbH, Barleben  
Printed in Germany

## **Vorwort der Herausgeber**

Bei einer zunehmenden Verbreitung elektronischer Medien kommt dem gedruckten Fachbericht auch weiterhin eine große Bedeutung zu. In der vorliegenden Reihe werden deshalb wichtige Forschungsarbeiten präsentiert, die am Institut für Werkstofftechnik – Metallische Werkstoffe der Universität Kassel gewonnen wurden. Das Institut kommt damit auch – neben der Publikationstätigkeit in Fachzeitschriften – seiner Verpflichtung nach, über seine Forschungsaktivitäten Rechenschaft abzulegen und die Resultate der interessierten Öffentlichkeit kenntlich und nutzbar zu machen.

Allen Institutionen, die durch Sach- und Personalmittel die durchgeführten Forschungsarbeiten unterstützen, sei an dieser Stelle verbindlich gedankt.

Kassel, im Dezember 2018

**Prof. Dr.-Ing. T. Niendorf**

**Prof. Dr.-Ing. habil. B. Scholtes**



## Table of Contents

|       |   |    |
|-------|---|----|
| 1     | Introduction .....  | 1  |
| 2     | State of the art .....  | 3  |
| 2.1   | Formation of residual stresses in polymer materials.....                    | 4  |
| 2.1.1 | Formation of residual stresses in injection moulded polymer materials ..... | 4  |
| 2.1.2 | Formation of residual stresses in heterogeneous materials .....             | 8  |
| 2.1.3 | Conclusion .....  | 10 |
| 2.2   | Standard methods for measuring residual stresses.....                       | 11 |
| 2.2.1 | X-ray diffraction.....  | 11 |
| 2.2.2 | Layer removal method.....   | 12 |
| 2.2.3 | Photoelastic stress analysis.....   | 13 |
| 2.2.4 | The hole drilling method .....  | 13 |
| 2.3   | The integral hole drilling method.....                                      | 14 |
| 2.3.1 | Principle.....  | 15 |
| 2.3.2 | Isotropic material .....  | 18 |
| 2.3.3 | Anisotropic or orthotropic material.....                                    | 21 |
| 2.3.4 | Influence of the geometry, case of a sample with a welded joint .....       | 22 |
| 2.4   | Conclusion.....   | 24 |
| 3     | Determination of calibration matrices.....                                  | 25 |
| 3.1   | Calculation of coefficients for the isotropic case.....                     | 25 |
| 3.1.1 | Determining the displacement and strain field for any load case.....        | 26 |
| 3.1.2 | Calculation of the matrix <b>a</b> .....                                    | 29 |
| 3.1.3 | Calculation of the matrix <b>b</b> .....                                    | 29 |
| 3.2   | Calculation of coefficients for orthotropic materials .....                 | 30 |
| 3.3   | Calculation of coefficients for hybrid structures.....                      | 31 |
| 3.3.1 | Example 1: Hybrid structure .....   | 32 |
| 3.3.2 | Example 2: Semi-crystalline material .....                                  | 32 |
| 3.4   | Important parameters for the simulation .....                               | 34 |
| 3.4.1 | Thickness of the sample .....   | 34 |
| 3.4.2 | Poisson's ratio.....  | 36 |
| 3.4.3 | Model equivalence.....  | 36 |
| 3.5   | Conclusion.....   | 37 |

|       |   |     |
|-------|---|-----|
| 4     | Elaboration of appropriate measuring strategies for polymer materials.....                                  | 38  |
| 4.1   | Required accuracy of the measurement .....  | 39  |
| 4.2   | Experimental set-up and sample preparation .....  | 40  |
| 4.3   | Influencing factors.....  | 42  |
| 4.3.1 | Influence of thermal fluctuations during the experiment .....   | 42  |
| 4.3.2 | Influence of mechanical loading during measuring operations.....  | 45  |
| 4.3.3 | Setting the zero depth and stress in the bonding strain gauge / sample .....                                | 48  |
| 4.3.4 | Stiffening effects.....   | 51  |
| 4.4   | Evaluation procedure to take into account time dependent effects.....                                       | 54  |
| 4.5   | Conclusion.....   | 59  |
| 5     | Application of the hole drilling method on polymer materials.....   | 60  |
| 5.1   | Reproducibility of the measurement .....  | 60  |
| 5.1.1 | Injection moulded polycarbonate .....   | 60  |
| 5.1.2 | Transmission laser welded polypropylene structure .....   | 68  |
| 5.1.3 | Reinforced polypropylene .....  | 78  |
| 5.2   | Free quenching .....  | 81  |
| 5.2.1 | Polycarbonate .....   | 81  |
| 5.2.2 | Polypropylene.....  | 82  |
| 5.3   | Quantitative validation and influence of residual stresses .....  | 84  |
| 5.3.1 | Bending of a 4 mm thick polycarbonate sample .....  | 85  |
| 5.3.2 | Influence of residual stresses on environmental stress cracking.....  | 90  |
| 5.3.3 | Bending of a 3 mm thick polypropylene sample.....   | 91  |
| 5.3.4 | Bending of a 4 mm thick self-reinforced polypropylene composite.....  | 94  |
| 5.4   | Residual stress measurement in an hybrid structure made of aluminium and of a reinforced polypropylene..... | 95  |
| 5.4.1 | Measurement validation in thin metal sheet.....   | 96  |
| 5.4.2 | Measurements in the hybrid structure .....  | 98  |
| 6     | Conclusion and outlook.....   | 101 |

## 1 Introduction

Residual stresses are mechanical stresses in materials free of external loads, moments or temperature gradients. These residual stresses form a self-equilibrated and inhomogeneous stress state, which is then superimposed upon external stresses applied to the material. A distinction is made between macroscopic residual stresses, which are comparable to loading stresses, and microscopic residual stresses, which take the inhomogeneous microstructure of materials into account. In polymer materials, residual stresses are generally produced during the processing phase due to changing pressure history and inhomogeneous cooling [Jansen 1994].

Residual stresses are mostly unwanted in polymer materials, because they induce geometrical changes, such as warpage. These deformations can be predicted with finite element analysis. Residual stresses also play a role in the mechanical integrity of workpieces. In fact, they influence the stress field around a crack [Subramanyam Reddy 2016], and even small amounts of residual stresses can cause early defects, for example, in pressurized polymer pipelines [Hutař 2013]. Moreover, tensile loads and tensile residual stresses are known to have a high tendency to crack when exposed to an aggressive chemical environment [Turnbull 1999]. Since this environmental stress cracking is one of the most frequently occurring failures in polymer materials [Jansen 2005, Klein 2016], it is necessary to be able to measure residual stresses to better predict the lifetime of products. For example, in medical devices, the intensive use of chemicals can lead to cracks on the surface of components. Inducing compressive residual stresses near the surface of components could be an effective way to increase the resistance to environmental stress cracking, by limiting the influence of possible external tensile loads (see also Figure 5.25). Therefore, residual stresses can also have positive effects on the mechanical properties of polymer materials. Altogether, residual stress measurements are needed to validate results from finite element analysis and to predict the short-term and long-term mechanical behaviour of products.

Different methods exist to measure residual stresses in polymer materials (chapter 2.2). Good results have been achieved with the layer removal method in the last decades [Jansen 1994]. However, because workpieces often have complex geometries, the use of the layer removal method is restricted, which, in turn, makes developing a method applicable for most product designs essential. The hole drilling method has high potential to fulfil this criterion [Garcia Sobolevski 2007, Nau 2015]. Furthermore, it can be used for numerous material classes, such as amorphous, semi-crystalline and composite structures. The standard norm [ASTM 2013] describes the integral hole drilling method, though it is only applicable for thick isotropic materials. Chapter 2.3 focuses on the theoretical mechanical basis of this method, an extension is also



proposed for general applications. Advice is provided for efficiently obtaining coefficients for correlating measured strains during an experiment and residual stresses. These coefficients were obtained with finite element analysis described in chapter 3.

However, even if the hole drilling method is well-known for its application on metallic materials, measurements performed on polymer materials are not straightforward and often lead to worse results than the layer removal method [Turnbull 1999, Kim 2007]. Indeed, the hole drilling method cannot be used without modification. Chapter 4 will illustrate how the measurement set-up needs to be adapted for polymer materials. Moreover, effects like the viscoelastic behaviour and the temperature sensitivity of the material must be taken into account during strain measurements. A thorough analysis of influencing factors is indispensable for finding the main sources of errors and in order to assess the accuracy of the proposed method (chapter 4).

After developing a reliable strain measurement method, residual stresses can be calculated. Chapter 5 focuses upon the reproducibility and the validity of results for different classes of materials: amorphous and isotropic (i.e., polycarbonate), semi-crystalline and isotropic (i.e., polypropylene), and orthotropic (i.e., the self-reinforced polypropylene composite PURE) [Heim 2014]. These materials exhibit differences regarding their stiffness, surface structure, thermal property and their viscoelastic behaviour, which is why different criteria must be investigated regarding the limitation of the hole drilling method. The results will be applicable for the various classes of materials. Different processing parameters were applied for polycarbonate and polypropylene structures and their respective influences on residual stresses were examined. Further investigations were performed using hybrid structures composed of two layers of aluminium and the composite PURE. In this case, high residual stresses were expected since both materials have different thermo-mechanical properties.

## 2 State of the art

In this chapter, the important aspects of the formation of residual stresses in polymer materials and composite materials are described. The following materials were focused upon: two thermoplastics, a polycarbonate and a polypropylene (both were processed with injection moulding), and a self-reinforced polypropylene composite structure [Heim 2014]. Different difficulties are expected for these materials. Polycarbonate is an amorphous thermoplastic with which it is possible to investigate the potential of the hole drilling method where other methods like X-ray diffraction fail (see chapter 2.2.1). Polypropylene is also a thermoplastic material, however, it is semi-crystalline. Due to the difference in crystallinity and spherulite sizes in the material, heterogeneous elastic properties are expected which may influence results. Polypropylene and polycarbonate share a similar level of stiffness with widespread classes of materials. The analysis and the validity of measurements can be extended to other materials with stiffness in between these two reference materials ( $E = 1300$  MPa for polypropylene;  $E = 2300$  MPa for polycarbonate). Stiffer self-reinforced polypropylene composites ( $E = 5500$  MPa) are not expected to be more challenging regarding their stiffness, however their wavy structure may not be suitable for the application of the hole drilling method (chapter 4.3.4). Furthermore, this material is orthotropic, which represents an additional problem for the standard hole drilling method formalism (chapter 2.3.3).

During the production process of these materials, different steps contribute greatly to the final residual stress state in the material. This chapter does not intend to provide an exhaustive list of residual stress formation mechanisms. It will instead highlight the main effects expected to contribute to the formation of residual stresses in the investigated materials. Different scales of residual stresses are shown: macroscopic residual stresses, such as thermally induced residual stresses in a sample during the cooling phase; microscopic residual stresses, such as the binding between fibre and matrix in composite materials. The fact that thermal effects are not the only cause for residual stresses is illustrated. Other sources, such as fluctuating pressure during the solidification phase, contribute to residual stresses.

Subsequently, various methods will be proposed to measure the residual stresses. The physics and mechanics of these methods will be explained. They differ in relation to the measured volumes and phases (crystal structure, amorphous structure, fibre), so that results are not necessarily comparable. For example, in the case of a semi-crystalline material, the use of x-ray diffraction will only offer information in the crystalline phase, whereas mechanical methods, such as the hole drilling method, will measure an average residual stress between the amorphous phase and the crystalline phase. For more information, detailed reviews are available concerning residual stresses in injection moulded samples [Guevara-Morales 2014] and residual stresses in thermoplastic composites [Parlevliet 2006, Shokrieh 2014].

## 2.1 Formation of residual stresses in polymer materials

### 2.1.1 Formation of residual stresses in injection moulded polymer materials

In this section, the development of residual stresses during the injection moulding process is shown. Two materials were produced using this process: a polypropylene and a polycarbonate. The main mechanisms, such as quenching induced residual stresses, are not inherent to injection moulding alone and can be correlated with other processes like polymer extrusion. For simplification, all materials are considered homogeneous, that is, property gradients in the material are neglected. Material heterogeneity is dealt with in-depth in chapter 2.2.

#### 2.1.1.1 Quenching induced residual stresses

The most well-known model for generating residual stresses in polymer materials is free quenching of a sample using a skin-core model. In this model, pre-heating is performed above the “solidification” temperature  $T_s$ : the glass temperature for amorphous material and the melting temperature for semi-crystalline material. It is assumed that the material behaves like a fluid above  $T_s$  and like a linear elastic solid below  $T_s$ . This means, the viscoelastic behaviour of the polymer material is not considered in this model. Furthermore, the dependency of the material’s elastic coefficient upon the temperature is greatly simplified. The Young’s modulus is a constant below  $T_s$  and is zero above  $T_s$ . Residual stress build-up is due to differences in cooling rates inside the material, and due to the material’s mechanical properties dependency with temperature. In the following section, residual stresses are considered to be uniaxial for the purpose of simplification.

During cooling, the surface of the material begins to solidify while in contact with the external environment, forming a skin; in Figure 2.1 this skin is layer “A”. This solidification is followed by shrinkage of the volume of the skin. The core of the material does not affect the shrinkage of the skin as it is still hot and behaves like a fluid. In other words, the core doesn’t bring any resistance to deformation initially. Later, the core of the material cools below  $T_s$  and shrinks. Since the skin has already solidified, it interferes with the volume variation of the core. As the volume reduction is restrained, the core stays in a locked, stretched state. Therefore, tensile residual stresses are formed in the core. In contrast, compressive residual stresses appear on the surface and balance out the tensile residual stresses in the core.

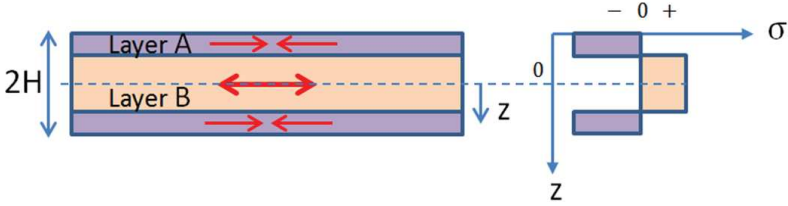


**Figure 2.1** Simplified residual stress state after free quenching: skin-core model.

This model is already questionable for semi-crystalline material. Indeed, if the material cools fast enough, no crystalline structure develops on the surface, leaving it amorphous. It results in an even more complex formation of residual stresses, because the amorphous phase and the semi-crystalline phase behave differently. As long as the amorphous skin is thin (0.03 mm in Figure 2.5), the model is globally applicable. Amorphous and semi-crystalline components exhibit viscoelastic behaviour, meaning part of the residual stresses in the material should relax to a certain degree over time. Moreover, crystallisation is followed by volume changes which also influence the end result.

It is actually possible to achieve a better description of the residual stresses induced in a component caused by varying cooling rates by evaluating the cross-section of the material with thermo-viscoelastic theory. The assumptions are the same as before. The material behaves like a fluid above  $T_s$  and like a homogeneous, linear, elastic solid below  $T_s$ . Cooling of the material is symmetric and is caused by contact with external sources. Both sides of the material cool down the same. A theoretical parabolic form of the residual stress distribution can then be obtained with the following formula [Struik 1978]:

$$\sigma(z) = \frac{\alpha E}{1-\nu} \cdot (T_g - T_f) \cdot m \cdot \frac{1}{6} \left[ 1 - 3 \left( \frac{z}{H} \right)^2 \right] \quad (2.1)$$

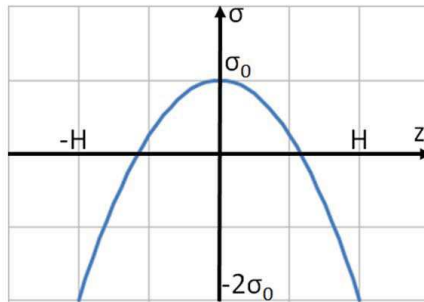


**Figure 2.2** Theoretical residual stress profile after quenching a polymer material using equation 2.1.

Equation (2.1) describes a residual stress state with compressive residual stresses near the surface and tensile residual stresses in the core. There is a factor of two between the maximum compressive and tensile residual stresses. This equation is convenient as it depends only on few parameters: the thermal expansion coefficient  $\alpha$ , Young's modulus  $E$ , Poisson's ratio  $\nu$ , the glass and final temperature  $T_g$  and  $T_f$ , the Biot number  $m$ , and the thickness  $2H$  of the sample. Similar residual stress profiles have been measured in this study after quenching of polycarbonate samples (chapter 5.2.1).

In conclusion, cooling residual stresses occur after inhomogeneous cooling of a component partly due to the material stiffness dependent upon the temperature. This mechanism is similar to the model used for metals, however, cooling residual stresses are more closely related to plastic deformations in this case and the dependency of the yield stress on the temperature. Mechanisms can be seen in [Gibmeier and Scholtes 2016]. In both cases, compressive residual stresses are induced near the surface and tensile residual stresses are present in the core.

#### **2.1.1.2 Pressure-induced residual stresses**

During the injection moulding process, the polymer melt solidifies at different pressures, which also leads to residual stresses in the product [Jansen 1994, 1996]. In Figure 2.3a the course of the cavity pressure during injection moulding can be seen. At first, layer "A" solidifies during the filling phase as it comes into contact with the low temperature of the mould. After the filling phase, the polymer melt is packed at high pressure. This high pressure is held and a loss in volume caused by the shrinkage resulting from the decreasing temperature is compensated by additional melt entering the cavity. The cavity pressure continues to decrease as the temperature does. There are three layers: layer A which solidifies at low pressure; layer B which solidifies at high holding pressure; core C which solidifies at continuously decreasing pressure. If all layers solidified at the same pressure, they would have undergone the same extension after ejection, as the pressure reduced to room pressure. In reality, layer B should extend more after ejection due to its high level of retained pressure (dashed line in figure 2.3d). However, because the surface and the core solidified at a lower pressure, they restrain the extension of layer B. Therefore, layer B remains in a retained, compressed state, and, in doing so, compressive residual stresses are locked in layer B and tensile residual stresses in layers A and C in order to establish a stress equilibrium, see Figure 2.3c.

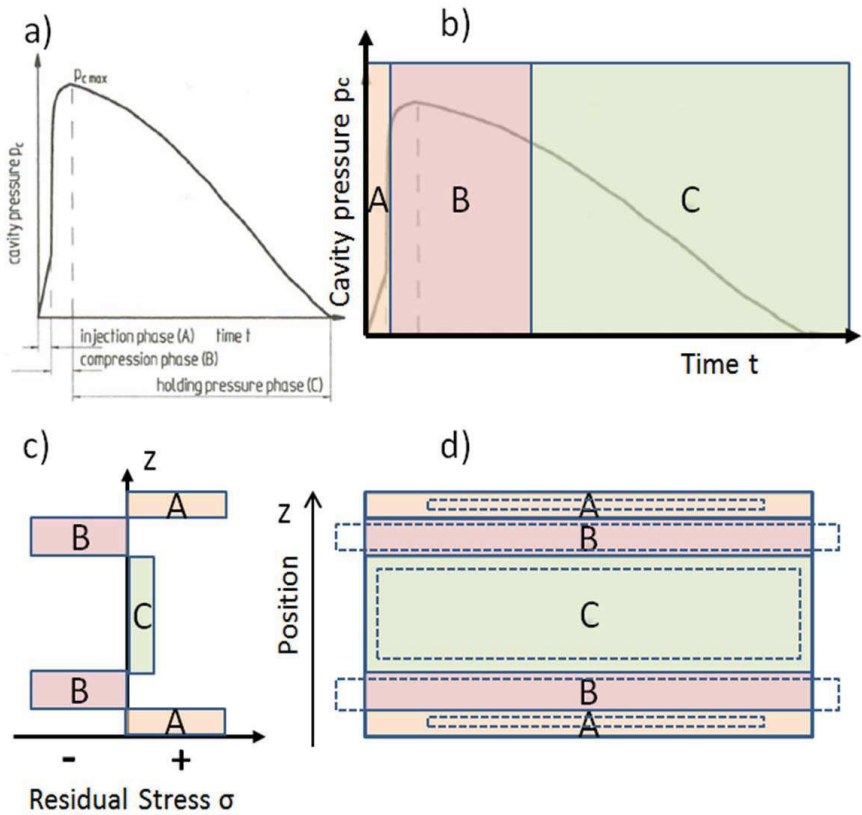


Figure 2.3 Pressure-induced residual stress in a sample during injection moulding. (a) Cavity pressure during injection, [Pötsch 2008]. (b) Three-layer model. Layers solidify at different pressures. (c) Corresponding residual stress in each layer. (d) Free shrinkage (dashed line) and final shrinkage of each layer.

## 2.1.2 Formation of residual stresses in heterogeneous materials

### 2.1.2.1 Cooling of materials with macroscopic heterogeneity

Here, materials composed of different homogeneous layers or plies are focused upon. This is the case for laminates and for some polymer materials, e.g. polypropylene. This inhomogeneity leads to the formation of residual stresses during cooling.

When cooling cross-ply laminates, the thermal contraction of the material is highly anisotropic. Each ply is considered to be a homogeneous continuum. The contraction in a ply is higher in the cross fibre direction than in the fibre direction. In fact, the thermal expansion in the cross fibre direction is mostly due to the contraction of the matrix, which is much higher than the dilation of the fibre, e.g. carbon/epoxy laminates. When observing the cooling of cross ply laminates, the shrinkage of the matrix in the upper ply is restrained by the fibres from the bottom ply (figure 2.4). This leads to tensile residual stresses in the matrix of the upper ply in the cross fibre direction and compressive residual stresses builds up as an equilibrium in the fibre direction in the bottom ply, see Figure 2.4b. The stress state presented in Figure 2.4 is uniform in each ply, which is simplified. Indeed, in Figure 2.4c the high shrinkage of the upper ply stretches the bottom ply and induces warpage. This warpage induces an additional tensile residual stress in the bottom ply near the surface.

In Figure 2.5, a cross-section micrograph of an injected polypropylene can be seen. Note that the surface of the material cooled so fast that no crystalline structure could develop directly at the surface. Thus, the layer on the surface remains purely amorphous and, as a result, has different thermomechanical properties than the semi-crystalline structure in the core. The material also has an in-depth crystallinity gradient. Different optical domains are emphasized in Figure 2.5 with a distance from the surface of 0.03 mm for the amorphous area, 0.08 and 0.2 mm for the high shear strength area, and a sample thickness of about 2.8 mm. In [Housmans 2009], it is evident that the crystallinity ratio has a high gradient near the surface and the crystallinity ratio remains relatively constant in the core of the material. Less crystallinity allows more molecular mobility, and the amorphous layer or the low-crystallinity layers display a higher level of thermal expansion than the core of the material. For this reason, residual stresses form in connection with temperature fluctuations.

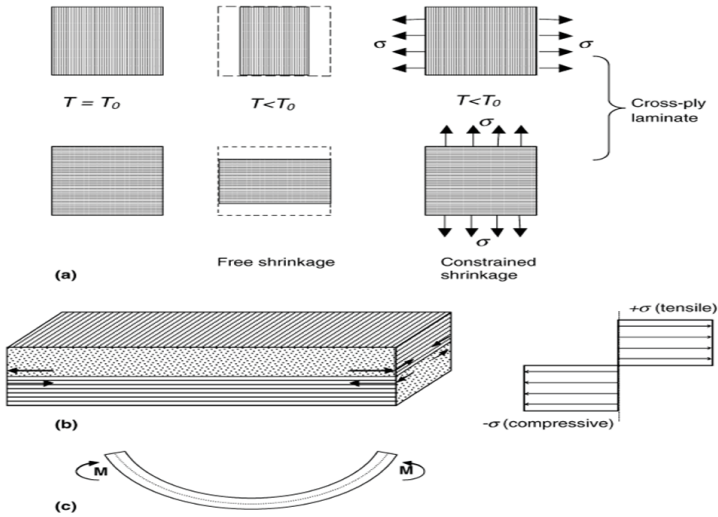


Figure 2.4 Residual stress formation in non-symmetric cross-ply laminate. (a) and (b) thermal residual stress forming when the laminate shrinkage is constrained, (c) front view of out-of-plane deformation when unconstrained. [Parlevliet 2006]

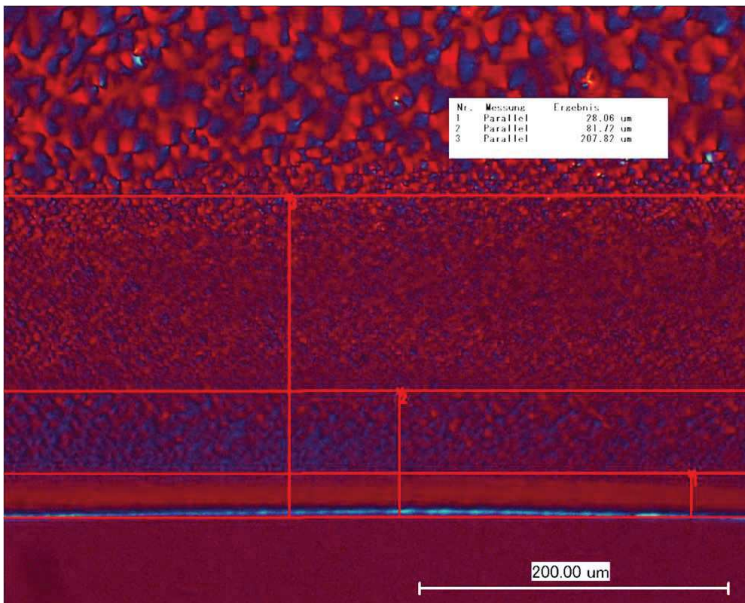
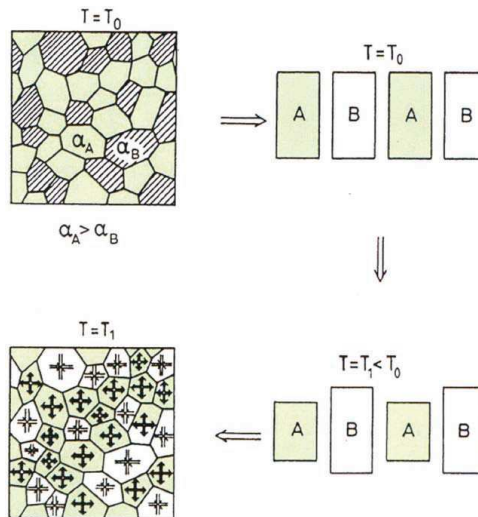


Figure 2.5 Cross section of an injection moulded polypropylene. Microstructure is viewed in polarized light, magnification x100.



### 2.1.2.2 Heterogeneity in microstructure

Residual stresses also exist on a microscopic scale. If a material is composed of two or more different phases, they usually have different thermal expansion coefficients. Therefore, changes in temperature induce a new residual stress state in the different phases of the material (Figure 2.6). Compressive and tensile residual stresses compensate each other. This occurs in matrix-filled material with small fibres, in metal composed of two phases (such as martensitic/austenitic steel), but it can also occur in semi-crystalline structures, as can be seen in Figure 2.5. In the case of this material, partly ordered regions (spherulites) exist in an amorphous matrix, both of them having different thermo-mechanical properties. The amorphous phase has more molecular mobility, its thermal expansion coefficient is higher.



**Figure 2.6** Thermal residual stress induced due to material phases having different thermal expansion coefficients [Scholtes 2017]

### 2.1.3 Conclusion

A concise list of models and mechanisms has been outlined to predict the formation of residual stresses and to interpret results from measurements. Macroscopic residual stresses are a consequence of non-uniform phenomena occurring in a material, e.g. different cooling rates or varying pressures during injection moulding. Residual stresses also develop in a material composed of different phases. Different thermal expansion coefficients lead to self-equilibrated residual stresses between the different phases that compose the material - fibres, crystalline, and amorphous structures - which can be seen as kinds of microscopic residual stresses. In the following chapter, different methods for measuring residual stresses will be presented.

## 2.2 Standard methods for measuring residual stresses

One can benefit from the knowledge of measuring residual stresses in metals and apply it to measuring residual stresses in polymers. In the case of metallic materials, the most commonly used method is X-ray diffraction. However, X-ray diffraction requires a crystalline structure for measuring residual stresses, and, therefore, is not applicable for amorphous structures. In some cases, crystalline phases of materials, e.g. aluminium powder, are added to amorphous polymer materials to enable X-ray diffraction measurements [Behnken and Hawk 1991]. However, no methods suitable for use in practice have been developed. To expand the possibility to perform measurements on amorphous materials, other methods, such as mechanical methods, are available. Among them, the layer removal method has been used in many studies. Some studies also compare results with the hole drilling method [Turnbull 1999, Kim 2007]. Photo-elasticity is also an option to obtain information about molecular orientations and residual stresses. In the following subchapter, these methods will be explained as well as their limitations, and a comparison of their potentials will be carried out.

### 2.2.1 X-ray diffraction

The basic principle of X-ray diffraction is the diffraction of an incident beam (Figure 2.7). Changes in Bragg's angle  $\theta$  correlate with deformations of the crystal lattice spacing based on Bragg's law,

$$n \cdot \lambda = 2D \cdot \sin\theta \quad (2.2)$$

with  $\lambda$  the wavelength of the rays,  $D$  the distance between two lattice planes and  $n$  a whole number to obtain a constructive interference. When working with metallic materials, residual stresses can be measured in a small volume near the surface. The penetration depth depends on the beam wavelength (or energy) and is generally around  $10 \mu\text{m}$  in steel if working with laboratory X-rays and up to  $2 \text{ mm}$  if working with more powerful sources of energy, e.g. synchrotron. In contrast, the penetration depth of the beam is significantly greater in polymer materials and can even pass through the whole sample, because the energy absorption capacity of polymer materials is lower than that of metals. Furthermore, small Bragg's angles are required since the spacing between ordered polymer molecules is larger than between ordered metallic atoms. As a consequence, the measured material volume increases significantly. Consequently, measured residual stresses are either an average of residual stresses along the surface or along the depth.

A secondary effect is that X-ray diffraction only measures residual stresses in the crystalline phase of semi-crystalline materials [Behnken and Hawk 1993]. Therefore, information cannot be obtained about the amorphous phase. However, the residual stress states in both the amorphous and crystalline phases are not necessarily identical. Experiences from working with steel show that if a material presents two phases with

different thermomechanical properties, residual stresses may be different in both phases (Figure 2.6). In [Kornmeier 1999], evidence that different residual stresses were formed in the cementite and ferrite phases of the same samples after plastic deformations of a steel is provided. Similarly, amorphous phases and crystalline phases could present different residual stresses in polymer materials.

In sum, X-ray measurements can be carried out on semi-crystalline polymers, however, the measured volume is larger than when performing standard measurements on metals and is difficult to evaluate. Also, X-ray measurements are not necessarily comparable to mechanical methods, because they only measure residual stresses in the crystalline phase. On the contrary, mechanical methods measure average residual stresses in the amorphous and crystalline phases, which means that only macroscopic residual stresses are captured.

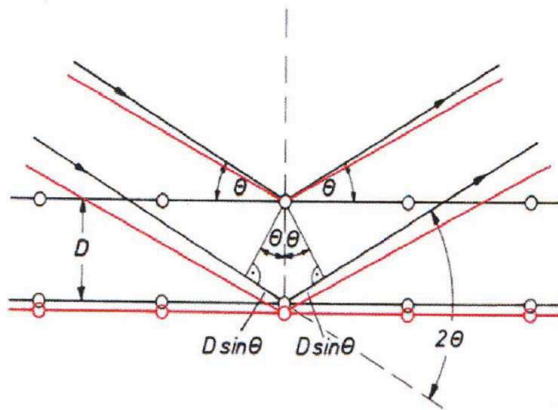


**Figure 2.7** Diffraction occurring during residual stress measurement with X-ray or Neutron diffraction [Gibmeier and Scholtes 2016]

### 2.2.2 Layer removal method

The layer removal method consists of incrementally milling a layer of the whole surface of a material. After removing this layer, the sample forms a new equilibrium and undergoes a deformation. The new curvature of the sample is then measured and correlated with the initial residual stresses in the removed layer. This procedure is then repeated to obtain an in-depth residual stress state. This method presumes that the material will behave linear elastically. However polymer materials are viscoelastic, therefore assumptions are required to take into account time dependent effects occurring during measurements. This time dependency has also been proven in ring slitting tests; in [Allahkarami 2016], the opening of a ring cut from a blow moulded PET bottle grows as time goes on.

The layer removal method is the most commonly used method in literature when working with polymer materials. For example in [Isayev 1984], this method was used to successfully measure thermal residual stresses in the core and the surface of a PMMA material, and, the results were compared to simulation. In [Giroud 2001], the method was also used for injection moulded polypropylene. Results are also applicable for inhomogeneous materials composed of different homogeneous layers and are compared with simulation, however, with questionable success. In several studies, the layer removal method is directly compared to the hole drilling method, and better results were achieved with the layer removal method [Turnbull 1999].

### **2.2.3 Photoelastic stress analysis**

Photoelastic stress analysis can only be applied on birefringent and transparent materials. It is an established method and technical notes exist for measurements [Vishay]. When polarized light passes through the sample, it will split in two wave fronts in the direction of the two principal stresses. The speed of light will then depend on the stresses in each direction. Using Brewster's law to measure the difference in the index of refraction of both waves, it is possible to measure stresses in the material. In [Macias 2015], this method was used to measure flow-induced residual stresses and results were correlated to environmental stress cracking. In [Hornberger 1987], the photoelastic stress analysis was used to reveal induced compressive residual stresses in quenched polycarbonate samples. Compressive residual stresses are correlated with improved life time in flexure.

This method has been discarded for this study for various reasons. First, it does not measure residual stresses, but instead the difference between the two principal stresses. This means that quantitative measurements are only possible in case of a unidirectional residual stress state in the investigated surface, which is generally not the case. Furthermore, if the residual stresses at the surface of the material are in equilibrium with residual stresses deep inside the material, photoelastic stress analysis will misinterpret this stress state as being stress-free.

As such, photoelasticity is a fast method to localize possible regions with high residual stresses. However, a quantitative measurement is restrained to uniaxial stress fields. As a result, this method does not provide useful information for samples used in this work, and will not be utilized.

### **2.2.4 The hole drilling method**

In contrast to the layer removal method, the hole drilling method can measure residual stresses in polymer materials locally. In this method, a hole is drilled incrementally and deformations around the hole are measured as a function of the depth. There are two main formalisms for the hole drilling method: the differential method [Schwarz 1996] and the integral method which is defined in an international standard [ASTM 2013]. Both methods are accurate near the surface as shown by [Nau

2015], who employed both methods on shot-peened steels and compared them to X-ray diffraction. However, the differential method is less accurate for in-depth residual stress measurement above 0.2 mm and especially has difficulties measuring the crossing point where residual stresses change states (transition between compressive and tensile residual stresses). For these reasons, the integral method will be used in this work.

Theory implies that the sample should be an infinite thick plate, however, in practice, the method is adaptable to the real sample geometry. In [Garcia Sobolevski 2007], evidence is provided that a curvature up to three times the size of the hole has almost no effect on the result. In chapter 5.4.1, the fact that the method is even applicable to 1 mm thin metal sheets will be demonstrated, proving it is suitable for very thin polymer components. Yet, as emphasized in [Nau 2011], the method needs to be adapted for polymer materials and modifications are necessary compared to the way it is used on metallic materials. [Kim 2007] states that the viscoelastic behaviour of the material may influence the result and that the hole drilling method is less reliable than the layer removal method. [Casavola 2017 and Nau 2011] illustrate how the rotation rate of the drilling tool needs to be minimized to improve the hole geometry and to limit heating effects that influence the result. In short, the hole drilling method has a huge advantage as it can locally measure residual stresses for a wide variety of materials and for many geometrical configurations. However, the method seems to lack accuracy for applications on polymer materials. In order to benefit from the advantages of the hole drilling method, a detailed analysis of the different influencing factors is necessary (chapter 4). Using the method efficiently, the reliability of the results has been significantly improved (chapter 5).

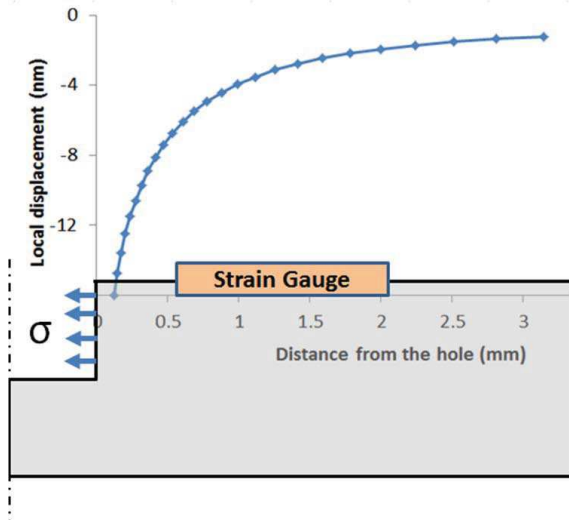
### **2.3 The integral hole drilling method**

This chapter aims to help the reader comprehend the mechanical principle of the hole drilling method. While there is a standard [ASTM 2013] for the hole drilling method containing information about the measuring set-up and calculation algorithms, it requires modification to be applicable to polymer materials. In this chapter, a theoretical background and specificities encountered in this study are explained. Specificities not present in the standard include: non-isotropic material behaviour, inhomogeneous materials, thin geometries and measurements near a notch. It will become clear that the calculation formalism is not the same as for other cases. Algorithms to correlate residual stresses and strains are developed in this chapter. First, the standard case of an isotropic, infinitely thick plate will be focused upon (chapter 2.3.2), which can be extended to isotropic thin components with the same formalism (chapter 3.4.1). This first case corresponds to materials such as isotropic polycarbonate or polypropylene. Then the general case will be shown, which is useful for orthotropic structures such as composite materials and laminate structures (chapter 2.3.3). Lastly, it will be seen that for some components e.g. a transmission welded

polypropylene, it is not recommended to use the formalism from the norm. Due to the presence of a notch (welded joint), it is advised to use the same formalism as for the general case (chapter 2.3.4). Chapter 3 explains how to efficiently obtain calibration coefficients using finite element analysis.

### 2.3.1 Principle

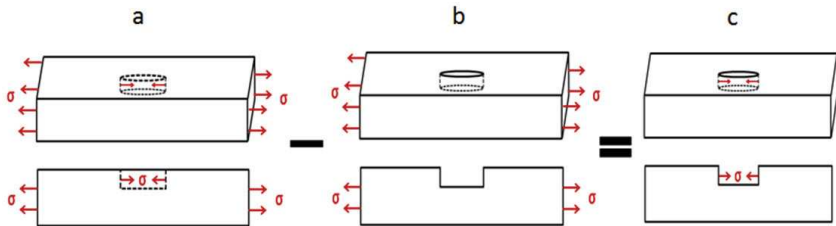
The hole drilling method consists of incrementally drilling a blind hole in a material. Due to the relief of residual stresses in the removed material, a new equilibrium forms locally around the blind hole (Figure 2.8). A strain gauge applied near the hole is used to measure deformations on the surface, and strains are correlated with the initial residual stresses in the material. During a measurement, the measured data is that of the strains. Owing to calibration coefficients calculated using finite element analysis, it is possible to calculate residual stresses from the measured strains (Figure 2.10-11).



**Figure 2.8** Local material displacement after drilling a blind hole in a sample.

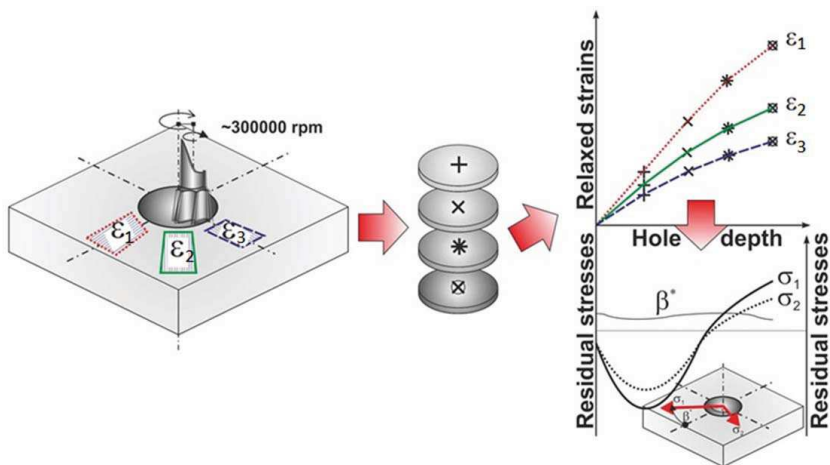
The new equilibrium induced in the sample after drilling a blind hole is emphasized in Figure 2.9. It shows that drilling an increment that relieves strain is equivalent to applying a stress at the hole surface (Figure 2.9c). In fact, the new strain equilibrium is equal to the difference between two cases: the strain field of a tensile test without a hole (Figure 2.9a) and a tensile test with a blind hole (Figure 2.9b). In Figure 2.9a, the stress inside the sample refers to the principle of reciprocity of the applied force, the small volume works like a spring which resists the deformation. Furthermore stresses and strains can be directly correlated with Hooke's law, like in a tensile test. The strain distribution of a stretched drilled plate is known as Kirsch's law [Kirsch 1898]. In

Figure 2.9b, the model is similar to Kirsch's problem, because a blind hole is comparable to a hole that passes through the material entirely. Therefore, the hole drilling method (Figure 2.9c) is a combination of Hooke's law and an adaptation of Kirsch's law.



**Figure 2.9** Model equivalence for stress distribution after drilling an increment in case of the hole drilling method

Figure 2.8 shows the resulting axial displacement of a component made of steel after drilling a blind hole 2 mm in diameter with a penetration depth of about 20  $\mu\text{m}$  and an initial residual stress  $\sigma = 100$  MPa. Note that the measured strain is quite small, about 2  $\mu\text{m}/\text{m}$ . In regards to the size of a strain gauge (1.5 mm), this corresponds to a local expansion of about 3 nm. If a hole that passes through the material is drilled, then it is only possible to measure an average stress. In order to know how the residual stresses vary in the depth, it is necessary to drill incrementally and to measure strains after each drilled increment (Figure 2.10).



**Figure 2.10** Measured strain relaxation after each drilling step [Nau 2015]. Strains are measured in three directions.

When using the hole drilling method, the material is assumed to be homogeneous and to behave like linear elastic material. In theory, the material is an infinitely thick plate, however, in practice, the method can be adapted to almost all geometries. In fact, in [Garcia Sobolevski 2007, Nau 2015] influencing of the geometric parameters, such as material curvature, was investigated with finite element analysis. Residual stresses are supposed to be uniform and biaxial in each drilled material volume, however, they are not necessarily uniform in terms of their depth. Holes in metals are usually drilled at a very high speed of about 300,000 rpm using the orbiting method in order not to induce residual stresses in the material [Flaman 1982]. This rotation speed needs to be reduced to a few rotations per minute when working with polymer materials to avoid heating [Nau 2011]. The experimental set-up is illustrated in chapter 4 and differs from the common application on metals because of the low stiffness of the polymer materials, their low thermal conductivity, their high thermal expansion coefficient and their viscoelastic behaviour.

In Figure 2.11, a schematic relation between the residual stresses and strains is shown for the integral hole drilling method. An increment is drilled, and, then, because of the residual stress  $\sigma_1$  initially present in the first increment, a deformation  $\varepsilon_1$  can be measured. Similarly, a total deformation  $\varepsilon_N$  is measured after drilling the  $N_{th}$  increment. In Figure 2.11,  $\varepsilon_{ij}$  refers to the strain measured after drilling the  $i_{th}$  increment due to the removed residual stresses in the  $j_{th}$  increment. Also, it is evident the initial residual stress in a removed increment, such as  $\sigma_1$ , contributes to deformations differently after drilling each following increment. This means that as the material is drilled, the local stiffness is reduced around the blind hole. As a consequence, the deformation induced by  $\sigma_1$  will increase after each following increment:  $\varepsilon_{i+1,1} > \varepsilon_{i,1} > \varepsilon_{1,1}$ . Constants  $k_{ij}$  can then be defined to correlate the residual stresses in the  $j_{th}$  increment with the measured strain after drilling the  $i_{th}$  increment.

$$\{\varepsilon\} = [k_{ij}] \cdot \{\sigma\} ; \quad \varepsilon_i = \sum k_{ij} \cdot \sigma_j \quad (2.3)$$

Please note that this equation is not generally applicable, because it is simplified. A more complex form of this equation will be provided at a later point in time to take the direction of the measured strains and the biaxial form of residual stresses into account (equation 2.6-2.7).



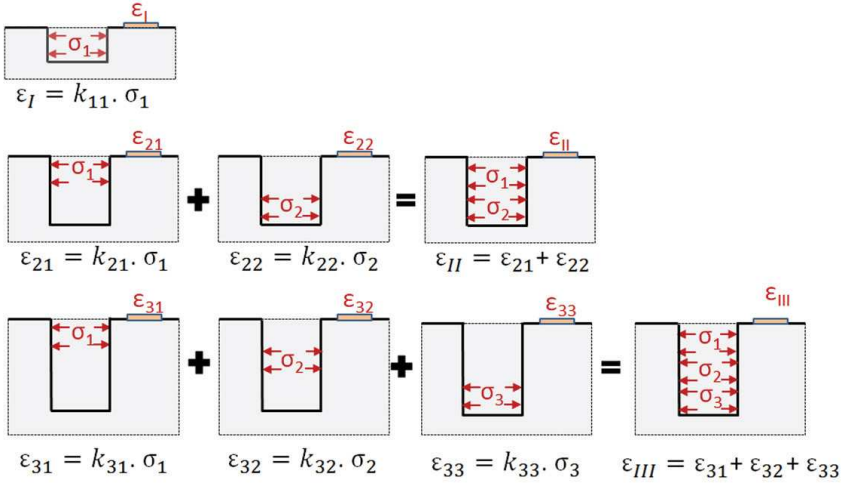


**Figure 2.11** Simplified model for the integral formalism of the hole drilling method. Total strain  $\epsilon_i$  is the sum of strain  $\epsilon_{ij}$  induced by each stress  $\sigma_j$  applied after drilling the  $i^{\text{th}}$  increment. Coefficients  $k_{ij}$  correlate stress  $\sigma_j$  and strain  $\epsilon_{ij}$  (simplified for example purpose).

### 2.3.2 Isotropic material

In the case of an isotropic material, displacements and strains around the hole can be measured to calculate residual stresses. Displacement data is especially useful if an optical method, such as the digital image correlation or the electronic speckle pattern Interferometry, is used in combination with the hole drilling method instead of strain gauges [Baldi 2005-2014, Nobre 2014]. Electronic speckle pattern interferometry even provided satisfying results when used on a polycarbonate sample [Rickert 2016]. Furthermore, displacement data simplifies finite element analysis to obtain strain data ([Schajer 1993], chapter 3.1). In fact, displacements converge faster than strains in finite element analysis. The strain measured by a strain gauge can be obtained from the direct differences between displacement data obtained at the extremity of each grid of the strain gauge (equation 3.8). Calculating a difference is more convenient than integrating strains over the area of the strain gauge. For this reason, the correlations between the displacements and the residual stresses are presented, even if only strain data are measured in this work.

After removing an increment, the material around the hole reaches a new equilibrium and the displacements  $u_r$  in the radial direction and  $u_\theta$  in the circumferential direction (Figure 2.12) take the following form [Makino 94]:

$$u_r = A_u (\sigma_x + \sigma_y) + B_u [(\sigma_x - \sigma_y) \cos(2\theta) + 2\tau_{xy} \sin(2\theta)] \quad (2.4)$$

$$u_\theta = C_u [(\sigma_x - \sigma_y) \sin(2\theta) - 2\tau_{xy} \cos(2\theta)] \quad (2.5)$$

When using optical methods, such as digital image correlation, the full field displacement can be used to directly calculate residual stresses [Baldi 2005]. Note that  $A_u$ ,  $B_u$  and  $C_u$  are functions of the measurement position (radius), and do not depend on the angle  $\theta$ . When using strain gauges, a theoretical solution exists for a plate that has been drilled through by taking the decomposition presented in Figure 2.9 (combination of Hooke's law and Kirsch's law) into account.

$$\varepsilon(\theta) = \frac{1+\nu}{E} a \frac{\sigma_x + \sigma_y}{2} + \frac{1}{E} b \frac{\sigma_x - \sigma_y}{2} \cos(2\theta) + \frac{1}{E} b \cdot \tau_{xy} \cdot \sin(2\theta) \quad (2.6)$$

$a$  and  $b$  are constants which depend mostly on the geometry of the strain gauge, the hole dimension and the geometry of the sample. In order to obtain a non-uniform, in-depth residual stress profile, this equation is written in an index form, as explained in the previous chapter (figure 2.11). Equation 2.7 shows an example for four drilled increments with  $\varepsilon_i(\theta)$  the strain measured after drilling the  $i^{\text{th}}$  increment and  $(\sigma_x)_i$ ,  $(\sigma_y)_i$ ,  $(\tau_{xy})_i$  the residual stresses in the  $i^{\text{th}}$  drilled increment.

$$\begin{pmatrix} \varepsilon_1 \\ \varepsilon_2 \\ \varepsilon_3 \\ \varepsilon_4 \end{pmatrix}(\theta) = \frac{1+\nu}{2E} \cdot \begin{bmatrix} a_{11} & 0 & 0 & 0 \\ a_{21} & a_{22} & 0 & 0 \\ a_{31} & a_{32} & a_{33} & 0 \\ a_{41} & a_{42} & a_{43} & a_{44} \end{bmatrix} \cdot \begin{pmatrix} (\sigma_x + \sigma_y)_1 \\ (\sigma_x + \sigma_y)_2 \\ (\sigma_x + \sigma_y)_3 \\ (\sigma_x + \sigma_y)_4 \end{pmatrix} + \frac{1}{2E} \cdot \begin{bmatrix} b_{11} & 0 & 0 & 0 \\ b_{21} & b_{22} & 0 & 0 \\ b_{31} & b_{32} & b_{33} & 0 \\ b_{41} & b_{42} & b_{43} & b_{44} \end{bmatrix} \cdot \left( \begin{pmatrix} (\sigma_x - \sigma_y)_1 \\ (\sigma_x - \sigma_y)_2 \\ (\sigma_x - \sigma_y)_3 \\ (\sigma_x - \sigma_y)_4 \end{pmatrix} \cdot \cos(2\theta) + 2 \cdot \begin{pmatrix} \tau_{xy1} \\ \tau_{xy2} \\ \tau_{xy3} \\ \tau_{xy4} \end{pmatrix} \cdot \sin(2\theta) \right) \quad (2.7)$$

These calibration coefficients also depend on the material geometry, the used strain gauge geometry and the material elastic constants. In fact, [Nau 2013] noted that these calibration coefficients also are a function of Poisson's ratio  $\nu$  (see also chapter 3.4.2). The standard [ASTM 2013] provides coefficients to be used for a thick plate with isotropic material behaviour and  $\nu=0.3$ . In this study, polymer materials were investigated. Their elastic property (Poisson's ratio  $\nu \approx 0.4$ ) and geometry (thin component) strongly differ from the one used in the standard, hence, calibration coefficients are specific to each investigated case. Equation (2.7) can also be extended to materials composed of different layers assuming that each layer consists of an isotropic material (see chapter 3.3.1).

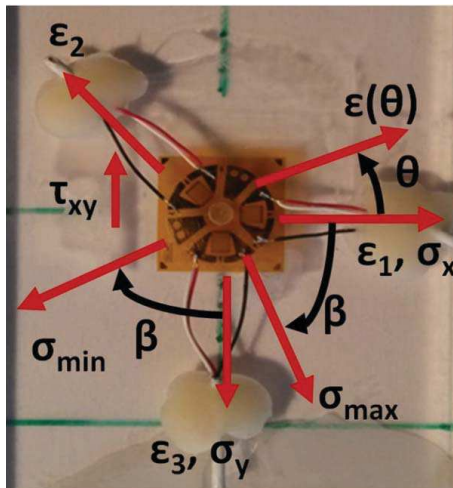


**Figure 2.12** Strain gauge (Vishay Micro-Measurements, Type EA-062RE) glued on a polycarbonate sample and corresponding system of coordinates used in this work.

When solving equation 2.7, the three unknown stress components  $\sigma_x$ ,  $\sigma_y$  and  $\tau_{xy}$  need to be determined (a planar stress condition is assumed). Therefore, three strains are required to solve this system, and these strains are measured in three different directions. Regarding the notation in Figure 2.12 and equation 2.6 - 2.7, relations between strains and stresses can be deduced using  $\varepsilon_{1_i} = \varepsilon_i(\theta = 0^\circ)$ ;  $\varepsilon_{2_i} = \varepsilon_i(\theta = 135^\circ)$ ;  $\varepsilon_{3_i} = \varepsilon_i(\theta = -90^\circ)$ ,  $\varepsilon_i(\theta)$  being the strain measured after drilling the  $i_{th}$  increment at the position  $\theta$ . Measuring strains at these positions simplifies the solution of equation system 2.7, as can be seen in equations 2.9 and 2.11 where the sum and difference of  $\varepsilon_{1_i}$  and  $\varepsilon_{3_i}$  isolate the matrices  $\bar{a}$  and  $\bar{b}$ . The residual stresses can then easily be obtained by calculating the inverse of the matrices  $\bar{a}$  and  $\bar{b}$  separately.

- By summing up  $\varepsilon_{1_i}$  and  $\varepsilon_{3_i}$  the following relations are obtained:

$$\bar{a} \cdot \{P\} = \bar{a} \cdot \left\{ \frac{\sigma_x + \sigma_y}{2} \right\} = \frac{E}{1+\nu} \cdot \{p\} = \frac{E}{1+\nu} \cdot \left\{ \frac{\varepsilon_1 + \varepsilon_3}{2} \right\} \quad (2.8)$$

$\bar{a}$  is a lower triangular matrix, P a stress vector, and p a strain vector. Equation 2.9 shows an example for three increments:

$$\frac{1}{2} \cdot \begin{bmatrix} a_{11} & 0 & 0 \\ a_{21} & a_{22} & 0 \\ a_{31} & a_{31} & a_{33} \end{bmatrix} \cdot \left\{ \begin{array}{l} (\sigma_x + \sigma_y)_1 \\ (\sigma_x + \sigma_y)_2 \\ (\sigma_x + \sigma_y)_3 \end{array} \right\} = \frac{E}{2(1+\nu)} \cdot \left\{ \begin{array}{l} (\varepsilon_1 + \varepsilon_3)_1 \\ (\varepsilon_1 + \varepsilon_3)_2 \\ (\varepsilon_1 + \varepsilon_3)_3 \end{array} \right\} \quad (2.9)$$

- Then the difference between  $\varepsilon_{3_i}$  and  $\varepsilon_{1_i}$  produces the following result:

$$\bar{b} \cdot \{Q\} = \bar{b} \cdot \left\{ \frac{\sigma_y - \sigma_x}{2} \right\} = E \cdot \{q\} = E \cdot \left\{ \frac{\varepsilon_3 - \varepsilon_1}{2} \right\} \quad (2.10)$$

$\bar{b}$  is a lower triangular matrix, Q a stress vector, and q a strain vector.

- Equations 2.8 and 2.10 provide enough information about the stress components  $\sigma_x$  and  $\sigma_y$ . To calculate the shear stress, the strain gauge  $\varepsilon_{2_i}$  is necessary and

$$\bar{b} \cdot \{T\} = \bar{b} \cdot \{\tau_{xy}\} = E \cdot \{t\} = E \cdot \left\{ \frac{\varepsilon_3 + \varepsilon_1 - 2 \cdot \varepsilon_2}{2} \right\} \quad (2.11)$$

with T a stress vector and t a strain vector.

In equations (2.8-2.11), the residual stresses  $\sigma$  and  $\tau$  are the unknown variables, strains  $\varepsilon$  are measured with strain gauges and the triangular matrices  $\bar{a}$  and  $\bar{b}$  need to be calculated with finite element analysis. The residual stresses can be calculated by inverting the matrices  $\bar{a}$  and  $\bar{b}$ . It is possible to calculate the two principal stresses  $\sigma_{max}$  and  $\sigma_{min}$  from the residual stresses  $\sigma_x$ ,  $\sigma_y$  and  $\tau_{xy}$  and their respective position with the angle  $\beta$  between  $\sigma_x$  and  $\sigma_{max}$ .

$$\sigma_{max} = P + \sqrt{Q^2 + T^2} \quad (2.12)$$

$$\sigma_{min} = P - \sqrt{Q^2 + T^2} \quad (2.13)$$

$$\beta = \frac{1}{2} \cdot \arctan\left(\frac{-T}{-Q}\right) \quad (2.14)$$

### 2.3.3 Anisotropic or orthotropic material

When working with anisotropic or orthotropic materials, equations 2.4-2.11 are no longer valid. Displacement distributions take a new form, which is much more complicated [Baldi 2007]. If strain gauges are being used, the following general formula can be used and the coefficient values can be found in [Schajer 1994, Pagliaro 2007] in the case of a uniform residual stress measurement with a hole that has been drilled through an orthotropic material.

$$\begin{pmatrix} \varepsilon_1 \\ \varepsilon_3 \\ \varepsilon_2 \end{pmatrix} = \begin{bmatrix} C_{11} & C_{12} & C_{13} \\ C_{21} & C_{22} & C_{23} \\ C_{31} & C_{32} & C_{33} \end{bmatrix} \cdot \begin{pmatrix} \sigma_x \\ \sigma_y \\ \tau_{xy} \end{pmatrix} \quad (2.15)$$

The calibration coefficients  $C_{ij}$  are a function of the elastic material properties, the material geometry, the strain gauge geometry and the orientation between the strain gauge and the principal elastic direction of the sample. All elastic material constants are required for the finite element analysis, and, in the case of orthotropic structures, elastic constants reduce to:  $E_{11}$ ,  $E_{22}$ ,  $E_{33}$ ,  $G_{12}$ ,  $G_{13}$ ,  $G_{23}$ ,  $\nu_{12}$ ,  $\nu_{13}$ ,  $\nu_{23}$ . They apply for laminate and composite materials, e.g. the reinforced polypropylene composite PURE investigated in this study. Aligning the strain gauge with the principal elastic direction

is recommended for reasons of simplicity. [Sánchez-Beitia 2015] shows how these coefficients are experimentally measured for a uniform, in-depth residual stress measurement in wood materials. This approach is also applicable for the isotropic case and using equations (2.6) and (2.15), the following relation is obtained:

$$\begin{pmatrix} \varepsilon_1 \\ \varepsilon_3 \\ \varepsilon_2 \end{pmatrix} = \frac{1}{2 \cdot E} \begin{bmatrix} (1 + \nu) \cdot a + b & (1 + \nu) \cdot a - b & 0 \\ (1 + \nu) \cdot a - b & (1 + \nu) \cdot a + b & 0 \\ (1 + \nu) \cdot a & (1 + \nu) \cdot a & -2 \cdot b \end{bmatrix} \cdot \begin{pmatrix} \sigma_x \\ \sigma_y \\ \tau_{xy} \end{pmatrix} \quad (2.16)$$

As can be seen in the isotropic case (equation 2.16), only two constants are required instead of nine constants. They can be obtained by using only one simulation with  $\sigma_x = 1$ ,  $\sigma_y = 0$ ,  $\tau_{xy} = 0$  (see chapter 3.1.1). In the orthotropic case, the coefficients  $C_{ij}$  are independent and three load cases are necessary.

To measure a non-uniform, in-depth residual stress profile, equation (2.15) is rewritten in indexed form. Index  $i$  represents the number of drilled increments and  $j$  the  $j_{th}$  increment where the load is applied (Figure 2.11). A similar method was already proposed in [Akbari 2014].

$$\begin{pmatrix} \varepsilon_1 \\ \varepsilon_3 \\ \varepsilon_2 \end{pmatrix}_i = \sum \begin{bmatrix} C_{11} & C_{12} & C_{13} \\ C_{21} & C_{22} & C_{23} \\ C_{31} & C_{32} & C_{33} \end{bmatrix}_{ij} \cdot \begin{pmatrix} \sigma_x \\ \sigma_y \\ \tau_{xy} \end{pmatrix}_j \quad 1 \leq j \leq i \quad (2.17)$$

It is possible to solve this system with the following iteration:

$$\begin{pmatrix} \sigma_x \\ \sigma_y \\ \tau_{xy} \end{pmatrix}_i = \begin{bmatrix} C_{11} & C_{12} & C_{13} \\ C_{21} & C_{22} & C_{23} \\ C_{31} & C_{32} & C_{33} \end{bmatrix}_{ii}^{-1} \cdot \left( \begin{pmatrix} \varepsilon_1 \\ \varepsilon_3 \\ \varepsilon_2 \end{pmatrix}_i - \sum_{j=1}^{i-1} \begin{bmatrix} C_{11} & C_{12} & C_{13} \\ C_{21} & C_{22} & C_{23} \\ C_{31} & C_{32} & C_{33} \end{bmatrix}_{ij} \cdot \begin{pmatrix} \sigma_x \\ \sigma_y \\ \tau_{xy} \end{pmatrix}_j \right) \quad (2.18)$$

An example for the self-reinforced polypropylene composite PURE can be viewed in attachment B. Coefficients are shown up to a thickness of 0.2 mm, but were calculated up to 0.8 mm for the sake of conciseness. These coefficients were calculated using finite element analysis as described in chapter 3.2.

### 2.3.4 Influence of the geometry, case of a sample with a welded joint

In some cases, residual stresses in isotropic materials can be obtained using the formalism presented in chapter 2.3.3 for orthotropic materials. This holds true when measurements are performed near a notch or an edge if the deformation field is affected. In the standard case for isotropic materials presented in chapter 2.3.2, the material was assimilated to an infinitely thick plate. However, if a measurement is performed near an edge or a notch of a component, then the strain distribution around the hole is influenced by the notch. Thus, the relation between the stress and measured strain is no more the same as in the case of an infinite isotropic plate. The new sample

calibration coefficients  $C_{ij}$  that correlate stress and strain (equations 2.15 and 2.17) need to be determined with a finite element model that is as close to reality as is possible. In [Nau 2015], the influence of an edge is demonstrated with finite element analysis for the case of residual stresses being calculated with the isotropic formalism (chapter 2.3.2). The residual stresses parallel to an edge are still accurate, whereas residual stresses oriented perpendicular to the edge are inaccurate. The measurement was simulated 3 mm and 5 mm from the edge with a hole diameter of 2 mm.

In this study, another example is given for two thin (2 mm) polymer samples welded together using a laser transmission welding process (Figure 2.13). If a 4 mm diameter hole is drilled to obtain information near the welded joint, the thickness of the sample becomes critical, and strongly influences the calibration matrices correlating with the stress and strain (see chapter 5.1.2). Moreover, the welding joint causes a notch effect, and, as a consequence, the relation between stress and strain is different from the isotropic case. In fact, stretching the sample with a stress  $\sigma_x$  causes deformation  $\epsilon_1$  (Figure 2.13). However, if the sample is stretched by  $\sigma_y$ , the measured deformation  $\epsilon_3$  is then different compared to the previous  $\epsilon_1$  due to the notch effect. This means that the coefficients  $C_{11}$  and  $C_{22}$  in equation 2.15 are not equal anymore. Moreover, regarding the coefficients  $C_{11}$  and  $C_{22}$  in equation 2.16, it is evident that the calibration matrices  $\bar{a}$  and  $\bar{b}$  used for the isotropic case cannot be used here, because  $C_{11}$  and  $C_{22}$  should be different. Therefore, a geometry specific calibration matrix  $C$  needs to be simulated (see chapter 3.2) and the calculation of residual stresses should not use the formalism for isotropic infinite plates. Although incorrect, the use of the isotropic model is still possible, and leads to errors – the magnitudes of which are presented in chapter 5.1.2.

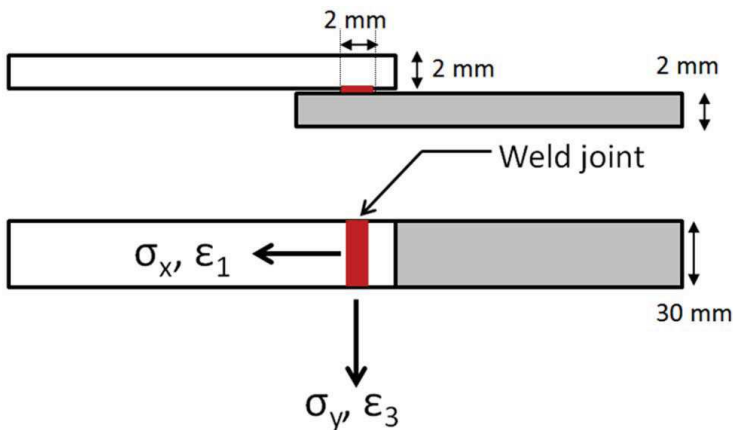


**Figure 2.13** Dimension of sample welded with transmission laser welding

## 2.4 Conclusion

During manufacturing of polymers, residual stresses are induced in the material due to inhomogeneous processes, e.g., cooling and pressure history. There are different methods to measure residual stresses. Among them, the hole drilling method has high potential, because it can be used in broad range of material classes (metal, amorphous material, semi-crystalline materials). The standard method for in-depth, non-uniform residual stress analysis as defined in [ASTM 2013] is only applicable under the following conditions: the material is linear-elastic isotropic, the strain gauge is applied to a flat surface far enough from the edge, and the sample is thick enough. Still, the formalisms can be applied to almost all geometries and also to materials composed of different isotropic layers or orthotropic materials. For this reason, calibration coefficients are required which are calculated with finite element model. Chapter 3 details the finite element analysis needed to obtain the necessary calibration coefficients that correlate with strains and residual stresses.

### 3 Determination of calibration matrices

In chapter 2.3, relations between stress and strain were introduced; to calculate residual stresses, calibration matrices are required. This chapter describes how to obtain these coefficients with finite element analysis. In literature, the isotropic case is dealt with using a 2D or a 3D finite element model. A 2D model requires special elements, like the element CAXA in Abaqus (version 6.13), and then it should be possible to create a 2D axisymmetric model with a non-axisymmetric stress distribution around a hole. However, as will be illustrated in chapter 3.1.1, the stress applied at the hole boundary is a combination of non-axisymmetric pressure and shear stress. In Abaqus, the CAXA element is only compatible with non-axisymmetric pressure, but not with non-axisymmetric shear stress. For this reason, if one wishes to calculate the calibration matrices  $\bar{a}$  and  $\bar{b}$  (equations 2.6-2.11), using a 3D model is compulsory when employing software Abaqus. Furthermore, in order to reduce the simulation time, symmetries are used and a fourth model is required, however, this is not generally the case with orthotropic materials where the whole model was built.

This study proposes using the same model for all the different strain gauge geometries and for all possible hole eccentricity cases for the isotropic case (chapter 3.1). The material orthotropy and material heterogeneity (different homogeneous layers) are a direct extension of the isotropic model (chapter 3.2 and 3.3). Which parameters are of great importance for the calculation of the matrices  $\bar{a}$  and  $\bar{b}$  in the case of an isotropic infinite plate (3.4) are shown. Advice on how to avoid unnecessary simulations is provided.

Please refer to the following chapters for the different materials investigated in this study. Polycarbonate samples are considered to be isotropic (see chapter 3.1). The reinforced polypropylene PURE is an orthotropic laminate structure (see chapter 3.2). The polypropylene components are modelled as a heterogeneous material composed of many homogeneous isotropic layers (see chapter 3.3.2).

#### 3.1 Calculation of coefficients for the isotropic case

A representation of the finite element model used in this work is shown in figure 3.1. This model is composed of about 170,000 elements of the type CCL12. The blind hole is drilled in 25 increments: 10 steps of about 0.02 mm thickness and from then onward 15 increments of about 0.04 mm. The simulation runs over the course of approximately three days to calculate the matrices  $\bar{a}$  and  $\bar{b}$  in their entirety, which equals 325 coefficients for each matrix. A computer with dual processor Intel Xeon x5660 was used with each of the six cores running at 2.8 GHz and 24 GB RAM for each processor. The calculation time is reasonable as the necessity to simulate new coefficients does not happen often. Furthermore, results from the same simulation can be used regardless of the geometry of the strain gauges and wherever the hole is drilled (eccentricity). In fact, it is not necessary to redo a simulation for each case, because all



the information is available in one model. For this purpose, it is best to make use of the displacement data, and to calculate the strains at the strain gauge positions from these displacements [Schajer 1993]. The same method of calculation can be applied to the hole drilling method using optical methods, which also measure displacement data [Baldi 2014]. Due to the fact that the material is considered to be isotropic, only two elastic constants are used in the model, e.g.  $E=2400$  MPa and  $\nu=0.4$  for polycarbonate components. Matrices  $\bar{a}$  and  $\bar{b}$  depend on Poisson's ratio (chapter 3.4.2), but not on the Young's modulus of the material.

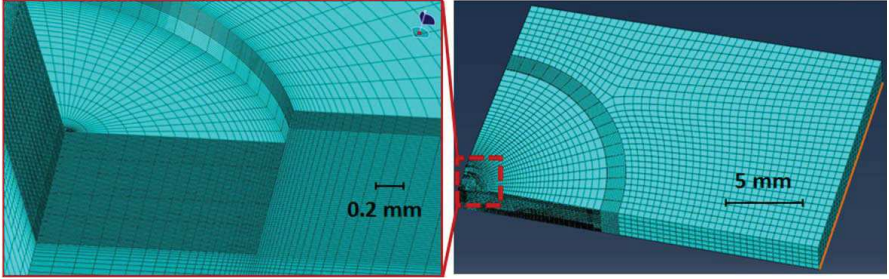


**Figure 3.1** Finite element model used for the isotropic case. A 0.2 mm blind hole is removed from a 1 mm thick sample. The thickness of the sample can be varied.

### 3.1.1 Determining the displacement and strain field for any load case

In order to obtain the calibration matrices  $\bar{a}$  and  $\bar{b}$ , two load cases are usually simulated: an equibiaxial stress state for  $\bar{a}$  with  $\sigma_x = \sigma_y = 1$ ,  $\tau_{xy} = 0$  and a pure shear stress state for  $\bar{b}$  with  $\sigma_x = -\sigma_y = 1$ ,  $\tau_{xy} = 0$ . It is also possible to perform only one simulation with  $\sigma_x = 1$  and to deduce the other load cases from it, as explained below. This reduces the calculation time to obtain calibration coefficients. Owing to the fact that the stress needs to be applied on the hole surface, it is beneficial to use polar decomposition of the stress vector. The following transformation can be used with  $\theta$ , which is the angle between  $\sigma_x$  and  $\sigma_r$ .

$$\begin{pmatrix} \sigma_r \\ \sigma_\theta \\ \tau_{r\theta} \end{pmatrix} = \begin{bmatrix} \cos^2 \theta & \sin^2 \theta & 2 \cdot \cos \theta \cdot \sin \theta \\ \sin^2 \theta & \cos^2 \theta & -2 \cdot \cos \theta \cdot \sin \theta \\ -\cos \theta \cdot \sin \theta & \cos \theta \cdot \sin \theta & \cos^2 \theta - \sin^2 \theta \end{bmatrix} \cdot \begin{pmatrix} \sigma_x \\ \sigma_y \\ \tau_{xy} \end{pmatrix} \quad (3.1)$$

Then  $\sigma_r$  and  $\tau_{r\theta}$  are applied at the hole boundary, but not  $\sigma_\theta$  as it is not a boundary condition. In fact, Figure 3.2 (right) shows that only  $\sigma_r$  and  $\tau_{r\theta}$  are applied at the surface of the hole.

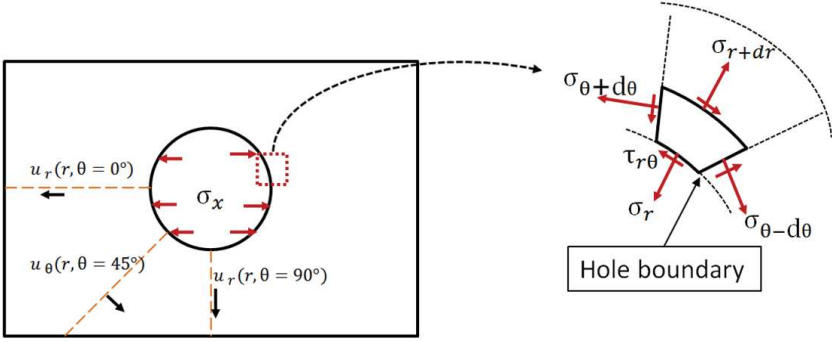


**Figure 3.2** Stress applied at the hole surface, and displacements measured around the hole

One simulation with  $\sigma_x = 1$ ,  $\sigma_y = 0$ ,  $\tau_{xy} = 0$  is enough to calculate other load cases. Since the material is isotropic, the load case  $\sigma_x = 1$  is the same as applying  $\sigma_y = 1$  while considering a rotation of the sample of  $90^\circ$ . This means the following for the displacement values  $u_r$  and  $u_\theta$ .

$$u_r(\theta, \sigma_x = 1) = u_r\left(\theta \pm \frac{\pi}{2}, \sigma_y = 1\right) \quad (3.2)$$

Thus, a simulation with a load  $\sigma_y$  is unnecessary, because it can be obtained from  $\sigma_x$ . Similarly, the pure shear stress case is the same as having a combination of  $\sigma_x = -1$ ,  $\sigma_y = 1$  and a rotation of the model of  $\theta = 45^\circ$  as can be seen in Figure 3.3. In Figure 3.3, the red line represents where the displacement is considered to be, and it shows the equal displacement between each step. It is as follows when written as an equation.

$$u_r(\theta, \tau_{xy} = 1) = u_r\left(\theta + \frac{\pi}{4}, \sigma_y = 1\right) + u_r\left(\theta + \frac{\pi}{4}, \sigma_x = -1\right) \quad (3.3)$$

And with equation (3.2), following formula is obtained:

$$u_r(\theta, \tau_{xy} = 1) = u_r\left(\theta + \frac{3\pi}{4}, \sigma_x = 1\right) - u_r\left(\theta + \frac{\pi}{4}, \sigma_x = 1\right) \quad (3.4)$$

These representations demonstrate that the displacement obtained from any load case  $(\sigma_x, \sigma_y, \tau_{xy})$  is a decomposition of a uniaxial load case  $\sigma_x$ . In order to obtain information about the entire displacement field from any load case, it is convenient to use equations 2.4 and 2.5. Equation 2.4 and 2.5 can be used to calculate the functions  $A_u(r)$ ,  $B_u(r)$  and  $C_u(r)$  from the displacements along the three orange dotted lines shown in Figure 3.2.

$$2 \cdot A_u(r) \cdot \sigma_x = u_r(r, \theta = 0) + u_r(r, \theta = 90) \quad (3.5)$$

$$2 \cdot B_u(r) \cdot \sigma_x = u_r(r, \theta = 0) - u_r(r, \theta = 90) \quad (3.6)$$

$$C_u(r) \cdot \sigma_x = u_\theta(r, \theta = 45) \quad (3.7)$$

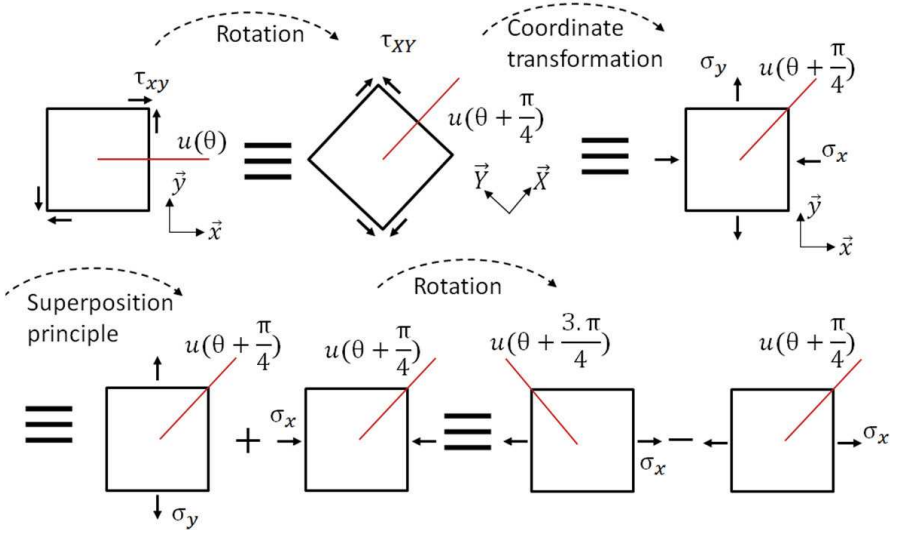


**Figure 3.3 Displacement equivalence from a pure shear stress to a uniaxial stress state (isotropic case). Red line represents where the displacements are equal**

With the aid of the functions  $A_u(r)$ ,  $B_u(r)$  and  $C_u(r)$ , displacements can be calculated at any location. To calculate the strain at a strain gauge position, it is sufficient to interpolate the displacement data at the active grid extremities of the strain gauge (see Figure 3.4 and the red points). The strain is then provided by [Schajer 1993],

$$\epsilon_X = \frac{\sum_i (U_{X2i} - U_{X1i}) / W_i}{\sum_i (X_{2i} - X_{1i}) / W_i} \quad (3.8)$$

with  $[X_1, X_2]$  as the position of the active grids of the strain gauge,  $i$  as the  $i_{th}$  grid line of the strain gauge, and  $W_i$  the width of the  $i_{th}$  grid line. The influence of the strain perpendicular to the strain gauge axis (transverse sensitivity) is generally neglected, but an exception was found for composite materials [Ajovalasit 2011].



**Figure 3.4** Strain gauge type EA-062RE and active parts of a strain gauge grid.

### 3.1.2 Calculation of the matrix $\bar{a}$

The matrix  $\bar{a}$  corresponds to an equibiaxial stress state. Having  $\sigma_x = \sigma_y = 1$ , equations 2.4-2.5 and 2.8 simplify to:

$$\bar{a} \cdot \left\{ \frac{\sigma_x + \sigma_y}{2} \right\} = \bar{a} \cdot \{\sigma_x\} = \bar{a} = \frac{E}{1+\nu} \cdot \left\{ \frac{\varepsilon_1 + \varepsilon_3}{2} \right\} = \frac{E}{1+\nu} \cdot \varepsilon_1 \quad (3.9)$$

$$2 \cdot A_u(r) = u_r(r, \theta) ; \quad u_\theta(r, \theta) = 0 \quad (3.10)$$

Note, in this case  $\varepsilon_1$  equals  $\varepsilon_3$  as they are both located at the same distance from the hole (Figure 3.4). If the hole is eccentric,  $\varepsilon_1$  and  $\varepsilon_3$  need to be calculated separately using equations 3.8 and 3.10.

### 3.1.3 Calculation of the matrix $\bar{b}$

Matrix  $\bar{b}$  corresponds to a pure shear stress state. Having  $\sigma_x = -\sigma_y = 1$ , equations 2.4-2.5 and 2.10 simplify and:

$$\bar{b} \cdot \{Q\} = \bar{b} \cdot \left\{ \frac{\sigma_y - \sigma_x}{2} \right\} = -\bar{b} = -E \cdot \{q\} = -E \cdot \left\{ \frac{\varepsilon_3 - \varepsilon_1}{2} \right\} = E \cdot \varepsilon_1 \quad (3.11)$$

$$u_r(r, \theta) = 2 \cdot B_u(r) \cdot \cos 2\theta \quad (3.12)$$

$$u_\theta(r, \theta) = 2 \cdot C_u(r) \cdot \sin 2\theta \quad (3.13)$$

Again, the strain can be calculated from the displacement data using equation 3.8. If the hole is eccentric, then the absolute values of  $\varepsilon_1$  and  $\varepsilon_3$  are no longer equal and they need to be calculated separately.

### 3.2 Calculation of coefficients for orthotropic materials

In the case of orthotropic materials, coefficients can be obtained from a complete 3D model (see Figure 3.5). Since the material is not isotropic, the material data for  $E_{11}$ ,  $E_{22}$ ,  $E_{33}$ ,  $G_{12}$ ,  $G_{13}$ ,  $G_{23}$ ,  $\nu_{12}$ ,  $\nu_{13}$ , and  $\nu_{23}$  was used. In this study, out-of-plane material properties are used because, during measurements non-uniform, in-depth stress profiles are expected. If only in-plane elastic constants are used in the finite element analysis, then it is implicitly assumed that the material is under plane stress. This is not true for in-depth, non-uniform stress analysis. An in-depth, uniform residual stress state is only a special case. Concerning the reinforced-polypropylene composite PURE, data is available in literature for the unidirectional reinforced polypropylene [Alcock 2006], and properties are also listed for a woven tape composite with a tape orientation  $[0^\circ/90^\circ]$  like the one used in this study. However, the number of stack plies and processing conditions were a little different, so that it was necessary to measure the elastic constants with a tensile test. The values of the elastic constants are listed in Table 3-1. The measured woven tape was composed of 32 plies compressed at 3 bars at a temperature of about 165 °C. The final thickness of the sample was about 4 mm. In Table 3.1, the asterisks \* mean that the values are estimated. In attachment A, explanations are available regarding how different elastic constants were calculated. For example, in the case of the unidirectional composite for which transversal isotropic behaviour was assumed, the shear modulus  $G_{23}$  equalled  $G_{23} = 0.5 E_{22} / (1 + \nu_{23}) = 0.55$  GPa.

**Table 3.1.3 : Elastic properties of a self-reinforced polypropylene composite.**

| Sample   | Tensile Modulus (GPa) |          |          | Poisson's Ratio |            |            | Shear Modulus (GPa) |          |          |
|--|-----------------------|----------|----------|-----------------|------------|------------|---------------------|----------|----------|
|  | $E_{11}$              | $E_{22}$ | $E_{33}$ | $\nu_{12}$      | $\nu_{13}$ | $\nu_{23}$ | $G_{12}$            | $G_{13}$ | $G_{23}$ |
| Unidirectional all-polypropylene composite                   | 12.95                 | 1.52     | 1.52     | 0.38            | 0.38*      | 0.38*      | 0.8                 | 0.8*     | 0.55*    |
| $[0^\circ/90^\circ]$ self-reinforced polypropylene composite | 5.5                   | 5.5*     | 1.5*     | 0.1             | 0.38*      | 0.38*      | 0.95                | 0.64*    | 0.64*    |

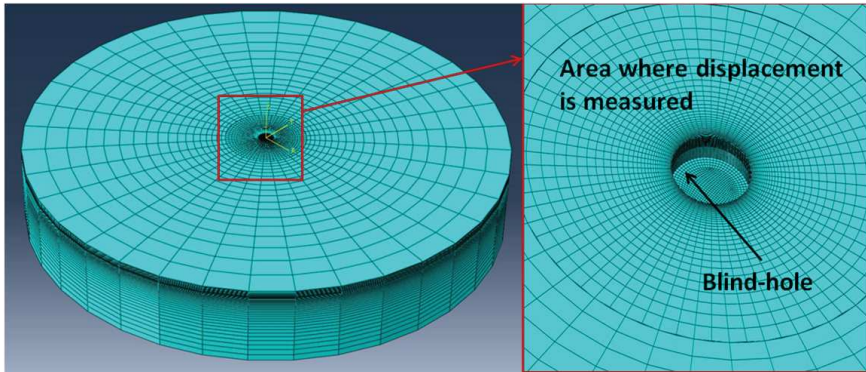


**Figure 3.5** Model used to calculate calibration coefficients for orthotropic materials. A blind hole is incrementally introduced and displacements are exported near the hole.

In chapter 3.1.1, an optimization of the calculation time was proposed by performing only one simulation with the load case  $\sigma_x$ . This optimization is not applicable with orthotropic materials, and, generally, each load case  $\sigma_x$ ,  $\sigma_y$ ,  $\tau_{xy}$  needs to be simulated separately. As the form of the displacement field is no longer a trigonometric function [Baldi 2007, Schajer 1994], exporting the displacement data from the whole surface is recommended for each load case. Later, these displacements can be interpolated at the desired position while taking the strain gauge geometry, position and eccentricity into consideration. Having determined the displacement field, it is then possible to calculate the strain at each strain gauge grid position (equation 3.8), and, then, the matrices  $C_{kl}$  can be deduced (equation 2.17). For example, using a load  $\sigma_x$ , the strain  $\varepsilon_1$  is obtained from the displacement data, and the coefficient  $C_{11}$  can be calculated. This can also be done incrementally in the same manner as for the isotropic case. If a load  $\sigma_x$  is only applied on the 6<sup>th</sup> increment and if 9 increments are removed by measuring the strain  $\varepsilon_1$  of the strain gauge, the coefficient  $C_{1196}$  can be obtained.

In conclusion, if using strain gauges, the orthotropic case does not present particular difficulties in comparison to the isotropic case. Each load case needs to be calculated separately in a complete 3D model. This increases the calculation time, which is why particular efforts should be invested in the optimization of the meshing of the model. Also, the accuracy of the result will definitely depend on the accuracy of the elastic constants of the material used in the finite element analysis. The calculation time for all  $C_{ij}$  matrices for 25 increments (975 simulations) takes about 1 week.

### 3.3 Calculation of coefficients for hybrid structures

The calculation of the calibration coefficients for hybrid structures is similar to the orthotropic or isotropic case. The fact that the material is composed of different layers, which are homogeneous but not necessarily isotropic, is taken into

consideration. After allocating the elastic properties to each layer, the matrices  $\bar{a}$  and  $\bar{b}$  (isotropic layers) or  $\bar{C}$  (orthotropic layers) are calculated using the same method as in chapters 3.1 or 3.2. [Held 2013] provides some information for metallic materials with coatings which can be used to anticipate the need of a new model depending of the geometry of the coating and the difference in elastic properties between the coating and the substrate. If the coating and the substrate material have a similar Young's modulus (a difference of less than 20%), then a new model is not necessary.

### 3.3.1 Example 1: Hybrid structure

In chapter 5.4 measurements are carried out on a hybrid structure made of a 1 mm thick sheet of aluminium and a 1 mm thick sheet of reinforced polypropylene (Figure 3.6). The model is equivalent to a component made of two layers. A finite element model was used which takes the thickness of the aluminium and the thickness of the reinforced polypropylene into consideration as well as the elastic constants of each structure, e.g.,  $E=70$  GPa and  $\nu=0.33$  for aluminium. The elastic properties of the reinforced polypropylene composite tape are the same as described in chapter 3.2. When performing measurements on the reinforced polypropylene, it is important to have calibration coefficients which take the stiffening effect of the sheet of aluminium on the backside into account. In contrast, modelling the reinforced polypropylene on the backside of aluminium does not influence the results of residual stress measurements for aluminium, because the stiffness of the reinforced polypropylene is negligible in comparison that one of aluminium.

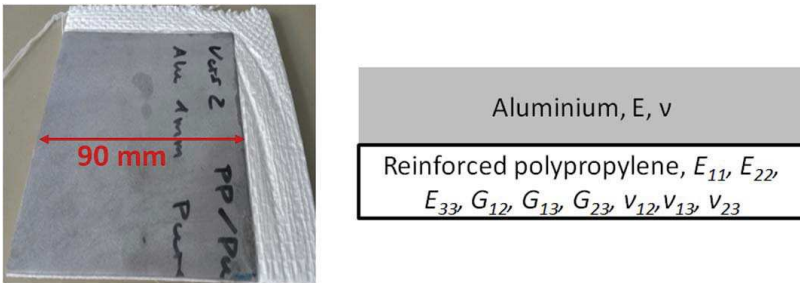


**Figure 3.6** Hybrid-structure made of a 1 mm sheet of aluminium and a 1 mm self-reinforced polypropylene. The right side shows the elastic constants used to model each structure.

### 3.3.2 Example 2: Semi-crystalline material

The second example concerns an injection moulded polypropylene. This process is characterized by freezing the outer layer (see chapter 2.1.1) and inducing an amorphous morphology at the surface. However, the core of the material is semi-crystalline, because crystals have more time to develop (Figure 2.5). The whole structure is characterised by a relatively constant crystallinity ratio in the core and a high gradient near the surface [Housmans 2009], as well as different spherulite sizes

(Figure 2.5). As a consequence, polypropylene samples are similar to multi-layer materials, each layer having different isotropic elastic properties. Therefore, the finite element model is composed of different layers and takes the elastic property gradient of this structure into consideration. Figure 3.7 depicts a simplification of the polypropylene structure. Young's modulus is estimated from moduli of indentation measured with nano-indentation for the real component [Persson 2014, VanLandingham 2001]. The average value along the depth of the sample is proportionally adjusted so that it corresponds with the common Young's modulus measured from tensile test ( $E=1300$  MPa). In Figure 3.8, the measured in-depth profile of the moduli of indentation can be seen. In order to obtain this result, a cross section of the material was embedded and polished with  $0.05\ \mu\text{m}$  alumina suspension MasterPrep (Buehler). The ultra-fine polishing is an important requirement for nano-indentation, because the maximum indentation depth is about  $1\text{-}2\ \mu\text{m}$ , and, therefore, the roughness needs to be as low as possible to limit scattering of the results. Measurements were made with the micro-hardness measurement instrument Fischerscope. A force of  $15\ \text{mN}$  was applied, the loading and unloading time was  $20\ \text{s}$ , and the maximum load was held  $40\ \text{s}$  long.

This gradient in the elastic property should have a strong influence on the results as moduli of indentation are of about  $60\ \%$  different between the skin and the core of polypropylene. In fact, it is evident in Figure 3.8 that the material becomes stiffer in the core. Near the surface, the stiffness is about  $1400\ \text{MPa}$ , at a depth of  $0.6\ \text{mm}$  the stiffness is approximately  $2100\ \text{MPa}$ , and in the core the stiffness is about  $2300\ \text{MPa}$ . The red curve represents the average modulus of indentation -  $2130\ \text{MPa}$ . This value is different compared to the one measured with a tensile test,  $1300\ \text{MPa}$ , and, therefore, all moduli of indentation were proportionally reduced as an approximation to match the tensile test. Figure 3.7 shows a simplification of the sample with a partition in three parts and takes the real value from the tensile test into consideration. The model used in this study uses a partition in the region near the surface (first  $0.8\ \text{mm}$ ) in 25 layers. The influence on the result will be discussed in chapter 5.3.3.

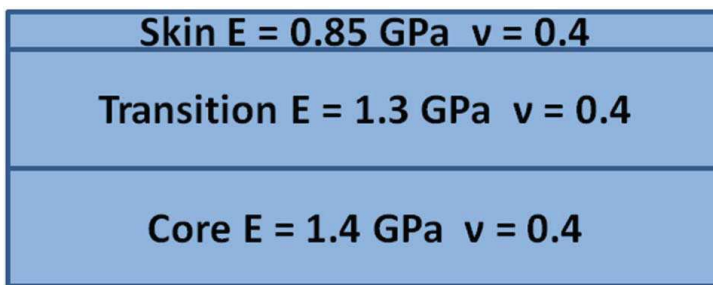


**Figure 3.7** Structure of polypropylene. The material is separated into 3 layers to highlight the difference in elastic properties of the structure.



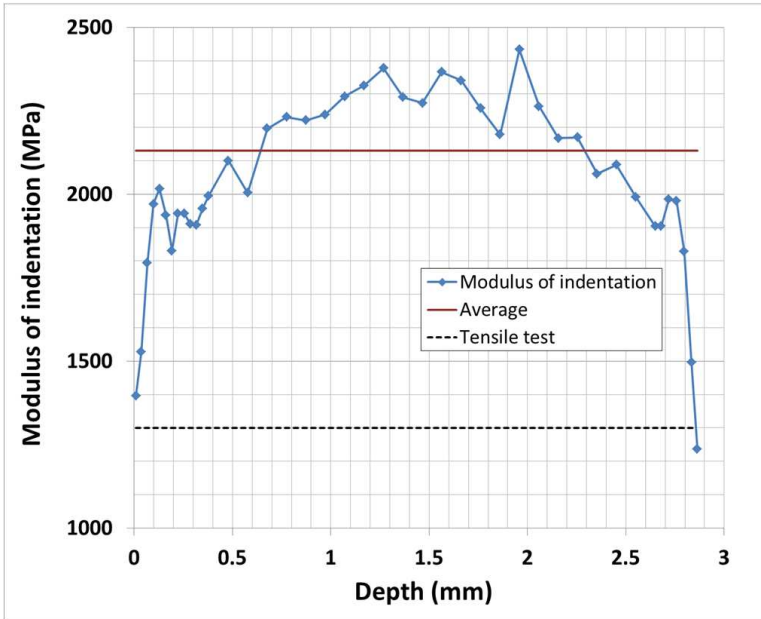


Figure 3.8: Profile of modulus of indentation along the depth of an injection moulded polypropylene. Red: average value of the moduli of indentation. A comparison with the value measured in tensile testing is illustrated by the dotted line.

### 3.4 Important parameters for the simulation

#### 3.4.1 Thickness of the sample

The standard [ASTM 2013] provides information on how to measure in-depth, non-uniform residual stress states in thick materials. Thick materials are defined as having at least the same thickness as the diameter of the gauge circle. For strain gauges designed for a 2 mm diameter hole, this is usually around 5 mm. No coefficients are proposed for non-uniform, in-depth residual stress evaluations for samples thinner than 5 mm. Evaluation formalism is proposed for materials thinner than 1 mm with the assumption that residual stresses are uniform in their depth, which, however, is generally not the case. When working with polymer materials, the thickness is often less than 5 mm, making it necessary to take the thickness of the material into consideration. In Table 3.2, the coefficient matrices  $\bar{a}$  and  $\bar{b}$  were calculated for components with thicknesses of 0.7 mm/1 mm/2 mm and 6 mm. A strain gauge type EA-062RE (Vishay Micro-Measurement) is listed with a hole diameter of 2 mm and a material with a Poisson's ratio of 0.3. As can be seen, there is a strong difference between each model, which is why major errors are expected if wrong coefficient matrices are used. This will be discussed in further detail in chapter 5.4.1. It is also interesting to note that coefficients in matrices  $\bar{a}$  and  $\bar{b}$  are higher in thin materials,

which means that higher deformations are expected during experimental testing with thinner materials. This is advantageous for measurements of residual stresses in thin components.

**Table 3.4.12: Coefficients for application of the hole drilling method near the surface for different component thicknesses. A strain gauge type EA-062RE, a Poisson's ratio of 0.3 and a hole diameter of 2 mm were used.**

Thickness 0.7 mm  
-a·10<sup>6</sup>

| Depth (mm) | 0.02 | 0.04 | 0.06 | 0.08 | 0.1  |
|------------|------|------|------|------|------|
| 0.02       | 6736 |      |      |      |      |
| 0.04       | 7551 | 7015 |      |      |      |
| 0.06       | 8306 | 7804 | 7204 |      |      |
| 0.08       | 9030 | 8522 | 7979 | 7326 |      |
| 0.1        | 9726 | 9206 | 8669 | 8087 | 7391 |

Thickness 1 mm  
-a·10<sup>6</sup>

| Depth (mm) | 0.02 | 0.04 | 0.06 | 0.08 | 0.1  |
|------------|------|------|------|------|------|
| 0.02       | 4628 |      |      |      |      |
| 0.04       | 5117 | 4817 |      |      |      |
| 0.06       | 5559 | 5290 | 4950 |      |      |
| 0.08       | 5977 | 5712 | 5420 | 5045 |      |
| 0.1        | 6377 | 6110 | 5829 | 5513 | 5111 |

Thickness 2 mm  
-a·10<sup>6</sup>

| Depth (mm) | 0.02 | 0.04 | 0.06 | 0.08 | 0.1  |
|------------|------|------|------|------|------|
| 0.02       | 2523 |      |      |      |      |
| 0.04       | 2788 | 2653 |      |      |      |
| 0.06       | 3024 | 2913 | 2747 |      |      |
| 0.08       | 3245 | 3139 | 3011 | 2816 |      |
| 0.1        | 3456 | 3350 | 3231 | 3085 | 2866 |

Thickness 6 mm  
-a·10<sup>6</sup>

| Depth (mm) | 0.02 | 0.04 | 0.06 | 0.08 | 0.1  |
|------------|------|------|------|------|------|
| 0.02       | 2375 |      |      |      |      |
| 0.04       | 2625 | 2500 |      |      |      |
| 0.06       | 2845 | 2745 | 2587 |      |      |
| 0.08       | 3050 | 2955 | 2836 | 2649 |      |
| 0.1        | 3243 | 3148 | 3041 | 2903 | 2691 |

Thickness 0.7 mm  
-b·10<sup>6</sup>

| Depth (mm) | 0.02 | 0.04 | 0.06 | 0.08 | 0.1  |
|------------|------|------|------|------|------|
| 0.02       | 7481 |      |      |      |      |
| 0.04       | 8136 | 7779 |      |      |      |
| 0.06       | 8715 | 8422 | 7982 |      |      |
| 0.08       | 9259 | 8982 | 8631 | 8122 |      |
| 0.1        | 9778 | 9507 | 9183 | 8781 | 8217 |

Thickness 1 mm  
-b·10<sup>6</sup>

| Depth (mm) | 0.02 | 0.04 | 0.06 | 0.08 | 0.1  |
|------------|------|------|------|------|------|
| 0.02       | 6055 |      |      |      |      |
| 0.04       | 6536 | 6298 |      |      |      |
| 0.06       | 6957 | 6771 | 6470 |      |      |
| 0.08       | 7351 | 7179 | 6949 | 6595 |      |
| 0.1        | 7726 | 7560 | 7353 | 7084 | 6686 |

Thickness 2 mm  
-b·10<sup>6</sup>

| Depth (mm) | 0.02 | 0.04 | 0.06 | 0.08 | 0.1  |
|------------|------|------|------|------|------|
| 0.02       | 4829 |      |      |      |      |
| 0.04       | 5199 | 5050 |      |      |      |
| 0.06       | 5525 | 5421 | 5216 |      |      |
| 0.08       | 5830 | 5739 | 5598 | 5346 |      |
| 0.1        | 6120 | 6034 | 5914 | 5740 | 5446 |

Thickness 6 mm  
-b·10<sup>6</sup>

| Depth (mm) | 0.02 | 0.04 | 0.06 | 0.08 | 0.1  |
|------------|------|------|------|------|------|
| 0.02       | 4700 |      |      |      |      |
| 0.04       | 5072 | 4936 |      |      |      |
| 0.06       | 5399 | 5310 | 5114 |      |      |
| 0.08       | 5705 | 5628 | 5500 | 5255 |      |
| 0.1        | 5995 | 5925 | 5818 | 5655 | 5365 |

### 3.4.2 Poisson's ratio

[Nau 2013] reported that the correct values of Poisson's ratio need to be used in the simulation. Similar results can be seen in Table 3.3 where near surface calibration coefficients were calculated for two different Poisson's ratios. The first  $a_{ij}$  and  $b_{ij}$  coefficients of a 1 mm thick plate (2 mm hole diameter) are presented. An error margin of about 10% is estimated for an equibiaxial stress state of the coefficient  $a_{ij}$  if the Poisson's ratio is not considered ( $\nu=0.3$  instead of 0.4). The  $b_{ij}$  coefficients are less affected.

**Table 3.4.2: Comparison between coefficients ( $-a_{ij} \cdot 10^6$  and  $-b_{ij} \cdot 10^6$ ) close to the surface for a 1 mm thick material with a Poisson's ratio of 0.3 and 0.4.**

| Matrix a $\nu = 0.3$ |      |      |      |      |      | Matrix b $\nu = 0.3$ |      |      |      |      |      |
|----------------------|------|------|------|------|------|----------------------|------|------|------|------|------|
| Depth (mm)           | 0.02 | 0.04 | 0.06 | 0.08 | 0.1  | Depth (mm)           | 0.02 | 0.04 | 0.06 | 0.08 | 0.1  |
| 0.02                 | 4628 | 0    | 0    | 0    | 0    | 0.02                 | 6055 | 0    | 0    | 0    | 0    |
| 0.04                 | 5117 | 4817 | 0    | 0    | 0    | 0.04                 | 6536 | 6298 | 0    | 0    | 0    |
| 0.06                 | 5559 | 5290 | 4950 | 0    | 0    | 0.06                 | 6957 | 6771 | 6470 | 0    | 0    |
| 0.08                 | 5977 | 5712 | 5420 | 5045 | 0    | 0.08                 | 7351 | 7179 | 6949 | 6595 | 0    |
| 0.1                  | 6377 | 6110 | 5829 | 5513 | 5111 | 0.1                  | 7726 | 7560 | 7353 | 7084 | 6686 |

| Matrix a $\nu = 0.4$ |      |      |      |      |      | Matrix b $\nu = 0.4$ |      |      |      |      |      |
|----------------------|------|------|------|------|------|----------------------|------|------|------|------|------|
| Depth (mm)           | 0.02 | 0.04 | 0.06 | 0.08 | 0.1  | Depth (mm)           | 0.02 | 0.04 | 0.06 | 0.08 | 0.1  |
| 0.02                 | 4019 | 0    | 0    | 0    | 0    | 0.02                 | 6278 | 0    | 0    | 0    | 0    |
| 0.04                 | 4484 | 4210 | 0    | 0    | 0    | 0.04                 | 6739 | 6504 | 0    | 0    | 0    |
| 0.06                 | 4911 | 4665 | 4353 | 0    | 0    | 0.06                 | 7141 | 6955 | 6661 | 0    | 0    |
| 0.08                 | 5320 | 5077 | 4808 | 4461 | 0    | 0.08                 | 7516 | 7344 | 7117 | 6772 | 0    |
| 0.1                  | 5717 | 5472 | 5212 | 4920 | 4544 | 0.1                  | 7872 | 7706 | 7501 | 7238 | 6852 |

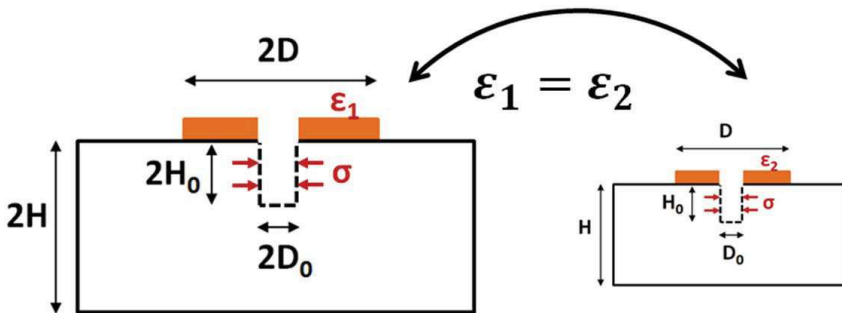
  

| Difference Matrix a |      |      |      |      |     | Difference Matrix b |      |      |      |      |     |
|---------------------|------|------|------|------|-----|---------------------|------|------|------|------|-----|
| Depth (mm)          | 0.02 | 0.04 | 0.06 | 0.08 | 0.1 | Depth (mm)          | 0.02 | 0.04 | 0.06 | 0.08 | 0.1 |
| 0.02                | 13%  |      |      |      |     | 0.02                | -4%  |      |      |      |     |
| 0.04                | 12%  | 13%  |      |      |     | 0.04                | -3%  | -3%  |      |      |     |
| 0.06                | 12%  | 12%  | 12%  |      |     | 0.06                | -3%  | -3%  | -3%  |      |     |
| 0.08                | 11%  | 11%  | 11%  | 12%  |     | 0.08                | -2%  | -2%  | -2%  | -3%  |     |
| 0.1                 | 10%  | 10%  | 11%  | 11%  | 11% | 0.1                 | -2%  | -2%  | -2%  | -2%  | -2% |

### 3.4.3 Model equivalence

In the standard [ASTM 2013], two corrections are proposed if the experiment does not match the geometry requirements exactly. The matrices  $\bar{a}$  and  $\bar{b}$  are calculated for a specific hole diameter  $d_0$ . If another diameter  $d$  with a value close to  $d_0$  is drilled, matrices  $\bar{a}$  and  $\bar{b}$  should be corrected with a factor  $d^2/d_0^2$ . Furthermore there

are three commercial sizes for strain gauge rosettes: one for drilling a 1 mm diameter hole e.g. EA-031RE (Vishay Micro-Measurements), one for a 2 mm diameter hole and one for a 4 mm diameter hole. Matrices  $\bar{a}$  and  $\bar{b}$  in the [ASTM13] are available for the medium-sized strain gauge, such as EA-062RE. When using the larger strain gauge model, such as EA-125RE, the calculation can still be made using the same coefficient matrices. In fact, the matrices  $\bar{a}$  and  $\bar{b}$  are the same if hole and increment sizes twice as large are drilled in a strain gauge rosette that is also twice as large. Equally, a smaller strain gauge can be used if the hole size and the increment size are reduced. Actually, this is not sufficient when working with thin material, because it is necessary to consider the material thickness. For example, drilling a 2 mm diameter hole in a 1 mm thick sample is the same as drilling a 4 mm diameter hole in a 2 mm thick sample with regards to the calibration coefficients and the strain relaxation around the blind hole. In sum, the hole diameter, increment sizes, strain gauge dimension and sample thickness should be increased or reduced in the same manner (see Figure 3.9).



**Figure 3.9** Model equivalence for the relaxed strain after drilling. Same strains  $\varepsilon_1$  and  $\varepsilon_2$  are measured due to the residual stress  $\sigma$  present in the removed increment.

### 3.5 Conclusion

In this chapter, it has been shown that in order to calculate residual stresses during a hole drilling measurement, calibration coefficients are required which correlate with measured strains and residual stresses. Some coefficients are available in [ASTM 2013], however, there are strong restrictions regarding the thickness of the sample, making it necessary to calculate specific coefficients for the present study. A step-by-step description was carried out to obtain these calibration coefficients. Furthermore, inhomogeneous, in-depth residual stress measurements near a joint or measurements in orthotropic structures are not covered sufficiently by other studies, which is why the integral method has been extended to such components in order to obtain a solution that is as exact as possible. The obtained calibration coefficients are then unique for each structure.

## 4 Elaboration of appropriate measuring strategies for polymer materials

In this chapter, how the application of the hole drilling method to plastic materials widely differs from metallic materials is shown. Possible sources of errors that can occur during the experiment are pointed out and analysed. Later, it will be possible to understand and critically assess the results from chapter 5, and to discuss the accuracy of the method.

Polymer materials have specific properties that differ from those of metallic materials, therefore, a measurement cannot be performed in the same way as usually recommended for metallic materials. Indeed, polymer materials have different thermal properties compared to metallic materials, namely a lower thermal conductivity and a higher thermal expansion coefficient. As a consequence, temperature fluctuations even of 1°C during measurement can lead to major errors in the result if their influence on strain measurements is not taken into account (chapter 4.3.1). For this reason, the experimental set-up should be adapted, e.g., drilling speed or feeding voltage of the strain gauge because they may heat the material locally [Nau 2015]. The adaptation of the experimental set-up also includes advice for cleaning the surface of components or gluing a strain gauge if working with material with a low surface energy, e.g. polypropylene (chapter 4.2).

Furthermore, polymer materials have a low elastic modulus, which makes it possible for high deformations to occur during the drilling procedure. They also have viscoelastic behaviour; strains are time-dependent (chapter 4.3.2). Therefore, a pragmatic approach is required to decide how to measure the released elastic strain needed to calculate residual stresses.

Other sources of errors are residual stresses present in the strain gauge which disturb measurements near the surface of the material (chapter 4.3.3). These residual stresses may be formed during the processing of the strain gauges and may be also due to the bonding that forms between the strain gauge and the underlying sample. This effect is not present in metals, because they are stiff enough to withstand the deformations from the strain gauge. In addition, owing to the fact that the strain gauges are approximately as stiff as the investigated materials, a stiffening effect which reduces the strain field near the strain gauge locally occurs (chapter 4.3.4).

These different effects are focused upon in this chapter in order to better understand and evaluate their respective impacts on the results. Lastly, a pragmatic measurement procedure is introduced to compensate some sources of errors and to achieve reproducible and reliable measurements (chapter 4.4).

#### 4.1 Required accuracy of the measurement

To better estimate influences of strain errors, it is of importance to select the order of magnitude for evaluation and comparison of occurring strain distortions. The standard [ASTM 2013] indicates a necessary accuracy of  $1 \mu\text{m}/\text{m}$  for strain measurements, and this is based on technical experience with metallic materials. Polymer materials, such as polycarbonate, have residual stresses that are generally below 10 MPa after processes like injection moulding. Higher values can be found in quenched samples where high compressive residual stresses can be induced (see chapter 5.2.1). This value is very low compared with metallic materials, but it is still very important for polymer materials regarding material deformations and environmental stress cracking (see chapter 5.3.2 and figure 5.25). Due to the fact that polymer materials have a low elastic modulus, low residual stresses still induce strong deformations, which are comparable - if not higher - than deformations measured during experiments performed on metallic materials. For this reason, the requirement in the standard ASTM can also be considered a target for measurements in polymer materials. Figure 4.1 shows a simulated strain profile that corresponds to strains calculated from an equibiaxial, homogeneous residual stress state of 1 MPa in polycarbonate ( $E=2400 \text{ MPa}$ ,  $\nu=0.4$ ). After drilling 0.04 mm deep increments (diameter 2 mm), deformations between 2 and  $5 \mu\text{m}/\text{m}$  are expected after each increment. If one wishes to measure with an accuracy of about 1 MPa, a strain accuracy around  $1 \mu\text{m}/\text{m}$  seems reasonable. Therefore, when investigating different strain error sources that influence the results, strain errors of about  $1 \mu\text{m}/\text{m}$  should be a concern. Eventually, bigger increments can be drilled to reduce the required measurement accuracy, though it results in a loss of spatial resolution.

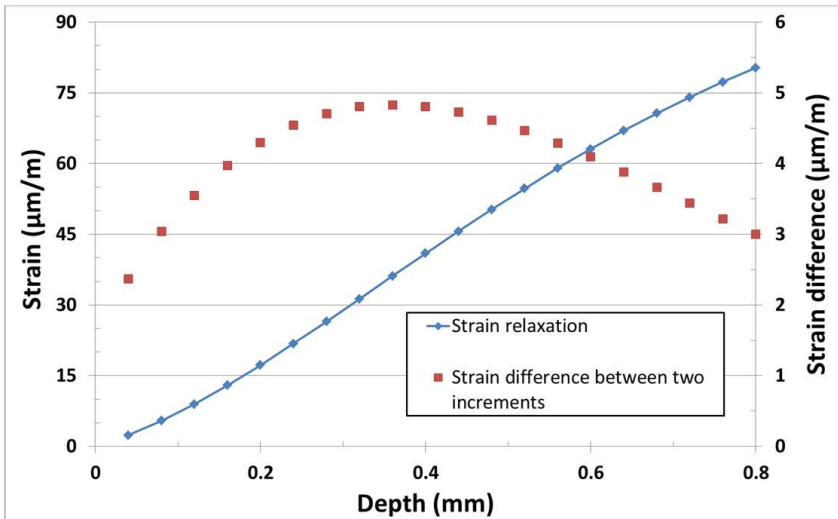
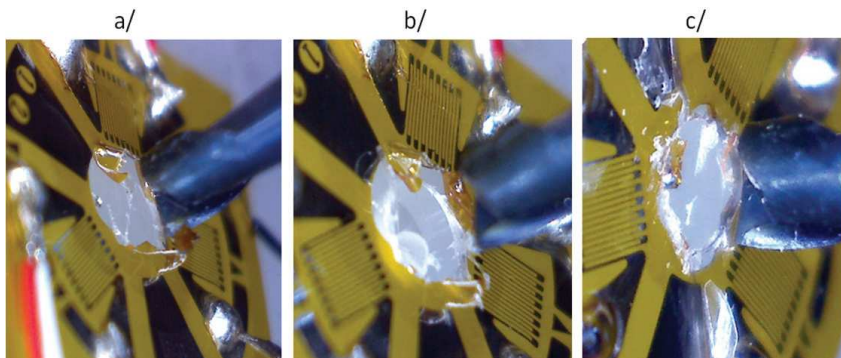


Figure 4.1: Simulated strain relaxation after drilling a polycarbonate sample while taking an equal-biaxial stress state of 1 MPa into account

## 4.2 Experimental set-up and sample preparation

In this study, three different materials are investigated: a polycarbonate, a polypropylene, and a self-reinforced polypropylene composite. Compared to metallic materials, they have low thermal conductivity, a lower resistance to solvent (acetone) and a low elastic modulus. [Nau 2011] illustrates how these characteristics can cause strong measurement errors if they are not taken into account correctly. First, before gluing the strain gauge, the sample needs to be cleaned with isopropanol or ethanol. Using acetone is not recommended as it may damage the surface of the material and, as a consequence, strong residual stress errors may be measured near the surface [Nau 2011]. Cyanoacrylate glue (CN and CN-R from TML Tokyo Sokki Kenkyujo Co.) is used to bond the strain gauge on the sample. Due to the low surface energy of polypropylene, a primer Loctite® 770 was used prior to doing so. When drilling and removing the foil of the strain gauge at the beginning of the measurement procedure, the strain gauge may become damaged, and interfacial unbonding can be observed (see Figure 4.2.a). This effect makes measurements unreliable as the strain transfer from the sample to the strain gauge is influenced. In this case, the foil is even removed far from the hole (figure 4.2.b). This effect happens when the bonding between the strain gauge and the material is weak. To reduce the probability of tearing out the strain gauge, a coating such as M-Coat A (Vishay Micro-measurements) should be applied on the strain gauge (Figure 4.2.c). This coating is a good compromise to reduce tearing out the strain gauge without bringing in too much stiffness. To further improve the adhesion between the strain gauge and the material surface, UV light was also used

before applying the primer. UV light uses low energy and changes the molecular organic bonds at the surface, increasing the contact angle and the surface energy. In doing so, a clean removal of the strain gauge foil was achieved (Figure 4.9).



**Figure 4.2: Removing of the strain gauge foil. Local unbonding occurs when the adhesion between the strain gauge and the sample is weak. In Figure (a), only the foil of the gauge has been removed. In (b), the sample was further drilled into up to 0.8 mm. In (c) only the foiled was drilled, minor improvement of the foil cracking was achieved through the use of a coating.**

Due to the low thermal conductivity of polymer materials, the feeding voltage of a strain gauge needs to be reduced to 0.5 V. If a stronger feeding voltage is used, the heat under the strain gauge cannot be diverted, and the temperature will rise. After connecting the strain gauges, it is necessary to wait for a thermal equilibrium to be established. For this purpose, experiments should be performed after a certain waiting period; in this study, we waited more than two hours before performing a measurement. Note that one hour is the minimum time required to obtain a stable signal before carrying out an experiment on metal.

Furthermore, the drilling speed of the cutter needs to be reduced. Usually 300,000 rpm are used with metallic materials, however such a speed melts polymer materials [Nau 2011, Casavola 2017]. To avoid heating, holes were manually drilled with a rotation rate of less than 60 rpm. As a result, heating induced by the cutter can be neglected during experiments. Lastly, because strain measurements with polymer materials are time-dependent (chapter 4.3), increments were drilled in a material every ten minutes. This enables better analysis and comprehension of the causes of time-dependent effects in order to be able to compensate them (chapter 4.4).

In this study, strain gauges are used to measure strains. Another possibility is the use of optical methods to measure displacement fields. These systems allow some problems inherent to the strain gauge technology to be avoided, such as the residual stress in the strain gauge (chapter 4.3.3) or the stiffening effect (chapter 4.3.4).



However, strain gauges are a robust technology which has the benefit of being based on much more extensive knowledge and experience than optical systems. Furthermore, we decided to closely investigate what happens during an experiment with a fast measurement rate, even while drilling. This makes the strain gauge technology a more suitable choice for first investigations. Results from this study can still be extrapolated to the other technologies. If optical methods are improved regarding their spatial resolution and robustness, then they should be able to improve obtainable results, especially near surface measurements in the first tenth millimetre.

### 4.3 Influencing factors

In this chapter, the main sources of errors are discussed. The first part deals with temperature fluctuations, then the focus shifts to how the drilling procedure also influences strain measurements. Another aspect is the presence of residual stress in the strain gauge, which particularly reduces the accuracy of near surface measurements in the first tenth millimetre. Lastly, the stiffening effect is explained, showing that strain measurements are lowered due to the presence of the strain gauge, which restrains deformations.

#### 4.3.1 Influence of thermal fluctuations during the experiment

When using strain gauges, it is possible to compensate most temperature fluctuations near room temperature by selecting an appropriate strain gauge type. For residual stress analysis performed on metallic materials, two common models exist for application on materials with different thermal expansion coefficients -  $\alpha$ : EA-06-062RE or EA-13-062RE. The first one is for application on ferritic steel  $\alpha \approx 11$  ( $\mu\text{m/m}/^\circ\text{C}$ ), and the second one is for application on aluminium  $\alpha \approx 23$  ( $\mu\text{m/m}/^\circ\text{C}$ ). In this study, measurements were performed on polypropylene with  $\alpha \approx 120$  ( $\mu\text{m/m}/^\circ\text{C}$ ) and polycarbonate with  $\alpha \approx 60$  ( $\mu\text{m/m}/^\circ\text{C}$ ). Therefore, the standard strain gauges for residual stress analysis are expected to be influenced by temperature fluctuation. Heating is of great concern, because a small temperature increase of about  $1^\circ\text{C}$  can induce an expansion bigger than  $60 \mu\text{m/m}$  when a measurement with an accuracy of about  $1 \mu\text{m/m}$  is required (chapter 4.1). Note that the measured expansion may actually be lower than the expansion of the pure material simply because the system strain gauge / sample reacts differently.

In order to compensate temperature fluctuations, connecting strain gauges in a half-bridge configuration with a second strain gauge glued on the same sample or another sample of the same material is generally recommended. This second strain gauge is then only influenced by temperature fluctuations, and, thus, can compensate its influence. This solution was not chosen for this study due to the fact that it is unable to perfectly compensate thermal expansion, because thermal expansion of the system polymer material/strain gauge is quite random near room temperature. In fact, Figure 4.3 shows the measured minimum, maximum and average thermal strain from 12

identical strain gauges glued on four polypropylene samples. It is evident that the thermal strain always correlates with the temperature measured with a thermocouple. However, there are strong differences between the strain values from each strain gauge. Therefore, to measure strain with very high accuracy, it is not enough to compensate thermal strains with another strain gauge. For example, after the 50 first minutes there is already a  $30 \mu\text{m}/\text{m}$  strain shift between the minimum and maximum thermal strains. The differences determined in this experiment were mostly random, and, in general, thermal expansion is also influenced by the material anisotropy and direction of the strain gauge. This investigation does not disprove the compensation of thermal expansion with a second strain gauge for general application, however, this compensation is not accurate enough for the hole drilling method.

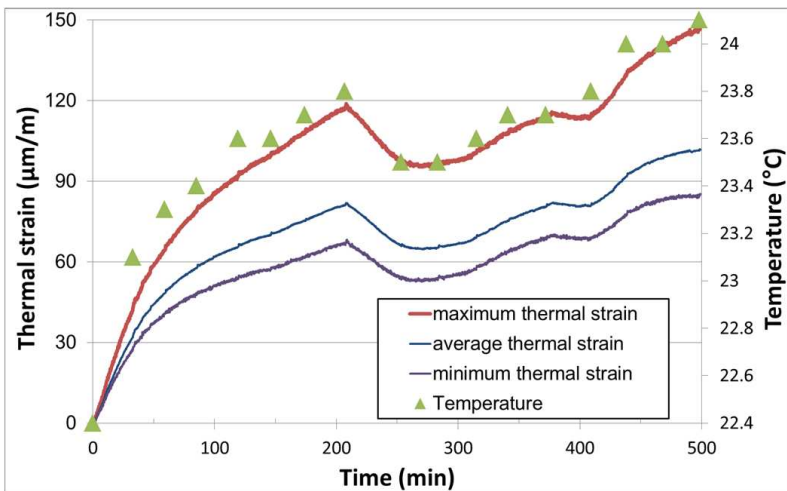


**Figure 4.3: Correlation between temperature fluctuation and thermal strains measured with 12 strain gauges glued on 4 polypropylene samples**

If a second strain gauge is still applied to compensate part of the thermal expansion, the orientation between the strain gauges and material should be considered to take the material thermal anisotropy into account [Ajovalasit 2011]. This anisotropy was observed in the case of injection moulded polypropylene with carbon black content. Figure 4.4 shows the measured anisotropic thermal strains for this sample. The strain gauge was connected to an amplifier at the time  $t = 0$  min. No mechanical load was applied to the sample. From the time  $t = 1100$  min to  $t = 1300$  min, an operator worked in the laboratory. Note that during that time, the thermal strain increased as the temperature in the laboratory probably increased. Furthermore, the thermal expansion is lower in the length direction of the sample (strain gauge 1) and is almost four times stronger in the cross direction (strain gauge 3). This material anisotropy has been observed several times, which confirms the thermal anisotropy of this sample.

The last effect is the non-reversibility of thermal expansion. In Figure 4.5, the heating of polycarbonate can be seen. As an operator came close to the experimental set-up, strains were measured by the strain gauges. Because the strain gauges are free of any mechanical load, the measured expansions correspond to thermal strains induced involuntarily by the operator. This heating was measured with a strain gauge rosette, each strain gauge from the same strain gauge rosette did not measure the same strain value. Furthermore, the thermal strain did not return back to its initial value for all the strain gauges. Three heating cycles were repeated, and remaining strains up to  $3 \mu\text{m}/\text{m}$  were present each time. This non-reversibility may be due to local plasticity between the strain gauge grid and the surrounding polymer matrix. This effect can be neglected by simply increasing the distance between the experimental set-up and the user, or by using a polystyrene box to prevent influence from body heat. Still, it emphasized the necessity to keep the temperature in the laboratory as constant as possible and to avoid any source of heat, e.g. heat induced by the drilling process.

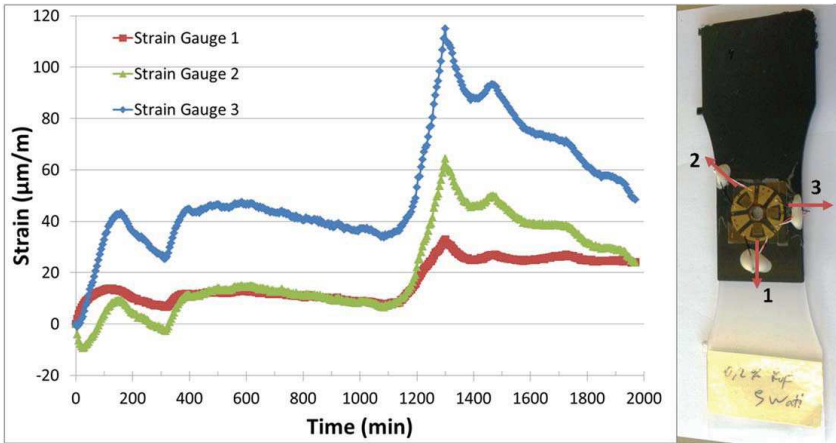


**Figure 4.4:** Thermal expansion of an injection moulded polypropylene with carbon black content over the course of 1.5 days.

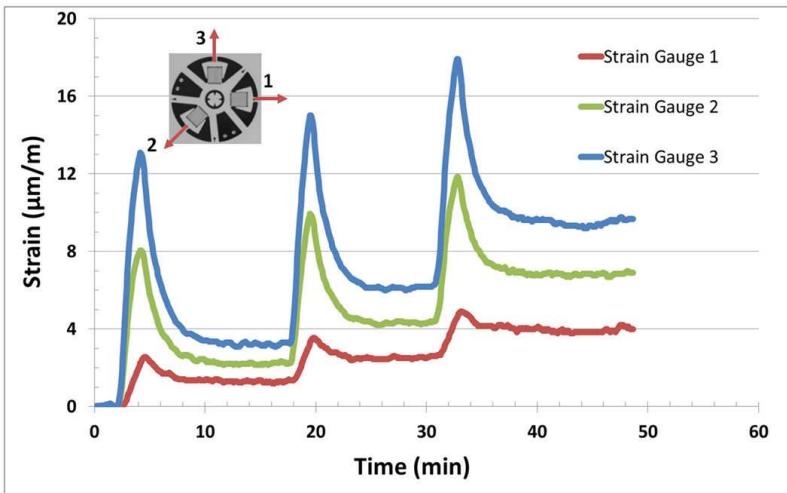


**Figure 4.5:** Thermal strain measured by a strain gauge rosette applied on a polycarbonate sample. Thermal strain was measured in the three directions of the rosette and is due to heating from an external source (operator). The heating cycle was reproduced three times.

In sum, polymer materials are sensitive to thermal fluctuations due to their high thermal expansion coefficient. The influence of some thermal sources can be neglected if care is taken, such as increasing the distance between the operator and the experimental set-up to remove the influence of body heat. Reducing the drilling rotation rate also prevents heating. Temperature fluctuations induce a non-reversible thermal strain, which is why it is recommendable to work in a closed laboratory with as stable of a temperature condition as possible. A part of thermal strain can be compensated using a second strain gauge free of mechanical load, and connected, for example, in a half-bridge configuration. Another possibility is to employ the procedure explained in chapter 4.4 assuming that slow temperature fluctuations are predictable in the ten minutes following data collection, e.g. the outside temperature fluctuation, or a radiator far away from the experimental set-up. This holds true when working in a closed laboratory with no unpredictable thermal influences such as the opening of a window during measurements.

#### 4.3.2 Influence of mechanical loading during measuring operations

During the drilling process, a cutter is manually rotated into the material with increment thicknesses of about 0.04 mm. In addition to the cutter pushing into the sample, the rotation of the cutter produces high shearing, which deforms the material in the surrounding of the hole. During the drilling process, deformations larger than 200  $\mu\text{m/m}$  can be measured (Figure 4.6). Deformations increase during drilling as the cutter continues to advance farther into the material. Since polymer materials do not

behave like elastic materials, viscoelastic phenomena occur during the drilling process (creeping). Consequently, the material will slowly recover after the drilling process. Usually, the viscoelastic strain becomes negligible after 2-4 minutes, and we do not recommend measuring the relaxed strain to calculate the residual stresses before this time has passed. In fact, in order to calculate the residual stresses, one should select the relaxed elastic strain. At first thought, elastic strain may be obtained directly after drilling. In Figure 4.6, the strain is  $-31 \mu\text{m/m}$  at the time  $t_2$  shortly after drilling, then it becomes respectively  $-13 \mu\text{m/m}$  after 4 seconds,  $-6 \mu\text{m/m}$  after 12 seconds and  $-3 \mu\text{m/m}$  after 2 minutes. The strain rate is too fast after drilling to allow the accurate selection of an elastic strain. Moreover, the viscoelastic strain during the drilling procedure influences the measured strain directly after drilling. Therefore, it is not possible to obtain the elastic strain by measuring the strain directly after drilling. As is evident, it is necessary to develop a pragmatic solution which takes the viscoelastic behaviour of polymer materials into consideration, to achieve accuracy of about  $1 \mu\text{m/m}$  for the relaxed elastic strain.

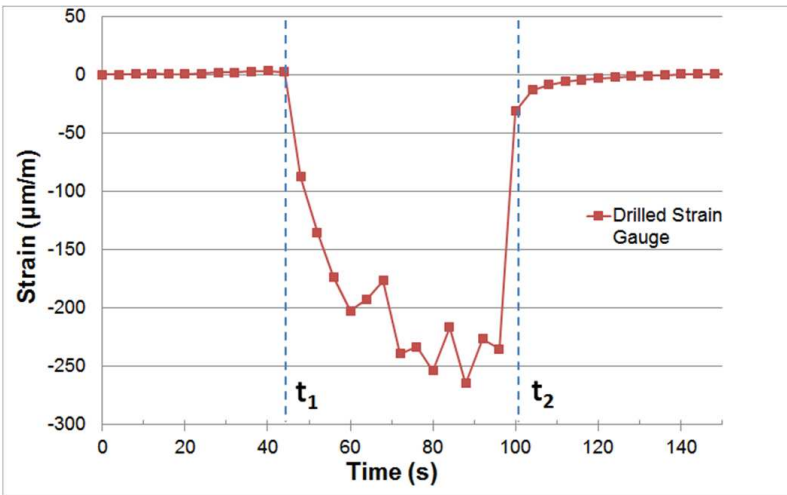


**Figure 4.6: Deformation during drilling process. Drilling process begins at the time  $t_1$  and ends around the time  $t_2$ .**

Furthermore, Figure 4.7 shows that the mechanical load induces irreversible deformations. In this case, a cutter was pushed into the sample, but without drilling and removing material. As a result, the measured deformations after removing the cutter were not due to initial residual stresses in the material. In Figure 4.7, a low strain increase can be noticed at the beginning of the experiment. This effect was caused by the increasing temperature in the laboratory. After three minutes, the cutter was pushed into the material, which, in turn, induced a deformation of about  $-170 \mu\text{m/m}$ . The deformation was maintained for 30 seconds and then the cutter was

removed. The material recovered quickly within  $t = 4$  minutes and  $t = 5$  minutes. Later, a constant strain rate is visible, which is again related to the increasing temperature in the laboratory. Looking at the profile of the strain before and after drilling, it is evident that the strain signal shifts by about  $3 \mu\text{m}/\text{m}$ . This experience was reproduced twice under similar conditions and strain shifts of about  $1 \mu\text{m}/\text{m}$  were measured. The remaining strain results in a loss of accuracy for the hole drilling method. Figure 4.8 depicts to which extent this error could influence the result. A sample free of residual stress was examined, then, after drilling each increment, it was assumed that a  $3 \mu\text{m}/\text{m}$  strain error was measured, which represents the worst observed case. The material used for this simulation was a polycarbonate with  $E=2400 \text{ MPa}$  and  $\nu=0.4$ . Figure 4.8 shows that residual stresses are at their maximum near the surface and half of errors are self-compensated around a depth of about  $0.3 \text{ mm}$ . The residual stresses inside the material increase, which means that a loss in accuracy is to be expected deep in the material in future experiments. These errors cannot be compensated precisely, because the remaining strains are random. Still, if possible, the amount of deformations during the drilling phase needs to be minimized to avoid influencing the result too much.

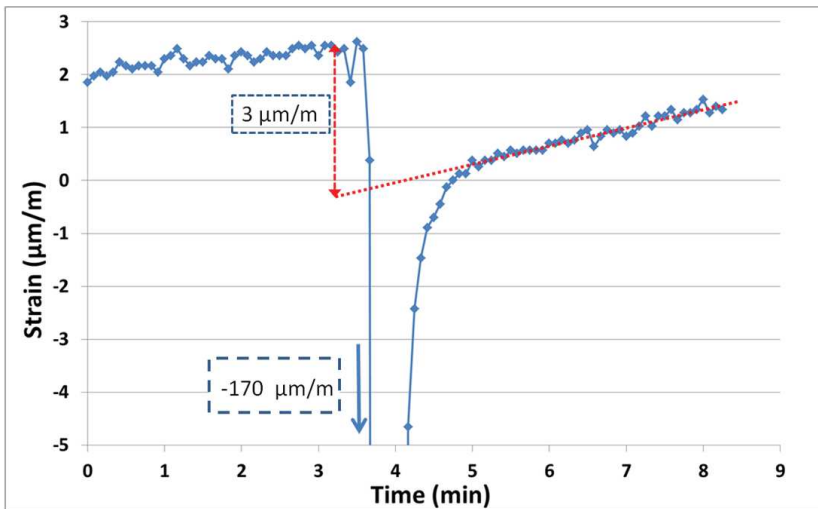


**Figure 4.7:** Strain measured after pushing and rotating a cutter into a polycarbonate sample without drilling the material.

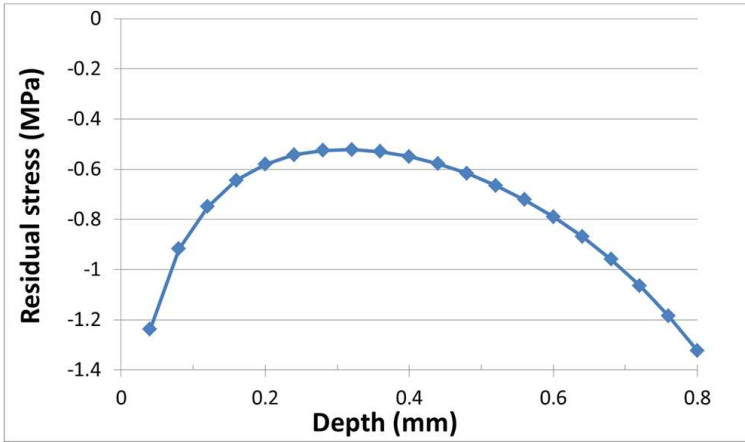


**Figure 4.8:** Residual stresses induced by strain errors of about  $3 \mu\text{m/m}$  after each drilled increment

#### 4.3.3 Setting the zero depth and stress in the bonding strain gauge / sample

Other errors are caused by the drilling tool during the removal of the foil in the centre of the strain gauge. First, errors are present for setting the surface of the sample as the reference, i.e. the definition of the zero depth. Figure 4.9 depicts the different steps to define where the cutter comes into contact with the surface of the sample. For the purpose of simplification, a little blue point was drawn on the surface of the sample before gluing the strain gauge rosette onto it. The dry ink does not influence the result, because it is not underneath the strain gauge grids. It was only applied for the visualisation of the zero setting in this example, but not during other experiments. In Figure 4.9, the foil was successively removed in steps of about  $5\text{-}10 \mu\text{m}$ . Using a camera makes it possible to see when the cutter actually comes into contact with the sample.

After removing the foil of the strain gauge, high deformations of about  $20\text{-}80 \mu\text{m/m}$  can be measured when working with polymer materials like polypropylene or polycarbonate. These deformations may be due to a combination of residual stresses contained in the strain gauge rosette, residual stresses building up between the strain gauge and the sample while gluing, and residual stresses induced by the curing of the epoxide coating protecting the strain gauge. These deformations are noticeable in polymer materials as the strain gauge rosette is applied on a material with a stiffness comparable to the rosette's stiffness.

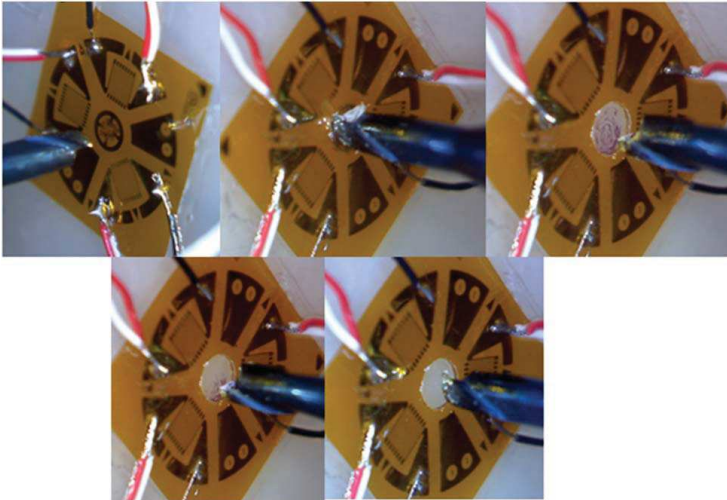


**Figure 4.9: Step-by-step removal of the strain gauge rosette foil. A little point was applied with dry ink to emphasize the location of the surface of the sample.**

In contrast, metallic materials are stiff enough and resist deformations induced by the strain gauge, so that almost no strains are measured after removing the foil. In polymer materials, these deformations are assumed to greatly influence results obtained near the surface. In fact, initial residual stresses present in an increment also influence the strain measured after the removal of the following increments (see chapter 2.3.1, figure 2.11). This effect is due to the loss of stiffness around the hole when the material is removed. Similarly, stresses in the strain gauge should presumably influence the strain measurements after drilling the material. The strains measured after removing the foil of the strain gauge are often larger than that measured after drilling 0.1 mm of material. As a consequence, when material near the surface is removed, the measured deformations grow due to the initial residual stresses in the material, but also due to the stresses in the strain gauge rosette. A way to compensate this error was not found in this study, and it may be the most important source of errors for measurements performed near the surface.

This error is emphasized in chapter 5.3 where a mechanical validation procedure of residual stress measurements was proposed by bending a sample. In this case, a known stress was induced in the strain gauge, and this effect has been schematised in Figure 4.10. After gluing a strain gauge into place, a sample is mechanically loaded by bending or stretching. In doing so, the component and the strain gauge are stretched, which induces a load stress in both the material and the strain gauge. As a consequence, if only the foil from the strain gauge is drilled, a strain is measured which corresponds to the relaxation of the load stress present in the strain gauge



rosette. For these experiments, two sizes of strain gauge rosettes were considered, one being twice the size of the other one. The small and medium size strain gauges are the references EA-06-062RE-SE and EA-06-031RE-SE by Vishay Micro-Measurements respectively. Samples were stretched up to 0.3% strain and the strain gauge rosettes were drilled with a hole diameter of 2 mm for the medium size strain gauge rosette and 1 mm for the other one. Following the removal of the foil of the strain gauge rosette, strain relaxations could be measured. They should have been the same seeing as both strain gauge rosettes are equivalent regarding strain relaxations (see chapter 3.4.3). However, a strain of about  $-110 \mu\text{m/m}$  was measured after drilling the foil of the medium size strain gauge and a strain of  $-280 \mu\text{m/m}$  was obtained for the small size strain gauge. These values are by far larger than usual strain relaxations obtained during residual stress measurement of samples which are free of any external load. The external stress induced by the load in the strain gauge rosette is the reason for these unusual strain relaxations, and it is the reason why measurements become unreliable. Furthermore, one can see that the relaxation after drilling the strain gauge foil is more important for the smaller strain gauge. The explanation for this can be seen in Figure 4.10, where the strain gauge EA-06-062RE-SE corresponds to the model (a) and the strain gauge EA-06-031RE-SE corresponds to the model (c). Regarding the strain relieved after drilling the foil of the strain gauge rosette, there is an equivalence between models (a) and (b), but not between (a) and (c). Both models (a) and (b) are equivalent as all dimensions are reduced by the same factor 2, e.g., diameter of the hole, dimension of the strain gauge, height of the strain gauge. However, in the case of real strain gauges, their height remains unchanged independent of the size of the strain gauge. As the height of the small strain gauge (c) is actually two times larger than the one in model (b), stronger deformation are obtained after drilling the foil of this small strain gauge (c). To reduce this effect, strain gauges should be glued after loading the sample if a load is present. Then, after drilling the foil of the strain gauge rosette, the measured relaxations was reduced up to  $20 \mu\text{m/m}$  for the small and medium size strain gauges. In conclusion, even the simple drilling of the foil of a strain gauge is an important step which should not be neglected. The strain relaxation measured after drilling the foil should be as small as possible to avoid influencing measurements of residual stresses near the surface.

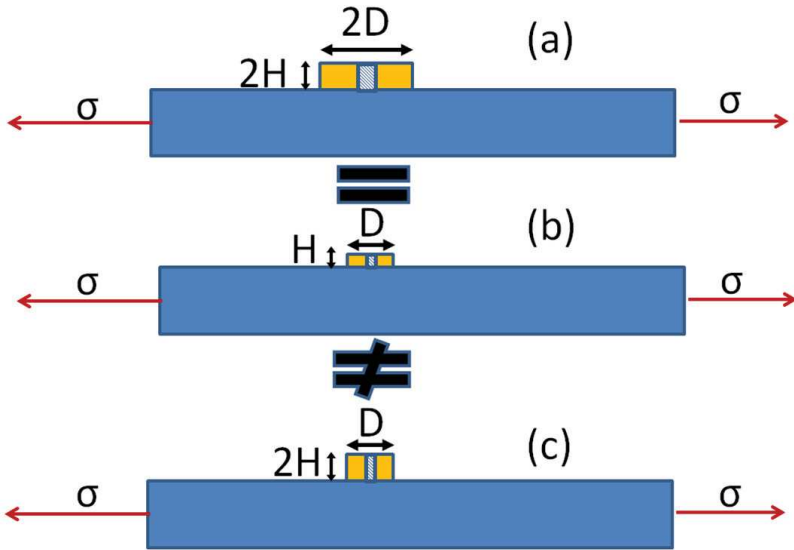


Figure 4.10: Strain equivalence in the case of a drilled strain gauge under a load. Model (a) and (c) correspond to a stretched sample with an applied strain gauge of the types EA-06-062RE-SE and EA-06-031RE-SE (Vishay Micro-Measurements) respectively. Model (b) shows the required dimension of the strain gauge needed to obtain a strain equivalence with model (a).

#### 4.3.4 Stiffening effects

The last source of errors investigated in this work is the stiffening effect. Strain gauges are generally designed to be applied on metallic materials. As a material expands, its deformation is transferred to the strain gauge. However, in the case of polymer materials, strain gauges have a comparable stiffness to the material. As a consequence, the strain gauge resists the deformations and strains are reduced locally. Some studies [Ajovalasit 2007-2013, Zike 2014] suggest that the stiffening effect depends on parameters such as the length of the strain gauge, Young's modulus, the thickness of the investigated sample, and the stiffness of the strain gauge. If this strain reduction is noticeable during tensile testing, it should also be present during a hole drilling experiment, meaning the measured residual stresses are proportionally reduced.

In this study, the stiffening effect was examined for different materials: an injection moulded polypropylene ( $E \approx 1400$  MPa), a polycarbonate ( $E \approx 2500$  MPa), and a self-reinforced polypropylene PURE ( $E \approx 5400$  MPa). Different strain gauges were investigated. The first were common strain gauges used for the hole drilling method, such as EA062-RE, EA125-RE with respectively a grid length of about 1.57 mm and 3.18 mm. The second was a standard linear strain gauge CEA-06-250UN-120 (Vishay

Micro-Measurements) with a grid length of 6 mm. The third was a strain gauge for the ring core method FR-5-11-JLT with a grid length of 5 mm. The fourth was a special linear strain gauge for applications with polymer materials GFLA-6-50 (TML, Tokyo Sokki Kenkyujo Co., Ltd.) with a grid length of 6 mm. Samples were stretched in a tensile test and strains were measured using different technologies: strain gauge, extensometer, and a video camera (GOM ARAMIS) positioned between two points spaced 8 cm. The ratio between the strain measured with the strain gauge and the two other methods was then incorporated into the function of the stiffness of the investigated sample (Figure 4.11). Based on the results in Figure 4.11, the strain measured for polycarbonate samples strain gauge is approximately 12% lower than that measured with an extensometer. This strain reduction increases in the case of polypropylene samples. Here, the strains are reduced by about 25% for small strain gauges with a grid length of 1.5 mm and 12 % for strain gauges with a grid length of 6 mm which were specially designed for low stiffness materials. Therefore, it is possible to deduct that using a strain gauge specially designed for polymer materials (GFLA-6-50) does improve the reliability of strain measurements. Regarding measurements performed on the self-reinforced polypropylene composite PURE, an even lower strain reduction was expected to be measured than for polycarbonate samples, because the material PURE is stiffer. This assumption was confirmed using a strain gauge with a grid length of 6 mm; the strain is only 5 % lower. However, this was not the case when the two other strain gauges were employed. The strains were reduced by at least 12 % for both polycarbonate and composite PURE.

Furthermore, the scattering of the results is even higher in the case of the self-reinforced polypropylene. This can be explained by the woven structure of the material, which tends to concentrate strains at the interlacement of warp and weft yarns [Skotarek 2014]. Figure 4.12 shows an example of a strain gauge glued on a self-reinforced polypropylene. The grids of the strain gauge are the same dimension as the weave. To reduce the scattering, it is necessary to use strain gauges which cover a larger area. This has been attempted using the strain gauge EA125-RE (3 mm), which is the largest size available for residual stress analysis using the hole drilling method. However, it did not result in any improvement. Better results were able to be achieved with strain gauges with a 6 mm grid length, but there is no strain gauge with those dimensions for residual stress analysis using the hole drilling method.

One possibility is the use of the ring core method with a strain gauge with a grid length of 5 mm. Yet, we were unable to obtain satisfying residual stress results in this study by applying the ring-core method to polycarbonate components, see Figures 5.3 and 5.5. In Figure 4.11, the Young's modulus of the reinforced polypropylene displays important scattering of obtained values. This is due to differences in the compacting temperature (160°C-180°C) during the processing of the samples, because the compacting temperature highly influences its properties [Heim 2011].

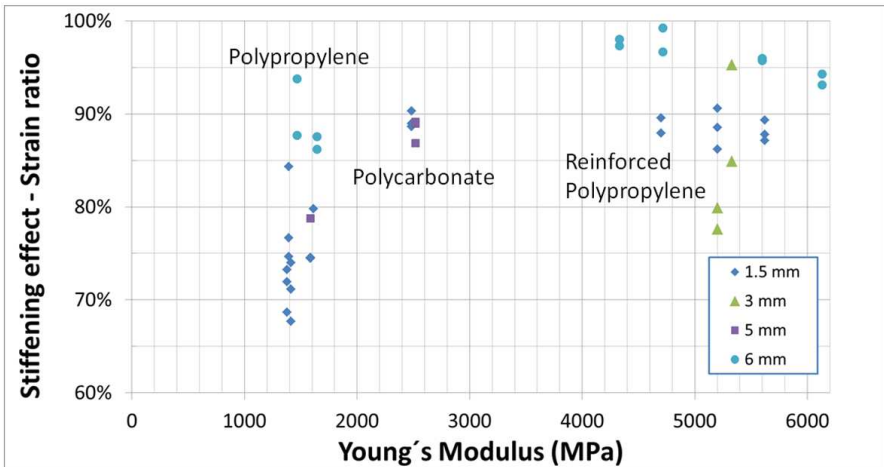


Figure 4.11: Stiffening effect in a function of Young's Modulus of the material. The stiffening effect is defined as the strain ratio between the strain measured with a strain gauge and the strain measured with a video camera (GOM ARAMIS) or with an extensometer. Strain gauges of different length were applied on polypropylene, polycarbonate, and self-reinforced polypropylene composite.

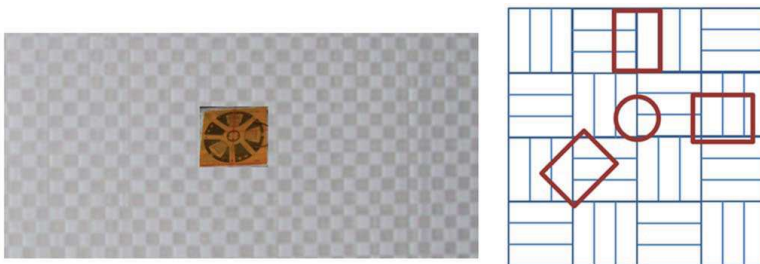
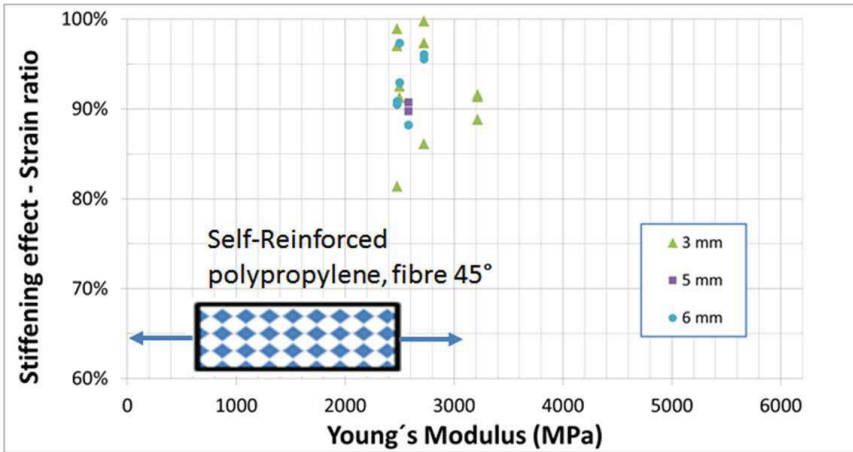


Figure 4.12: Self-reinforced polypropylene composite PURE with applied strain gauge rosette. The strain gauge dimension is of the same order of magnitude as the woven structure of the composite.

Another aspect is the accuracy of strain measurements obtainable for the self-reinforced polypropylene samples if the tensile test is operated at an angle of  $\pm 45^\circ$  to the fibre direction. The results can be viewed in Figure 4.13. The scattered results with a fibre orientation of  $\pm 45^\circ$  are similar to those with fibre orientations of  $0^\circ$  and  $90^\circ$ . The stiffening effect is about 10% again, but, in this case, the large strain gauges (5 or 6 mm) are not as efficient as when fibres are aligned with the tensile test direction and the strain gauge direction. The strain gauges should cover more weaves to reduce the scattering. Note that the Young's modulus of the material reduced to about 2.6 GPa

once the tensile direction was no longer aligned with the fibres and because the material is orthotropic.



**Figure 4.13: Stiffening effect in function of the Young's Modulus of the material. The stiffening effect is defined as the strain ratio between the strain measured with a strain gauge and the strain measured with a video camera (GOM ARAMIS) or with an extensometer. Strain gauges were applied to a self-reinforced polypropylene composite. The direction of the force applied in the tensile test is oriented by an angle of 45° to the direction of the sample reinforcement ("fibre direction").**

In conclusion, the strain reduced by about 10 % for polycarbonate and the self-reinforced polypropylene when applying strain gauges designed for residual stress analysis on metallic materials. The strain reduction increased by about 25 % for polypropylene because its stiffness is lower,  $E=1.4$  GPa. During hole drilling measurements in which the strains are measured with strain gauges, results should be proportionally increased to take the stiffening effect into account. Owing to the fact that the influence of the stiffening effect was obtained later on in this study, the results have not been corrected. However, the analyses of the results are still relevant because the profiles of residual stress states are not influenced by the stiffening effect.

#### 4.4 Evaluation procedure to take into account time dependent effects

In the present study, residual stresses are directly calculated from the measured elastic strains. Chapters 4.3.1-4.3.2 illustrated that measured strains are time-dependent, making it necessary to decide on a procedure that allows the selection of the correct elastic strains amount.

The elastic strains are needed to calculate residual stresses. These strains are usually measured directly after drilling when applying the hole drilling method on metallic materials. This is not the case with polymer materials. In fact, chapter 4.3.2 showed us

the sample crept due to the load induced by the cutter during the drilling phase. The total creep strain is composed of an elastic strain, a transient recoverable viscoelastic strain, and a permanent non-recoverable plastic strain. Non-recoverable strains have been neglected for simplification purposes. Due to the viscoelastic strains developing during the drilling phase, strains measured directly after drilling are not correct for evaluation of residual stresses as they do not only correspond to the relieved elastic strains. This effect is illustrated in Figure 4.7 where viscoelastic effects occurred without drilling the sample. Therefore, it is necessary to wait for the material to recover to measure the elastic strain. In other words, after some time, the previous viscoelastic deformation becomes negligible and the elastic strain can be measured. Furthermore, selecting a strain directly after drilling is arbitrary, and not possible in practice, because the strain rate is too high after drilling (chapter 4.3.2). In addition, the material is also affected by temperature fluctuations which are added to the mechanical elastic strain.

One way to correct the influence of temperature fluctuations is to remember that the temperature constantly increases or decreases at the same rate during a short 10-minute period, which is the period of time between two drilling increments. Figure 4.14 sums up the different effects that occur when drilling an increment. In the first five minutes, the strain signal increased, and this phenomenon was related to the temperature increase in the laboratory and the resulting material thermal expansion. Then, the sample was drilled, which induced strong deformations. After  $t \approx 6$  minutes, the cutter was removed and the sample recovered slowly from the viscoelastic deformations. Since the drilled material contained initial residual stresses, it underwent relaxation and the signal shifted accordingly. This relaxation is the elastic strain required for the hole drilling method. Finally, after  $t = 10$  minutes, the material had recovered and a similar strain rate as before drilling was identified.

This increasing strain can again be correlated with temperature fluctuations in the laboratory. The shape of the strain before drilling and several minutes after drilling appears to be similar, thus, confirming the assumption that temperature fluctuations are predictable during a relatively short period of time. Drilling an increment every 10 minutes is a good solution to make an experiment fast enough and to simultaneously be able to analyse how the strain signal behaves. In theory, the temperature should be kept perfectly constant during an experiment, however, good control of the thermal influencing factors is enough to ensure reliability of results.

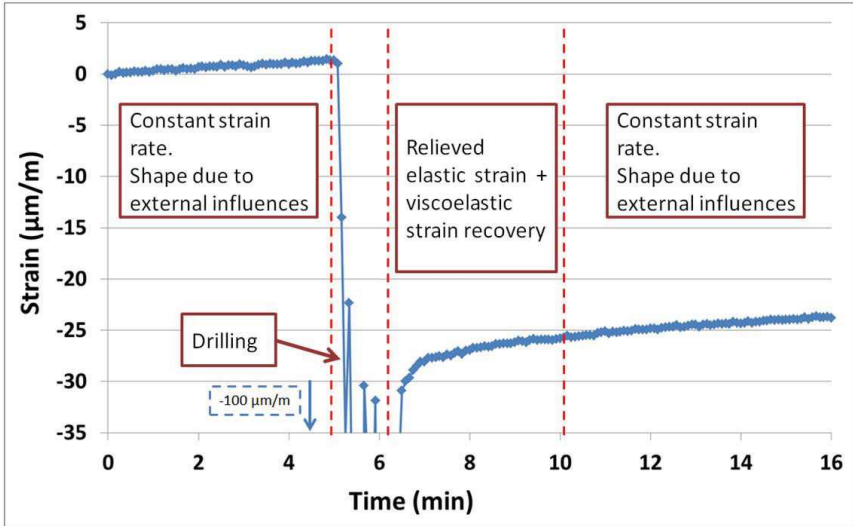


**Figure 4.14: Principal causes of strain that occur during a measurement with the hole drilling method. One increment is drilled at time  $t = 5$  min.**

Based on the above-shown information about strains measured during a measurement, it is possible to define the elastic strains required to calculate the residual stresses. Figure 4.15 shows a possible definition of the elastic strain. After  $t_1$ , viscoelastic strains are considered negligible and the strain signal is a superposition of thermal strain and the previously released elastic strain. The same is valid at  $t_2$ , however, the thermal expansion increases as time goes on. In order to remove the thermal strain, it is possible to extrapolate the signal to the time  $t_0$  with an affine interpolation, see equation 4.1. In doing so, the difference between the extrapolated value and  $Y_0$  is the required elastic strain released due the removal of material.

$$\varepsilon_{elastic} = Y_1 - Y_0 + \frac{Y_2 - Y_1}{t_2 - t_1} \cdot (t_0 - t_1) \quad (4.1)$$

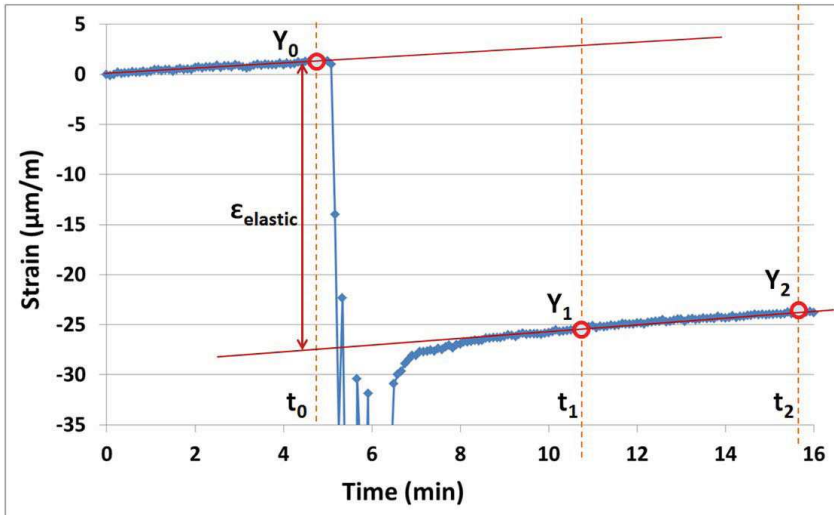


**Figure 4.15: Definition of the elastic relaxation occurring after drilling an increment.**

Figure 4.16 shows the application of this methodology to several successive drilled increments. High strain deformations measured while drilling were removed to simplify the representation of the results. It is remarkable that the strain rate is similar after drilling each increment. The first strain relaxation is a compressive one and the other increments go in the tensile direction. This confirms that the shape of the signal after drilling is not caused by initial residual stresses, but is due to both temperature fluctuations and recovering viscoelastic strains from the drilling process itself.



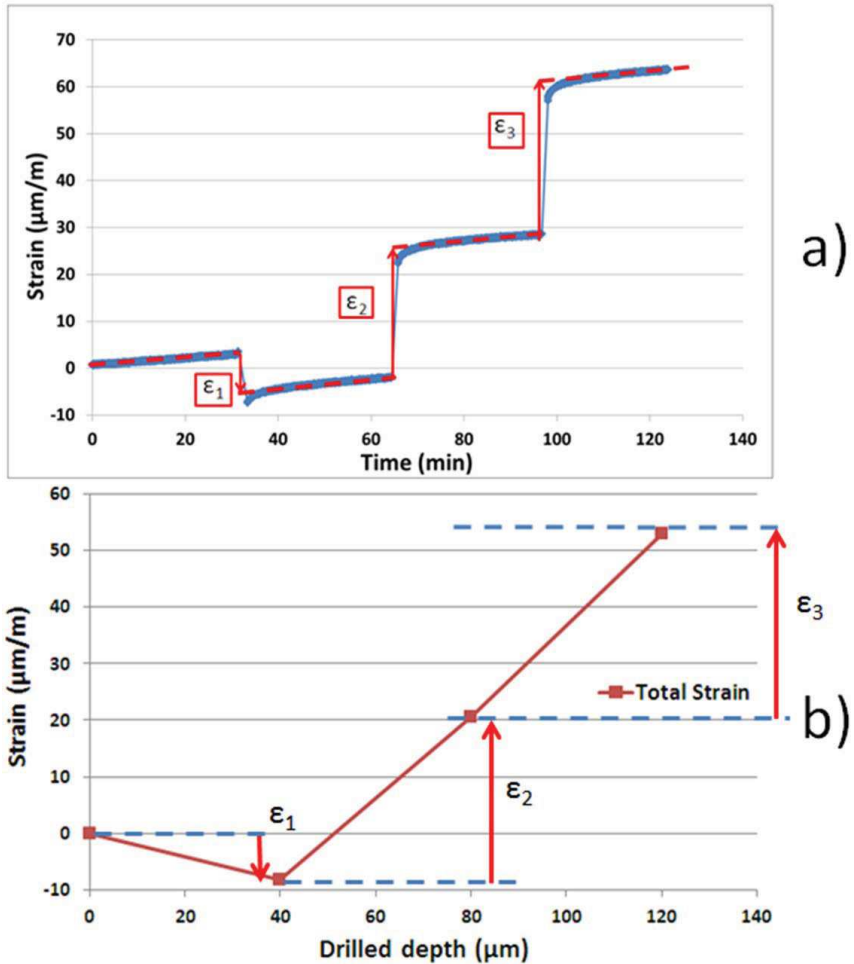


Figure 4.16: Practical solution to measure elastic strains during an experiment. Example of three consecutive increments. a) Measured total strain as a function of time. b) Released elastic strain of each drilling increment.

## 4.5 Conclusion

During a residual stress measurement in polymer materials with the hole drilling method, different effects influence the measurement. The experimental set-up has been adapted to polymer materials (chapter 4.2), e.g. polypropylene and polycarbonate, by avoiding cutter-induced heating, by selecting an appropriate cleaning agent for the surface preparation, and by utilizing an appropriate strain gauge bonding strategy. Improving the bonding of materials with a low surface energy by using a combination of a primer and UV light is recommended.

Different sources of errors that occur during an experiment have been analysed. Some errors are specific to the strain gauge technology. In fact, strain gauges cause a stiffening effect which lowers the strain field at the surface locally. This effect can be corrected by calibrating the strain gauge with a tensile test (chapter 4.3.4). Another source of error is the residual stress present in the strain gauge. The level of relieved strain is measured after drilling only the foil of the strain gauge rosette (chapter 4.3.3), which influences measurements and leads to a lack of accuracy near the surface.

Thermal expansion and viscoelastic strain during a measurement are also of great concern, because both effects are time-dependent and can influence measurements significantly. These time-dependent effects are also present if other technologies are used to measure strains or displacements, and they need to be corrected. A pragmatic evaluation procedure has been proposed to correct both effects and make measurements reproducible and reliable (chapter 4.4).

## **5 Application of the hole drilling method on polymer materials**

This chapter focuses on the application of the hole drilling method on polymer materials. Measurements were performed using the recommendations given in chapter 4. Three different materials were investigated: a polypropylene, a polycarbonate and a self-reinforced polypropylene composite PURE [Heim 2014]. Residual stress states in materials are influenced by varying the process parameters of injection moulding and by applying a laser transmission welding process. Then, the focus shifts to the analysis of the measured residual stresses in terms of plausibility and reproducibility (chapter 5.1). By quenching polycarbonate samples, it was possible to induce compressive residual stresses at the surface of the material. In doing so, the environmental stress cracking resistance of polycarbonate was able to be improved significantly (chapter 5.2). An experimental procedure was proposed to estimate the accuracy of measurements by bending each material (chapter 5.3). Finally, measurements in a hybrid structure made of a 1 mm thin sheet of aluminium and of another 1 mm layer of self-reinforced polypropylene were carried out on both sides of the structure (chapter 5.4).

### **5.1 Reproducibility of the measurement**

#### **5.1.1 Injection moulded polycarbonate**

##### **5.1.1.1 Methodological background**

First, how processing parameters influence the residual stress state in injection moulded polycarbonate samples was analysed. Five samples had been processed with dimensions of 155 mm x 60 mm x 4 mm while employing different process parameters (see table 5-1). Sample 1 was produced with unfavourable processing parameters that included a high injection rate of 1000 mm/s and a low mould temperature of 30 °C. High shearing and residual stresses occurred. Sample 2 corresponds to in-house recommended processing parameters, namely the injection rate was reduced to 100 mm/s and the mould temperature was increased to 80 °C. The higher mould temperature prevented fast cooling of the surface of samples, and, consequently, it should have reduced the residual stresses near the surface. Sample 3, which was processed with the same processing parameters as sample 2, was annealed to further reduce the residual stresses in the material.

A review by [Guevara-Morales 2014] about residual stresses in injection moulded samples provides plausible residual stress profiles. Residual stresses are influenced by the pressure history during the injection process. During the filling phase, the surfaces of samples freeze at lower pressure than the core, leading to tensile residual stresses near the surface. These are then followed by high compressive residual stresses which then converge to low tensile residual stress values in the core (see chapter 2.1.1.2). A

second effect that influences the residual stresses is the fast cooling of samples, leading to compressive residual stresses near the surface and tensile residual stresses in the core of the material (chapter 2.1.1.1). For example, in [Jansen 94], residual stresses in a 2 mm thick injected polystyrene strip were measured using the layer removal method. About 3.5 MPa tensile residual stresses were measured at the surface followed by compressive residual stresses of about -3 MPa 0.1 mm from the surface and then residual stresses reduced with tensile residual stresses in the core of about 1 MPa (figure 5.1). Therefore, such a tendency is expected for the following measurements of injected polycarbonate in samples 1 and 2.

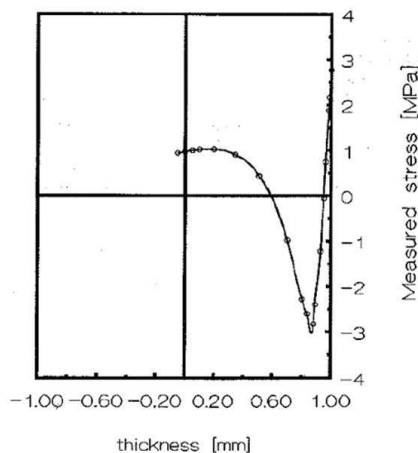


**Figure 5.1: Measured stress distribution (layer removal method) of an injection moulded polystyrene strip,  $E= 3400$  MPA and  $\nu=0.33$  [Jansen 94].**

Sample 4 was especially designed to see if the hole drilling method can qualitatively measure tensile residual stresses. In this case, the polycarbonate melt was injected into an aluminium frame (Figure 5.2.b). Due to the shape of the aluminium frame and owing to the fact that the thermal expansion coefficient of polycarbonate is higher than the one of aluminium, the shrinkage of the polycarbonate in the longitudinal direction X is constrained. For this reason, tensile residual stresses are expected at point A, which should be compensated by compressive residual stresses in the aluminium at point C to reach an equilibrium. The aim of this experiment is to measure the tensile residual stresses at point A.

The last example concerns sample 5, which was processed with a low mould temperature of 30 °C and a low injection rate of 100 mm/s to observe the influence of the injection rate with low mould temperature. The results can be compared with sample 2, which was processed with a higher injection rate of 1000 mm/s. All samples were measured in the middle, as can be seen in Figure 5.2.

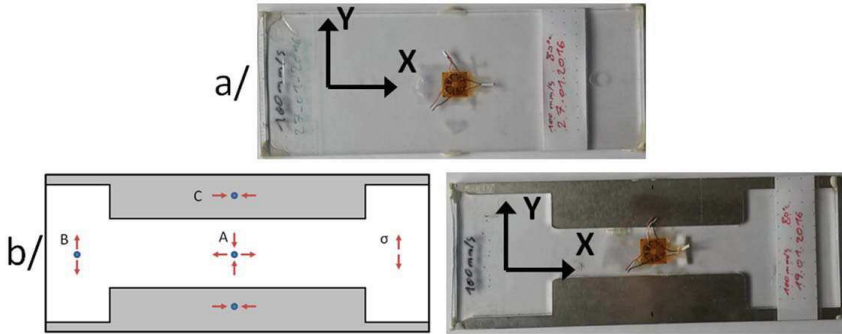


**Figure 5.2:** a/ Injected polycarbonate without an aluminium frame (samples 1, 2, 3, 5). b/ Polycarbonate sample injected into an aluminium frame (sample 4). Dimensions of samples are 155 mm x 60 mm x 4 mm. The red arrows highlight the expected orientation of the residual stresses. Residual stresses in samples were always measured in the middle as highlighted by the glued strain gauge.

**Table 5.1.1: Processing parameters for injection moulded polycarbonate**

|                        | Sample 1 | Sample 2 | Sample 3 | Sample 4                            | Sample 5 |
|------------------------|----------|----------|----------|-------------------------------------|----------|
| Injection Rate (mm/s)  | 1000     | 100      | 100      | 100                                 | 100      |
| Mould Temperature (°C) | 30       | 80       | 80       | 80                                  | 30       |
| Packing Pressure (MPa) | 50       | 50       | 50       | 50                                  | 50       |
| Melt Temperature (°C)  | 290      | 290      | 290      | 290                                 | 290      |
| Additional Information |          |          | Annealed | With aluminium frame (Figure 5.2.b) |          |

Different measurement strategies have been developed. To obtain accurate residual stress measurements near the surface, type EA-06-062RE-SE (Vishay Micro-Measurements) medium size strain gauges were used. A 2 mm diameter hole was drilled and residual stresses were evaluated with the hole drilling method up to 0.7 mm. Then, larger strain gauge rosettes of the type EA-06-125RE-SE were used to obtain information deeper in the material. In this case, a 4 mm diameter hole was drilled and information for a depth of up to 1.4 mm was obtained. In order to further increase the amount of obtainable data, the use of the ring core method was attempted. For this method, a ring slot was incrementally removed. The internal diameter of the circumferential slot was 14 mm and the external diameter was 17 mm.

Measured residual stresses near the surface should be interpreted carefully, because they are influenced by residual stresses in the foil of the strain gauge, as mentioned in chapter 4.3.3. Measurements with the hole drilling method using a 2 mm hole diameter are accurate from 0.1 mm to 0.7 mm (chapter 5.3.1). Chapter 5.1.1.2 shows the influence of processing parameters, and measurements of all samples are presented for each measuring method. Then, the influence of the injection rate in combination with a low mould temperature is shown (chapter 5.1.1.3). Lastly, in order to analyse the reproducibility of measurements, chapter 5.1.1.4 shows the results classified for each processing parameter, and illustrates where the differences between each measuring strategies lie (hole drilling method with 2 mm and 4 mm diameter holes and ring core method).

### 5.1.1.2 Influence of process parameters

In Figure 5.3, residual stresses and relieved strains are shown in the longitudinal direction X of samples. Each graph shows results obtained for samples 1 to 4 while applying different methods: the hole drilling method with a 2 mm diameter hole (a and b) and a 4 mm diameter hole (c and d), the ring core method with a ring slot (e and f). Sample 5 was depicted separately in Figure 5.4 to simplify the visualization and comprehension of results. In Figures 5.3.b and 5.3.d, it is evident that samples processed without an aluminium frame have low residual stresses near the surface within 0 MPa and 1.5 MPa, then compressive residual stresses appear with a maximum absolute value near a depth of about 0.3 mm. Farther away from the surface, the residual stresses reduce and turn into tensile stresses at about 0.8 mm. Tensile stresses are approximately constant at a depth of 1 mm and deeper. This profile is similar to the one reported in literature (Figure 5.1). Results in the transverse direction Y (not shown here) have the same tendency in samples 1, 2 and 3, but maximum compressive residual stresses are a little different. The influence of the processing parameters is readily visible. Annealed sample 3 presents the lowest residual stress values with a maximum compressive residual stresses of about -1.6 MPa in the X direction (and -1.7 MPa in the Y direction). Sample 2, processed with the same recommended parameters but without the annealing step, has higher maximum compressive residual stresses of about -3.2 MPa in the X direction and -3.1 MPa in the Y direction. Sample 1 was processed with a higher injection rate and a lower mould temperature, and even has higher compressive residual stresses of about -3.7 MPa in the X direction and -4.6 MPa in the Y direction, which may be due to faster cooling of the material. As expected, sample 4 that was injected into an aluminium frame displayed residual stresses in the longitudinal direction X of the sample, which are tensile residual stresses. The profile of the residual stress state is similar to the other samples, the lowest value 0.8 MPa is again at a depth of about 0.3-0.4 mm. In comparison to sample 2 that was produced with the same processing parameters, but without aluminium frame, the residual stress profile of sample 4 shifted in the tensile direction by about +4.3 MPa. In graph 5.3.d, results with a hole diameter of 4 mm are

complementary and show that tensile residual stresses are approximately constant in depth.

A better comparison between each measuring method and the existing differences can be seen in the following chapter 5.1.1.4. Results obtained with the ring core method in graph (f) show a lack of accuracy. Strains measured in the first 0.8 mm (graph e) are really low, meaning that this method is not suitable for near surface measurements as it is less sensitive than the hole drilling method. If one goes deeper than 2 mm (graph f), the compressive residual stresses increase, which is not plausible because the symmetry of residual stress is expected for this sample. At the same depth of 2 mm in graph (e), a strain error was measured for the sample injected in an aluminium frame. This error probably indicates that the drilling process damaged the material.

### **5.1.1.3 Influence of injection rate by low temperature**

A comparison between residual stresses measured in samples 1 and 5 with the hole drilling method can be seen in Figure 5.4. Sample 5 exhibits higher tensile residual stresses near the surface, which cannot be an error because tensile residual stresses exist up to 0.35 mm. The residual stress profiles measured for both samples are similar; both become compressive deep within the material, though the location of the maximum compressive residual stress differs. Then, residual stresses reduce and converge to almost zero. Thus, reducing the injection rate leads to higher tensile residual stresses which remain deeper in the material. A possible explanation for this phenomenon is the consideration of pressure-induced residual stresses during the injection process. In chapter 2.1.1.2, a model is presented which shows that the polymer flow freezes at different pressures during the injection moulding process. In the cases of samples 1 and 5, reducing the injection rate may have increased the volume near the surface, which solidified at low pressure. Therefore, tensile residual stresses are no longer located directly at the surface, but are homogenised deeper in the material.

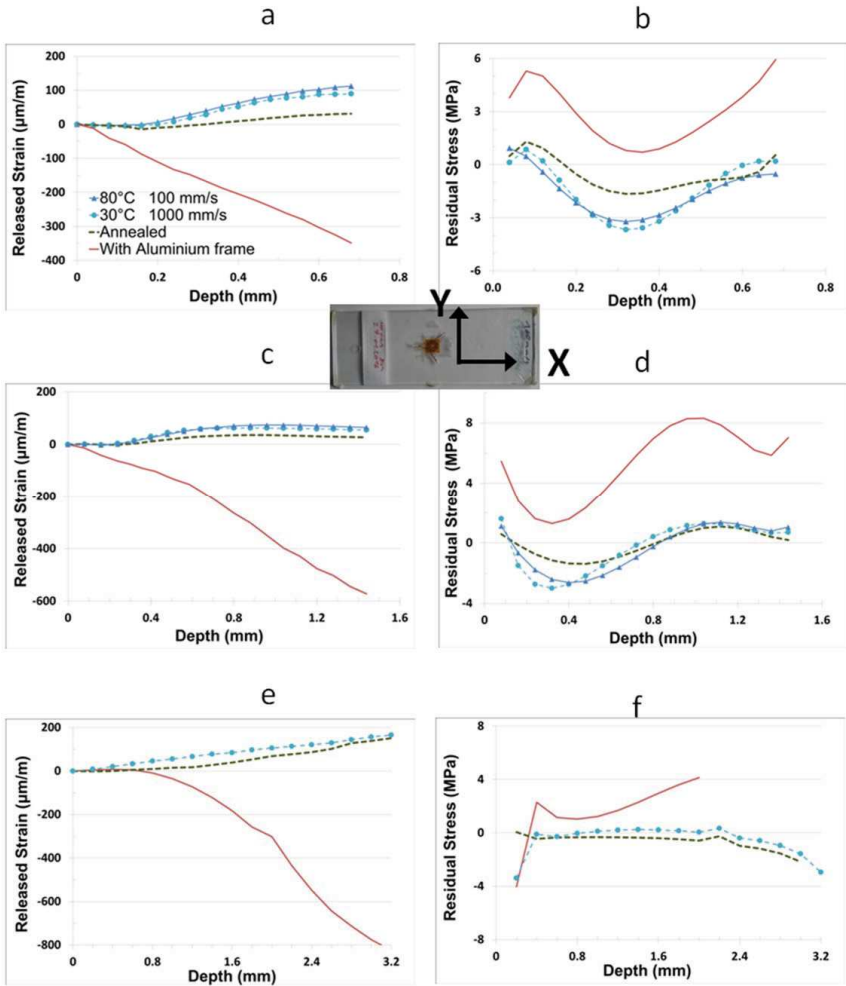
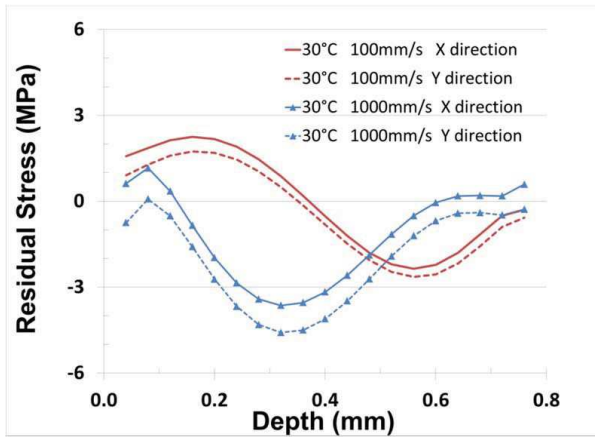


Figure 5.3: Relieved strain and measured residual stress in the direction X when applying the hole drilling method with a 2 mm hole (a and b), a 4 mm hole (c and d) and when applying the ring-core method (e and f).





**Figure 5.4:** Residual stress measurement in two injection moulded polycarbonates with a mould temperature of 30°C and injection rates of 100 mm/s and 1000 mm/s respectively.

#### 5.1.1.4 Reproducibility of results

Figure 5.5 depicts a comparison between the different measurement strategies for the following samples: sample 4 moulded in an aluminium frame (5.5.a-b), sample 1 processed with a high injection rate and low mould temperature (5.5.c-d), and post-moulding annealed sample 3 (5.5.e-f). Both residual stresses in the longitudinal X (continuous line) and transverse direction Y (dotted line) are represented for each measuring method. In Figure 5.5.a-c-e, one can see that the relieved strain is higher at the same depth when applying the hole drilling method with a 2 mm diameter hole. Consequently, better accuracy is expected for measurements with a hole diameter of 2 mm with the exception of results in the first 0.1 mm, which are influenced by stresses in the strain gauges (chapter 4.3.3). Furthermore, since the relieved strains for the ring core method are small near the surface, the method is not recommended for analysis of residual stresses near the surface. In Figure 5.5.b-d-f, a good relation is observed between results measured with the hole drilling method with different strain gauge sizes - the results are reproducible. However, measurements performed using the ring core method are not satisfying, because they are not comparable to the two other measuring methods. In Figure 5.5.d, note that both residual stresses in the longitudinal direction X and transverse direction Y are close together; the residual stresses are quasi equibiaxial. The difference between both residual stresses may be due to the high injection rate used to process the sample (Figure 5.5.d). This difference was measured for both measurements with 2 mm and 4 mm hole diameters. For sample 3 annealed after moulding, the measured strains (graph e) and calculated residual stresses (graph f) were, as expected, the lowest. Maximum compressive residual stresses of -1.7 MPa (hole diameter 2 mm) and -1.4 MPa (hole diameter 4 mm) were measured. Almost no difference in the residual stresses was measured in both directions X and Y for the

post-moulding annealed samples. The hole drilling measurements with different hole diameters deliver really close results for each processing parameter.

In conclusion the results of these first experiments are really promising. The hole drilling method was used with two different hole diameters. That way, it was possible to measure residual stresses at different depths and to adjust the level of accuracy as higher strains were measured with smaller strain gauges. Results from the hole drilling method are reproducible if holes of different sizes are drilled. Also, the measured profiles are plausible and have been reported elsewhere (Figure 5.1). However, such results had never been measured with the hole drilling method before. As such, measurements with the hole drilling method can be performed on polycarbonate samples using the recommendations provided in chapter 4, and they are qualitatively validated. Measurements with the ring-core method did not provide a satisfying result. The ring nut probably damaged the material and this method is not adapted for measurements close to the surface, because the relieved strains are smaller than strains measured with the hole drilling method.

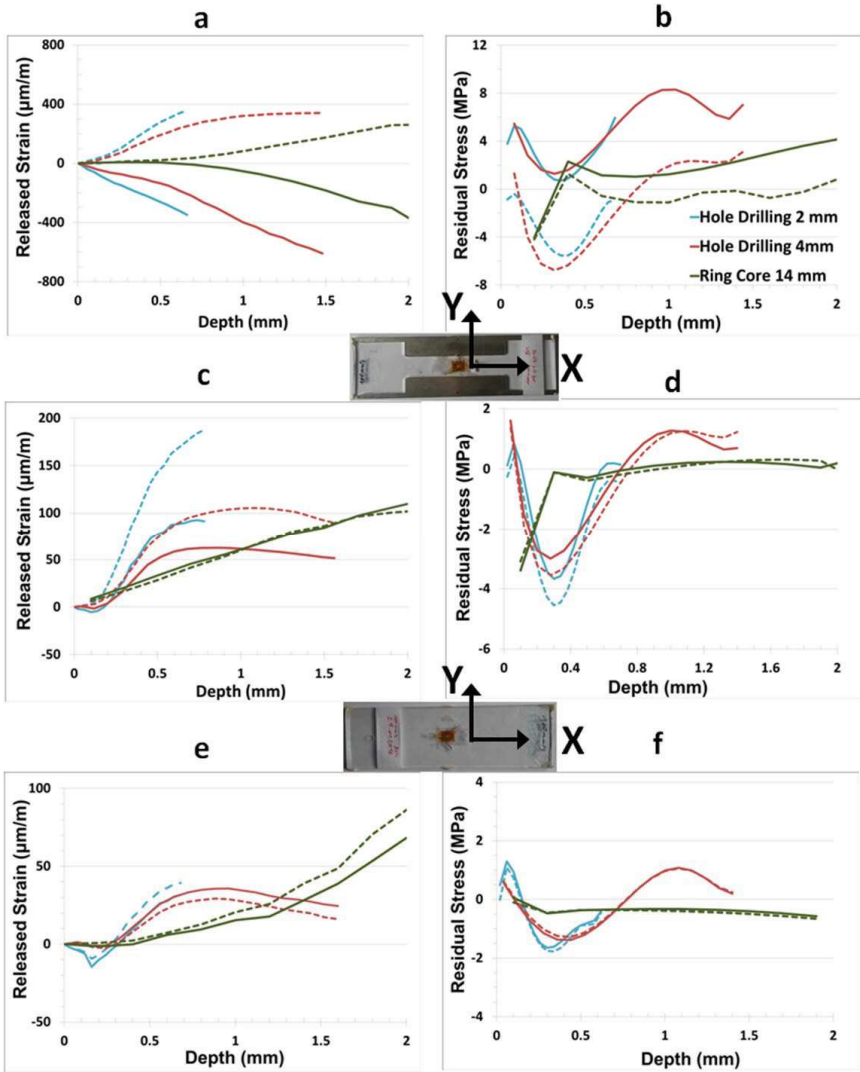


Figure 5.5: Measured strains and calculated residual stresses in the longitudinal direction X (continuous line) and transverse direction Y (dotted line) in polycarbonate samples: sample 4 was moulded into an aluminium frame (a and b); sample 1 was produced with a mould temperature of  $30^{\circ}\text{C}$  and injection rate of  $1000\text{ mm/s}$  (c and d); post-moulding annealed sample 3 (e and f).

### 5.1.2 Transmission laser welded polypropylene structure

The aim of this study was to develop a methodology to measure residual stresses in transmission laser welded polypropylene components, which was a

challenge due to the special geometry of the joined components and the lack of knowledge about measurements of residual stresses in polypropylene. During the transmission laser welding process, two components are joined (Figure 5.6). To absorb the energy from the laser, one component is composed of polypropylene with carbon black content. That way the laser penetrates through the first transparent polypropylene joining part during the process and the energy of the laser is mostly absorbed by the second joining black part. The energy of the laser is locally converted into heat and it mainly melts the polypropylene with carbon black content. In Figure 5.6, the weld seam is represented by the red rectangular surface. After the locally heated area cools, the material shrinks (red arrows). As the cooling of the material is constrained by the surrounding material, residual stresses develop in all directions. Figure 5.7 schematically shows residual stresses developing in a thin metal sheet after a single-pass welding process.

An analogy exists between the laser transmission welding process and the model shown in Figure 5.7. Due to the restricted cooling of the weld seam, the maximum tensile residual stresses in the longitudinal direction Y develop in the middle of weld seam. These residual stresses are equalised by compressive residual stresses along the plate width (red curve). In the case of laser transmission welded components, the shrinkage of the weld seam is not only restricted by the material on the side (direction X as shown in Figure 5.7), but also by the material at the bottom and top (Z direction). Therefore, it can be assumed that residual stresses in the longitudinal direction Y have a similar profile near the weld seam along the X and Z directions. Thus, applying the hole drilling method, was expected to result in the measurement of a similar in-depth profile as the red curve in Figure 5.7.

Furthermore, residual stresses near the surface of components are more likely induced by the injection moulded process (see chapter 5.1.1). In [Kreimeier 2016], residual stresses were simulated in transmission laser welded components made of polyamide 66. The highest tensile residual stresses were located in the weld seam with a maximum of 80 MPa in the longitudinal direction Y of the weld seam and 20 MPa in the normal direction Z (see coordinate system in Figure 5.6). Residual stresses in the normal direction Z were not measurable using the hole drilling method, and it is wrong to assume that these residual stresses do not exist. The influence of residual stresses in the normal direction Z on the measurement was neglected. Therefore, measurement proved to be a challenge because the weld seam is located deep within the material and the standard requirements for utilizing the hole drilling method were not fulfilled.

Each joint material was 2 mm thick, and a 4 mm diameter hole was drilled to obtain information as deep in the material as possible. Strains measured with strain gauge rosettes were converted into residual stresses with the method proposed in chapter

2.3.4. The standard method (chapter 2.3.2) may not be applicable because the sample is thin and a notch is present (joint) in the area of interest, which should influence the relations between the residual stresses and strains (chapter 2.3.4). Hence, the reproducibility and feasibility of measurements have to be analysed.

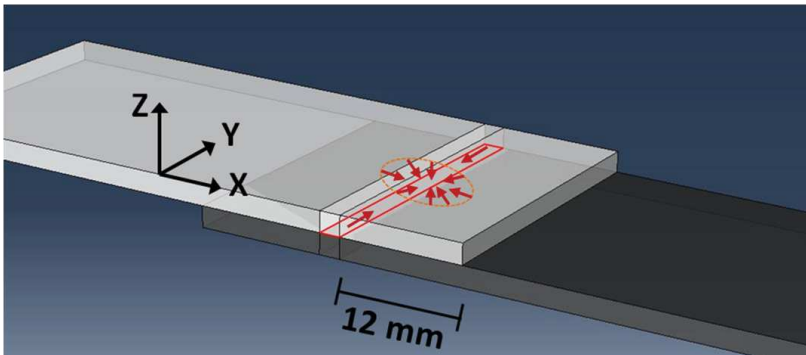


Figure 5.6: Two components joined with laser transmission welding. The weld seam is represented by a red rectangle. Arrows symbolize the direction of thermal strain caused by cooling after the welding process.

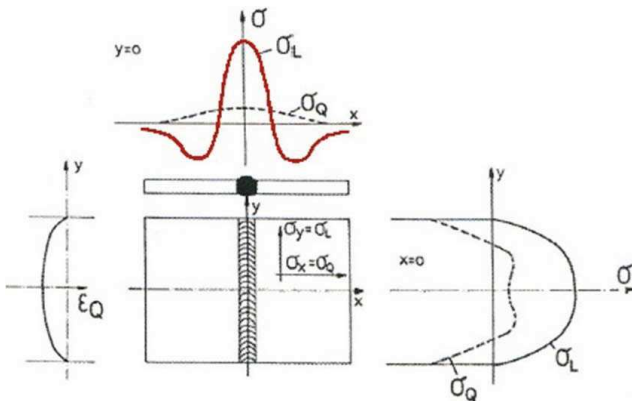


Figure 5.7: Longitudinal and transverse residual stresses along line Y parallel to the weld seam and along line X perpendicular to the weld seam. The model is applicable for a single-pass welding process of a sufficiently thin sheet [Macherauch 1977].

Different parameters were utilized to analyse their respective influences on residual stress formation. The carbon black content in one of the polypropylene components was varied from 0.1 % to 0.2 %, and then the power of the laser was set to 2.5 W, 3.25 W or 5 W. The feed rate of the laser was kept at a constant rate of 1.25 mm/s. The measurement matrix was resumed in Table 5-2. Chapter 5.1.2.1 demonstrates how the selection of the calculation model influences the results. In chapter 5.1.2.3, the carbon

black content and laser power were varied to investigate their influence on the residual stresses in the black joint part. Finally, evidence that higher tensile residual stresses are located in the black joint part was obtained, making measurements in the transparent part unnecessary.

**Table 5.1.2: Overview of samples processed with laser transmission welding**

|                           | Laser power 2.5 W | Laser power 3.25 W | Laser power 5 W | Original state (not joined) |
|---------------------------|-------------------|--------------------|-----------------|-----------------------------|
| Carbon black content 0.1% | -                 | X                  | X               | X                           |
| Carbon black content 0.2% | X                 | -                  | X               | X                           |

### 5.1.2.1 Influence of the sample geometry on calculated residual stresses

In order to measure residual stresses in the middle of the weld seam, it is necessary to use special calibration coefficients to calculate residual stresses due to the geometry of the joined samples. Different strategies exist to calculate residual stresses depending on how the geometry of the sample is implemented in the finite element model. In Figure 5.8, three models are shown where the red surfaces highlight the weld seam. If the real geometry is considered (Figure 5.8.a), it is then necessary to use the formalism from chapter 2.3.4 to obtain calibration coefficients, because of the presence of the joint which behaves like a notch (chapter 2.3.4). This model is the closest solution to reality and should provide more accurate results. In Figure 5.8.b, the geometry of the sample is simplified. We assumed that the joint was wide and provided enough stiffness, as if both 2 mm components were perfectly joined over their entire surface. Therefore, the sample was modelled like it was a 4 mm thick material without a joint. Figure 5.8.c represents the opposite case, where the joint was considered to be too thin to influence measurements, as if both components were not joined. Only one of the two 2 mm component was modelled in this third case. The model closest to reality (figure 5.8.a) should provide the best results, but it is interesting to see to which extent the results are influenced by the choice of model. Thus, it is possible to evaluate the necessity to invest time and effort into calculating calibration coefficients specific to the geometry of the sample.

In Figure 5.9, residual stresses can be seen in the black part of a laser welded component, and were evaluated using the assumption mentioned above. The sample was drilled above the weld seam (Figure 5.8.a). None of the three models can measure accurately near the joint at a depth of 2 mm. If the sample is assumed to be 2 mm thick, a high error margin can be noticed at a depth of about 1.4 mm. The results from other models are also sensitive when performing in-depth measurements, however, they are evaluable up to a distance from the surface of about 1.6 mm.

The geometry-specific model seemed to be more suitable than the 4 mm thick model, because the tensile residual stress reduction was less pronounced near the joint. This tensile residual stress reduction was not expected and illustrates the inability of the 4 mm thick model to measure at such a depth. Residual stresses near the surface displayed similar behaviour as the injected moulded polycarbonate measured in chapter 5.1.1 (Figure 5.5), with maximum compressive residual stresses at a depth of about 0.3 mm. However, in this case, the tensile residual stresses deep within the material were higher in absolute value than the compressive residual stresses near the surface. This confirms that the laser transmission welding process induces tensile residual stresses near the joint. A comparison with residual stress measured in non-welded samples will be shown in chapter 5.1.2.2. Furthermore, in the transverse direction X of the joint near the surface, residual stresses calculated with the geometry-specific model are included between the values obtained with the model with 4 mm thickness and the other one with 2 mm thickness. This behaviour was expected because the joint implements a little stiffness in the material, which resists deformation in the X direction. Considering this resistance to deformation in the transverse direction X, the geometry-specific model with its thin joint is in between the two other models, where the joint spans the entire surface (4 mm model) or does not exist (2 mm model).

The reasons the geometry-specific model and the 4 mm model show the same trend near the surface in the Y direction are similar (Figure 5.9, right). The joint is located along the whole width of the sample and strongly contributes to the resistance against deformation in the Y direction. This resistance to deformation is the same as in the case of a 4 mm thick material. In contrast, a 2 mm thick sample has different deformation behaviour, and, consequently, the residual stresses near the surface are lower for this model.

In conclusion, the model used with the specific geometry seems to be applicable, and results should be considered with care near the joint. If a qualitative investigation of influencing parameters is expected, it should be enough to consider the model as being a 4 mm thick continuum (no weld seam). With other words, it is safe to assume that both joint partners are perfectly bonded along their whole surface. Therefore, the geometry-specific model is not necessary. Owing to the fact that the geometry-specific model has already been calculated for this study, it will be used in the next chapter for the evaluation of influencing parameters to provide more accurate measurements and to limit the residual stress drop deep in the material to 1.6 mm.

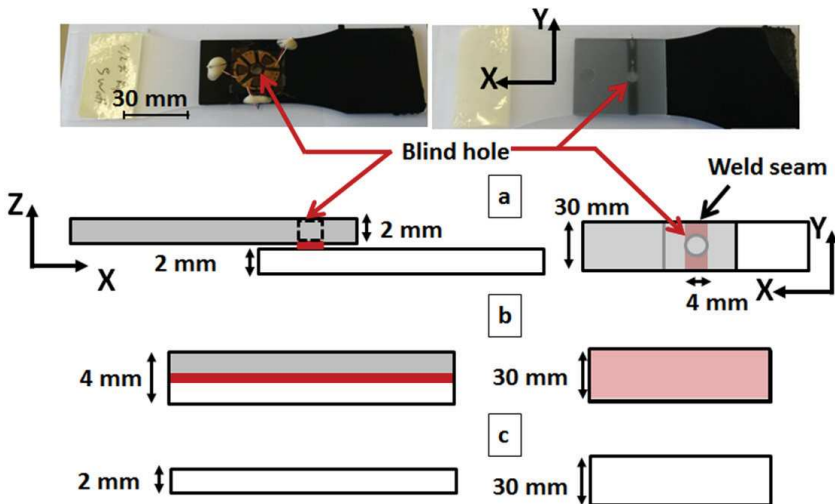


Figure 5.8: Geometries of two components joined with laser transmission welding used in finite element analysis. The red surface shows how the weld seam is considered in the simulation. In model (a), the two components and the weld joint were modelled with real sample geometries. Both components are perfectly joined along the thin weld joint. In (b), the two joint parts are joined along their whole surface. Model (b) is the same as a 4 mm thick single component. In (c), the weld joint is neglected; only one joint part was modelled with a thickness of 2 mm.

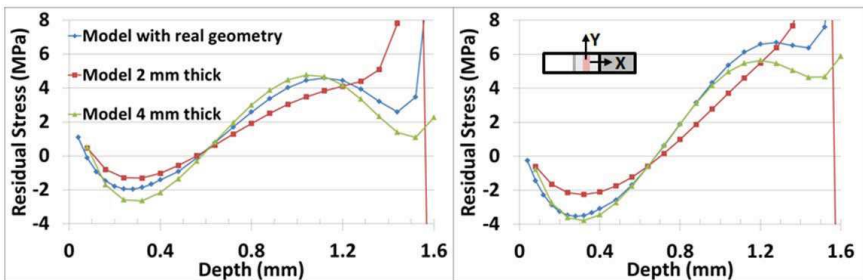


Figure 5.9: Residual stresses in the black part of a laser welded component. Left: Residual stresses in the transverse direction X of the joint. Right: residual stresses in the longitudinal direction Y of the joint. Three models have been used to show the influence of the geometry of the samples (see Figure 5.8)

### 5.1.2.2 Residual stress in laser transmission welded samples

In the previous chapter, a strategy was defined to measure residual stresses in transmission welded samples and to analyse which parameters influence their formation. Two parameters were investigated: the carbon black content in the black joint part and the laser power. Investigated samples have been resumed in Table 5.2,



only the black joint parts were measured. It is shown in chapter 5.1.2.3 that residual stresses are higher in this section (Chapter 5.1.2.3).

In Figures 5.10 and 5.11, the influence of the laser power is revealed in the black joint part with respectively 0.1 % and 0.2 % carbon black content. In Figure 5.10, the initial residual stress state of the material (original state) is characterized by low compressive residual stresses of about -1.5 MPa. Values located directly at the surface before 0.2 mm are not reliable due to residual stresses in the strain gauge (chapter 4.3.3). The core of the material is in a tensile stress state with residual stresses of about 2 MPa at a depth of 0.9 mm in both directions X (left) and Y (right). Symmetry of the residual stresses may be assumed as the samples were first processed using injection moulding. If the two joint parts are joined with a laser power of 3.25 W or 5 W and a carbon black content of 0.1 %, low compressive residual stresses of about -2.5 MPa are present near the surface at a depth of about 0.2 mm. Then residual stresses turn into tensile stresses with a value of about 4.5 MPa (3.25 W) and 6 MPa (5 W) at a depth of about 1.2 mm in the transverse direction X of the joint. Deeper in the material, the tensile residual stresses reduce, which does not seem plausible as more tensile residual stresses are expected near the joint. Eventually, the measured residual stresses may be less than real residual stresses if the hole diameter is larger than the width of the weld seam, and the measurement, thus, represents an average.

In the longitudinal direction Y of the joint, a similar profile can be measured, the maximum residual stress increases to 7.2 MPa at a depth of 1.36 mm (3.25 W). In the cases of all different applied laser powers, tensile residual stresses were always higher in the longitudinal direction Y than in the transverse direction X. Applying a stronger laser power of 5 W resulted in higher tensile residual stresses of up to 9.6 MPa in the longitudinal direction Y. Similar results were observed if the carbon black content was increased to 0.2 % (figure 5.9). The maximum induced tensile stress was around 8.8 MPa at a depth of 1.44 mm with a laser power of 5 W.

A sample joined with a laser power of 2.5 W shows a similar trend with lower maximum tensile residual stresses of about 3.5 MPa. However, this sample showed really weak adhesion. The transparent partner probably did not melt during the laser transmission process. This could explain why the maximum tensile stresses were lower for a higher laser power. Since the adhesion between both parts was weak, and one of the samples was separated during manipulation, it was then possible to measure residual stresses directly at the weld seam of the black partner (Figure 5.12 and Figure 5.13 blue curve). In Figure 5.13, sample 1, which had a full bond between the joint partners, was processed with a laser power of 2.5 W, and was measured from the surface (depth 0 mm in figure 5.12, joint is at a depth of 2 mm). The other sample 2, which showed no adhesion (both joint partners were not joined but had undergone an identical time-temperature profile), was measured directly at the joint (depth 2 mm in

Figure 5.13). The residual stresses measured at the surface were inaccurate in both measurements (depth 0 mm and 2 mm) due to residual stresses in the strain gauge. Both measurements seem complementary, a residual stress plateau is visible for the residual stresses in the transverse direction X of the joint with a maximum tensile stress of about 2 MPa. Residual stresses in the longitudinal direction of the joint revealed the expected profile with tensile residual stresses increasing up to 6 MPa. Differences between both measurements can be seen at a depth of about 1.2 mm. These differences may be due to the method being oversensitive to strain errors in the depth of the material.

In conclusion, measurements performed on transmission laser welded components provided sufficient information about the residual stress state near the joint. How the laser power directly influences the residual stress state near the joint was illustrated and high tensile residual stresses up to 9 MPa were revealed to be present in the black joint partner if a high laser power is applied. The effect of the carbon black content showed no clear influence. Measuring residual stresses at the joint of samples without transparent partner provided a complementary understanding of residual stress formation.

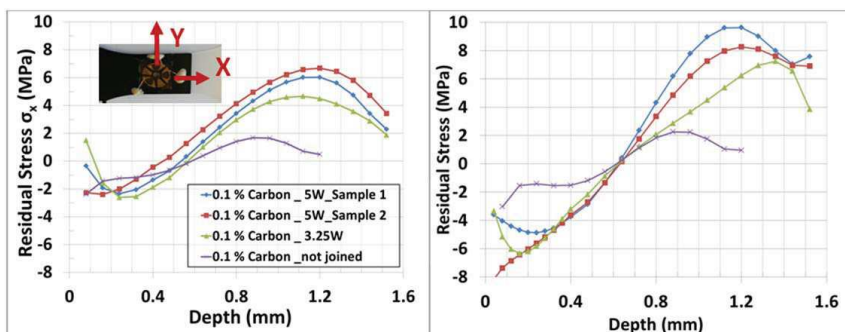


**Figure 5.10: Residual stresses in the black joint part of polypropylene components with 0.1% carbon black content. Samples were joined with transmission laser welding while varying the laser power. One sample was not joined for the sake of comparison. Left: residual stresses in the transverse direction X of the joint. Right: Residual stresses in the longitudinal direction Y along the joint.**

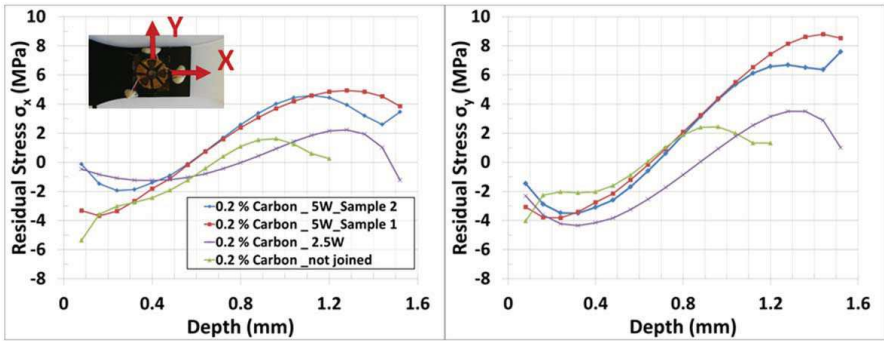


Figure 5.11: Residual stresses in the black joint partner of polypropylene components with 0.2 % carbon black content, joined with laser transmission welding while varying the laser power. One sample was not joined for comparison. Left: residual stresses in the transverse direction X of the joint. Right: Residual stress in the longitudinal Y along the joint.

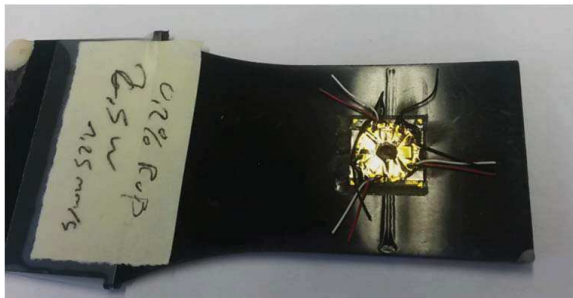


Figure 5.12: Welded sample separated from the other joint partner due to inappropriate welding process parameters. The laser power was 2.5 W for a feed rate of 1.25 mm/s.

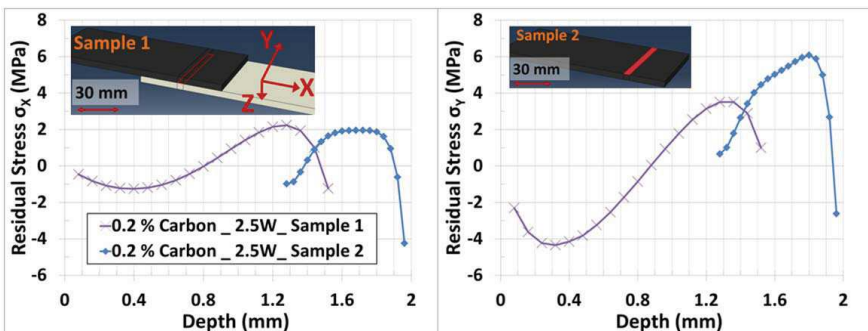


Figure 5.13: Residual stresses measured in components with 0.2% carbon content. Sample 2 showed no adhesion during transmission laser welding and became separated from its transparent partner. This sample was measured directly at the middle of the

joint (Figure 5.12). The surface of sample 2 is 2 mm deep in the material. Sample 1 is composed of two joint partners and the measurement was carried out in the middle of the surface of the black component, above the joint. The surface of sample 1 corresponds to the depth 0 mm. The joint of the samples was emphasized by the red rectangles. Left: Measurement of residual stresses in the direction X transverse to the joint. Right: Measurement of residual stresses in the direction Y longitudinal to the joint.

### 5.1.2.3 Comparison of residual stresses in the transparent and black joint parts

In order to obtain information about critical residual stress states near the joint, two samples were measured on two different sides. In Figure 5.14, near the joint, tensile residual stresses were observed in the black part (right side, depth 2.6 mm) and compressive residual stresses in the transparent part (left side, depth 1.5 mm). This seems plausible as most energy is converted into heat in the black part. That way, the influenced area with tensile residual stresses is by far wider in the black part than in the transparent part. Results cannot be evaluated deeper than 1.6 mm from the surface, because the measurements become too sensitive to errors. Therefore, it is not possible to analyse the continuity of residual stresses near the joint between the two joint partners. Since high tensile residual stresses are measurable in the black part, only this side seems relevant and it is not necessary to measure residual stresses in the transparent part.

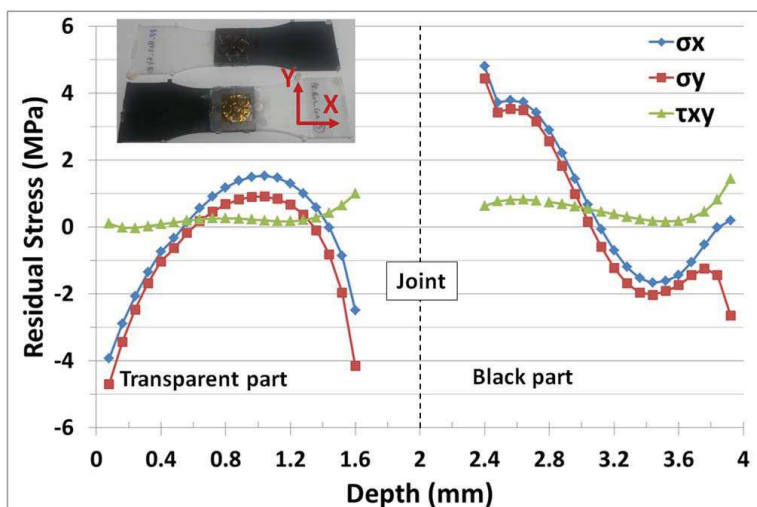
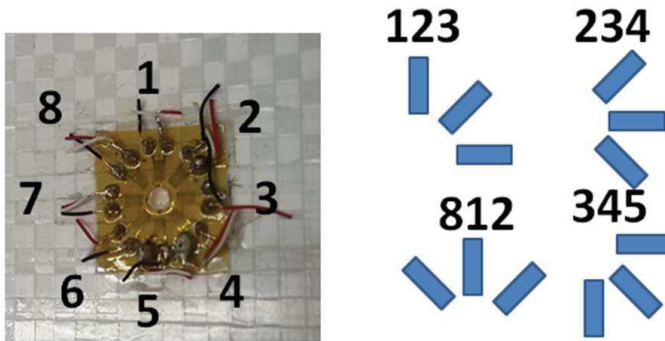


Figure 5.14: Residual stress measurements in the transparent and black parts of two laser transmission welded samples. Two welded samples have been measured, each on only one side. Samples were joined with a laser feed rate of 20 mm/s and a laser power of 7.9 W.

### 5.1.3 Reinforced polypropylene

Measurements were performed on the self-reinforced polypropylene composite PURE (Figures 5.15-16). A 500 mm x 500 mm x 4 mm sheet was processed. This sheet was composed of 32 semi-finished fabrics which have a high degree of self-reinforcement [HEIM 2011, 2014]. Those fabrics were sealed together in a laboratory press (Joos LAP 800) with a pressure of 3 MPa at a temperature of about 160 °C and with a holding time of 180 s. Then the formed sheet was cooled down to 50 °C in 500 s in the press at a constant pressure (3 MPa). 140 mm x 25 mm x 4 mm samples were milled from the plate.



**Figure 5.15: Left: Eight grid strain gauges glued on a self-reinforced polypropylene composite. Right: Example of different possible gauge combinations to calculate residual stresses.**

To ensure plausibility of the results, a strain gauge with eight grids was used (Figure 5.15). Only three non-parallel strain gauges are required to calculate residual stresses and they can be chosen arbitrarily. Based on the measured data, eight configurations were chosen (123, 234, 345...) to evaluate residual stresses and to investigate the possible influences of anisotropy and material defects (voids). This strain gauge also enables the accuracy of the strain analysis to be evaluated since two different parallel strain gauge grids should measure the same relieved strain. Furthermore, influences on the scattering of residual stresses evaluated with all eight configurations can be directly observed. A hole diameter of 2 mm was drilled, which has similar dimension as the PURE tape width (2.2 mm). Mesoscopic residual stresses may exist at the interlacement of warp and weft yarns. These residual stresses are self-compensated between several meshes, but can still influence the result because the hole diameter is small. With the hole drilling method, it is expected to measure cooling thermal stresses due to the fast cooling of the material in the press. Owing to the fact that the directions of the reinforcements of each fabric were aligned together, no discontinuity was expected when drilling the different fabrics. Discontinuous thermal residual stresses would have been induced if the whole structure was composed of differently oriented

fabrics (Figure 2.4). Residual stresses induced by the pressure of the press were not expected, because the material was heated and cooled down at a constant pressure.

In Figure 5.16, the measured eight strain signals are shown. Strain gauges 1,3,5,7 are particularly interesting due to the fact that they are oriented in the direction of the reinforcement of the material, which should be the directions of the principal residual stresses. In Figure 5.16, one can see that strain gauges 1 and 5 did not measure the same strains, which is also the case for strain gauges 3 and 7. This difference occurred due to the structure of the self-reinforced polypropylene; the strain gauges have the same dimensions as the woven structure, which is not recommendable. Strain gauges are localized at the crossing of yarns which acts as a stress raiser, influencing the measured strain (chapter 4.3.4 and Figure 5.15). Since the whole structure was composed of 32 plies and the crossing points of the tapes of each ply were not aligned amongst each other, local strain errors, which are not predictable, were induced during the experiments. The drilling process could have also damaged the material, resulting in a localized strain increase. In conclusion, irregularities exist in the measured strains, and, thus, residual stress measurements should be interpreted carefully.

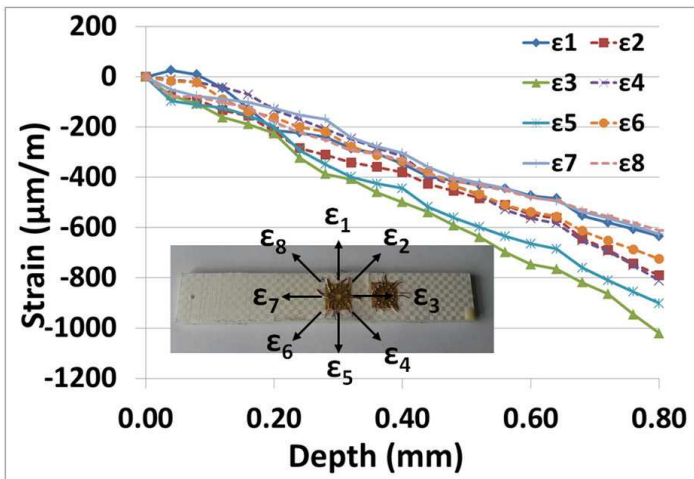


**Figure 5.16: Strain measured in eight directions with an eight grid strain gauge in a self-reinforced polypropylene composite after drilling incrementally the sample.**

Eight combinations of three strain gauges were chosen to evaluate the residual stresses. Two models were used to calculate residual stresses. The first model considers the material to be isotropic ( $E = 5.5$  GPa,  $\nu = 0.1$ ). In the second model, orthotropic elastic constants of the material were assumed (Table 3-1) and residual stresses were evaluated using the formalism of the integral hole drilling method for orthotropic material (chapter 3.2). The results are shown in Figure 5.17 with both

models and all strain gauge configurations used. Since residual stresses calculated with all strain gauge combinations are highly scattered, only the average value was interpreted. Scattering in strain measurements may be due to material damages or due to the woven structure which locally acts as a strain raiser. Data obtained for the first 0.1 mm is not evaluable due to residual stresses in the strain gauge (chapter 4.3.3). The residual stress average near the surface remained mostly constant up to 0.5 mm and then diverged. Measurements deep in material may be influenced by increasing material degradation and, hence, are not reliable. When using the orthotropic formalism, the minimum principal residual stress is about 5 MPa (Figure 5.17.a) and the maximum residual stress about 10 MPa (Figure 5.17.b). In different strain gauge combinations, residual stresses are in a range of approximately  $\pm 5$  MPa. If the wrong model (isotropic) is used, the residual stress state has a similar profile, but residual stresses are overestimated with a minimum residual stress of about 20 MPa (Figure 5.17.c) and a maximum residual stress of about 30 MPa (Figure 5.17.d).

In conclusion, the use of eight strain gauges is necessary due to a high level of scattering of measurement data. The accuracy of measurements is questionable, because parallel strain gauge grids did not measure the same strains. Scattering may be due to the special woven structure of the material, and, additionally, the drilling process may increase damage already present in the material. Still, a residual stress state calculated with different strain gauge configurations seems to produce tensile residual stress values ranging between 5 MPa and 10 MPa which are oriented in the reinforcement direction. This holds true if the orthotropic material properties of a material are taken into consideration. Residual stresses were overestimated by a factor of four for the minimum residual stresses and by a factor two for maximum residual stresses when using the isotropic formalism. A quantitative validation procedure is necessary to validate the accuracy of measurements in such a material (chapter 5.3.4).

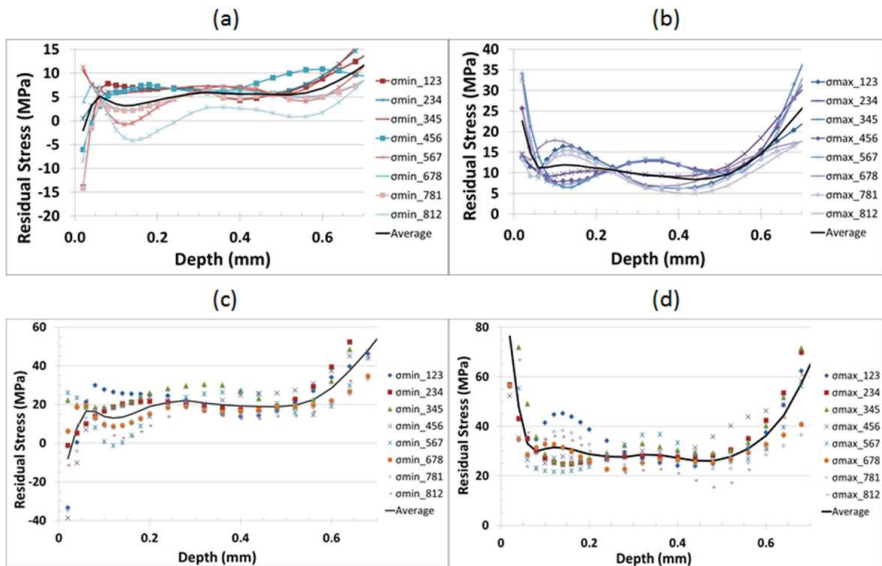


Figure 5.17: Both principal residual stresses  $\sigma_{max}$  and  $\sigma_{min}$  were measured for a self-reinforced polypropylene composite. The sample was either considered isotropic (c and d) or orthotropic (a and b). Eight combinations of three strain gauges taken from an eight grid strain gauge were used to evaluate residual stresses (Figure 5.15).

## 5.2 Free quenching

Compressive residual stresses have the potential to improve material properties such as the endurance limit [Hornberger 1987], or environmental stress cracking (chapter 5.3.2). Quenching of previously heated samples is a well-known procedure to induce typical parabolic residual stress states in a material with compressive residual stresses at the surface and tensile residual stresses in the core (chapter 2.1.1.1, Figure 2.2). Polypropylene (chapter 5.2.2) and polycarbonate (chapter 5.2.1) samples were annealed and successively quenched in water. In doing so, samples with compressive residual stresses near the surface were created for hole drilling tests.

### 5.2.1 Polycarbonate

Two 160 mm x 60 mm x 4 mm polycarbonate samples were annealed and quenched. Sample 1 was annealed at 150 °C and quenched in 17 °C water. The process was similar for sample 2 and the annealing temperature was 147 °C followed by quenching in about 20 °C water. The temperature difference for both quenching procedures is almost the same (4.5 % difference). Residual stresses were then measured in the middle of both samples. The results are shown in Figure 5.18, and a measurement in an annealed sample was also carried out for reference purposes. Here, a compressive residual stress maximum of about -1.6 MPa was measured at a depth of



0.3 mm. It was then possible to induce higher compressive residual stresses of about -14 MPa near the surface of polycarbonate components at a depth of about 0.1 mm by quenching them in water. The residual stresses then continuously decreased and were expected to become tensile in the core of the sample. Directly at the surface, small compressive residual stresses were measured. However, this result does not seem reliable since higher compressive residual stresses were expected (chapter 2.1.1.1). Differences between residual stress measurements of the two quenched samples are probably due to the quenching that was performed manually.

In conclusion, it was possible to induce high compressive residual stresses near the surface of polycarbonate samples by quenching them in water. The hole drilling method made it possible to measure a plausible residual stress profile with a maximum compressive residual stress value of about -14 MPa at 0.1 mm. Results in the first 0.1 mm do not seem reliable and should be interpreted with caution.

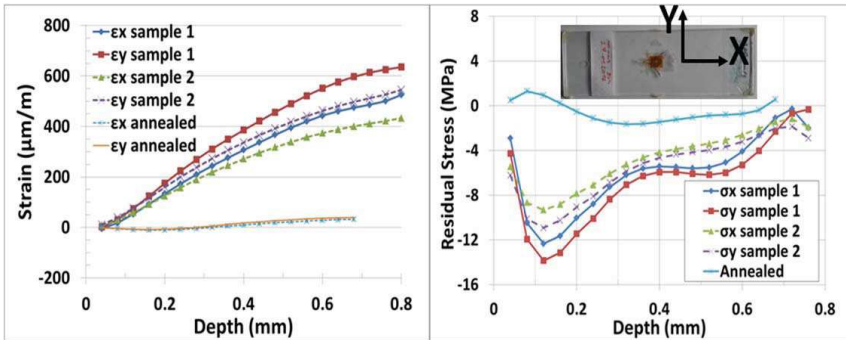


**Figure 5.18: Strain and residual stress measurements of two samples quenched from a temperature of about 150 °C to 20 °C. A measurement of an annealed sample is shown for reference purposes. Left: measured strains during the experiment in both direction X and Y. Right: calculated residual stresses in samples.**

### 5.2.2 Polypropylene

Similar experiments were carried out with polypropylene materials. Samples were injection moulded with the dimensions 180 mm x 20 mm x 3 mm. To obtain a homogeneous structure, they were annealed 4 hours at 135 °C and cooled to 70 °C. This temperature was maintained for two hours and then samples were slowly cooled down to room temperature. Samples were then separately heated to 135 °C, 125 °C and 75 °C and were subsequently quenched in water. Theoretical parabolic residual stress profiles like that of polycarbonate were expected with a compressive residual stress maximum at the surface (Figure 2.2). In Figure 5.19, if the temperature of the sample before quenching is higher, then the strain curve shifts in the tensile direction. As more tensile strains were relieved, more compressive residual stresses were induced in the material. In comparison to quenching polycarbonate, residual stresses

obtained after quenching polypropylene samples were not equibiaxial because the strains were particularly different in the longitudinal direction X and in the transverse direction Y of the sample. Residual stresses were calculated in the longitudinal direction X of the sample (Figure 5.20 left) and in the transverse direction Y of the sample (Figure 5.20 right). As expected, quenching the sample from higher temperature in water induced more compressive residual stresses in the material. The profile of residual stresses in the sample quenched from a temperature of 135 °C was below that of the samples quenched from 125 °C and 75 °C in both the directions X and Y near the surface. Furthermore, compressive residual stresses were higher in the transverse direction of the samples with a maximum compressive residual stress of about -2 MPa (direction Y) compared to -1 MPa (direction X) at a depth of about 0.25 mm for the sample quenched from a temperature of 135 °C. Results in the first 0.1 mm should be interpreted cautiously, because they are highly influenced by measurement errors induced by residual stresses in the strain gauge rosette (chapter 4.3.3). In the longitudinal direction X, tensile residual stresses were predominant near the surface even though compressive residual stresses were expected. At a depth of 0.1 mm, residual stresses were about 1.5 MPa for both samples quenched from 125 °C and 75 °C and they were about 1 MPa for the sample quenched from 135 °C. Differences between expected residual stresses and measurements may be related to crystal developments in the sample at about 110 °C during the annealing of samples. Since crystals (spherulites) are more compact than their original amorphous phases, their formation is restricted by the surrounding material. Therefore, new spherulites that grew near the surface are in a tensile residual stress state. The development of spherulites could be more restricted in the molecular-oriented direction of the sample, resulting in differences of residual stresses in the transverse and longitudinal directions. Thus, the residual stress state in the sample is a combination of thermal residual stresses and residual stresses caused by phase transformation. Another possibility is the pressure-induced residual stress during the injection process (chapter 2.1.1.2). This effect is known to induce tensile residual stresses near the surface. If so, the annealing procedure may not have relieved these tensile residual stresses.

In conclusion, even if more compressive residual stresses were obtained by quenching samples from 135 °C, the measured residual stresses did not correspond to the expected profile. Results may have been influenced by the development of spherulites near the surface or the unsuccessful annealing of samples. To obtain compressive residual stresses, samples should probably be heated close to their melting temperature at 165 °C. Then, after “melting” the sample, homogeneous crystal growth should be achieved by slowly cooling the sample. Finally quenching the samples should help to develop compressive residual stresses near the surface. More experiments are necessary to confirm these hypotheses.

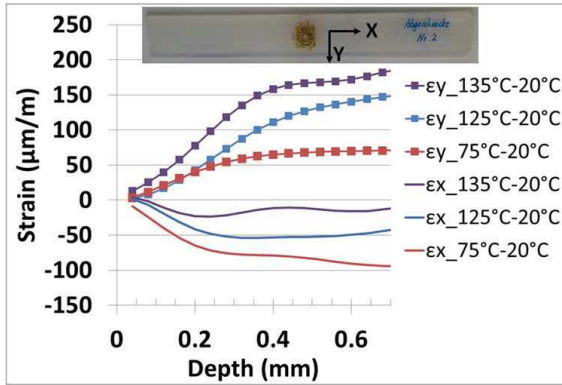


Figure 5.19: Strains measured in three quenched polypropylene samples. Samples were annealed at 135 °C and then slowly cooled down to room temperature. Then they were heated up to respectively 135 °C, 125 °C and 75 °C and finally quenched in 20 °C water.

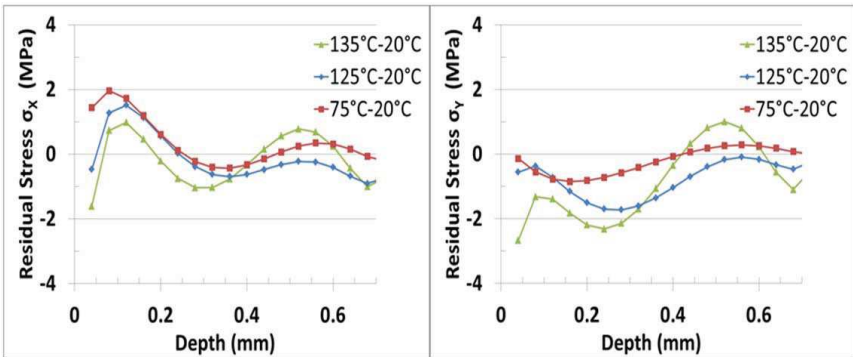


Figure 5.20: Residual stress measurements of three samples quenched in water. Samples were annealed at 135 °C then slowly cooled down to room temperature. They were finally heated to 135 °C or 125 °C or 75 °C and quenched in 20 °C water. Left: residual stresses in the longitudinal direction X of samples. Right: residual stresses in the transverse direction Y of samples.

### 5.3 Quantitative validation and influence of residual stresses

In chapters 5.1 and 5.2, measurements illustrated that residual stresses are influenced by processing parameters and post-processing procedures such as annealing or quenching. In some cases, assumptions about the reliability of residual stress analysis were made. In order to assess the results of the residual stress analysis, it is necessary to investigate the accuracy of the residual stress measurements. Figures 5.21-22 show a measuring set-up used to induce a bending stress state in a sample. After loading the sample with a weight, stresses at the surface were measured with a strain gauge rosette. The profile along the depth was then assumed to be linear as

proposed in the beam theory with the assumption of linear elasticity. As the induced load was added to pre-existing residual stresses in the sample, two possibilities were available to measure the induced bending load with the hole drilling method. The first method involved annealing the sample in order to completely relieve the pre-existing residual stresses in the sample. Then the sample can be loaded, and a stress measurement should measure the induced bending load. However, material properties may be influenced by the annealing process, which means this procedure is not applicable for all type of samples. This procedure was used for polycarbonate because the samples were considered to be homogeneous and amorphous throughout the whole depth. The second possibility to measure the bending load was to perform a residual stress measurement first without loading the sample. In doing so, the initial residual stress state in the sample was determined. Subsequently, the same sample was loaded and a new stress measurement was able to be carried out near the first measurement to measure the total stress (residual stresses and bending load). A comparison of both measurements should reveal the induced bending load in the sample, because the bending load is added to initial residual stresses in the material assuming that no plastic deformation occurs. This procedure was chosen for polypropylene samples due to the fact that annealing the sample could modify its structure. This procedure was also chosen for self-reinforced polypropylene samples for which annealing could result in a loss of material reinforcements.

After having demonstrated that the residual stress measurements are accurate, it is shown how residual stresses influence material properties. For this purpose, different residual stresses were induced near the surface of a polycarbonate sample. Then, the sample was bent, and evidence that the resistance to environmental stress cracking was highly influenced by the initial residual stress state in the material while subject to a bending load is provided.

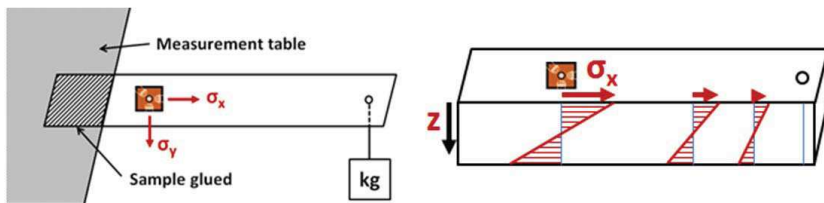


**Figure 5.21: Measurement set-up to induce a known loading stress state in a sample.**

### 5.3.1 Bending of a 4 mm thick polycarbonate sample

Samples made of polycarbonate with the dimensions 160 mm x 40 mm x 4 mm were annealed for 4 hours at 115 °C and then slowly cooled down to 70°C. This temperature was held for two hours, and, finally, the samples were slowly cooled down to room temperature. This way, initial residual stresses in the samples were relieved. In order to induce a bending moment in the sample, a weight of about 1 kg

was attached to the sample and a bending length of about 100 mm was realised (Figures 5.21 and 5.22). After attaching the weight, strains of about 0.3 % were measured in the longitudinal direction X at the area of interest ( $\epsilon_x = 3046 \mu\text{m/m}$  in the longitudinal direction;  $\epsilon_y = -676 \mu\text{m/m}$  in the transverse direction Y and  $\epsilon_{45^\circ} = +1110 \mu\text{m/m}$  at an angle of  $45^\circ$ ). This corresponds to a stress in the longitudinal direction X of about 8 MPa by applying Hook's law for elastic materials. This stress is relevant, because it has a similar value as the residual stress measurements performed on the same material (Figure 5.3 and Figure 5.18). Deeper in the material, a linear load stress profile was assumed as proposed by the beam theory (Figure 5.21).

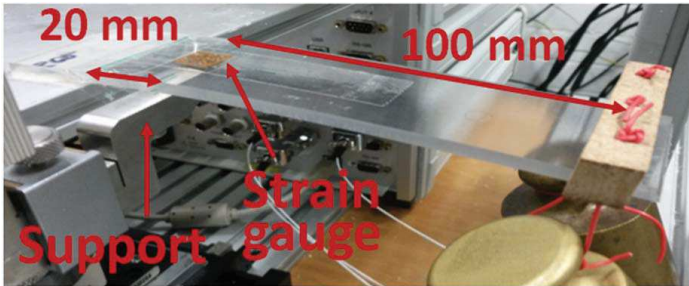


**Figure 5.22: Polycarbonate sample under bending. 1 kg was fixed to the sample. A support is put close to the strain gauge to limit bending during the drilling process.**

Sample preparations are of importance for the experimental set-up. First, the sample should be supported under the area of interest to limit bending while the drilling tool is pushed into the sample, and to ensure that the right amount of material was drilled (Figure 5.22). If the bottom of the sample is left without support, a 0.7 mm deep blind hole would be drilled instead of one that is 0.8 mm. Furthermore, the strain gauge rosette for hole drilling measurements should be glued onto the sample after loading. If the strain gauge rosette is glued onto the sample before loading, both the sample and strain gauge will be stretched after fixing the weight. Since the material and strain gauge have similar elastic Young's moduli, the load stress would not only be present in the sample but also in the strain gauge. Consequently, after drilling the foil of the stressed strain gauge, high relaxations would be measured in the influenced measurement. About  $110 \mu\text{m/m}$  were measured after drilling the foil of a medium size strain gauge rosette EA-062RE and  $280 \mu\text{m/m}$  were measured after drilling the foil of a small strain gauge EA-031RE (Vishay Micro-Measurements). This effect is caused by the total stresses in the strain gauge as described in chapter 4.3.3. The consequence it has on the result can be seen in Figures 5.23.a (EA-031RE) and 5.23.c (EA-062RE). The dotted lines correspond to the expected load stress of the beam theory. Results obtained with the small strain gauge near the surface in the longitudinal direction X were overestimated by a factor of two (Figure 5.23.a). In the case of the medium size strain gauge (Figure 5.23.c), the results were more accurate. Load stresses were

overestimated at a depth of about 0.15 mm with a value of 9 MPa instead of 7 MPa in the direction X, and then load stresses in the direction X converged to the expected load stresses from the beam theory. Accuracy reduced below a depth of 0.6 mm. To avoid inducing stresses in the strain gauges, they were later glued onto the sample after bending the sample. However, gluing after bending the sample caused a new problem. Due to tensile stresses induced by bending, environmental stress cracking could occur if the glue or coating was applied at the surface of the stretched samples. The strain gauge needs to be glued on as fast as possible, otherwise cracks develop below the strain gauge and the measurement becomes unreliable. This can be seen in the result presented in Figure 5.23.b where cracks have relieved load stresses near the surface or may have influenced the measured strains, because cracks were also located below the strain grids.

Using the proposed experimental set-up and avoiding the formation of environmental stress cracking, measurements were reproduced two times and satisfying accuracy was able to be achieved (Figures 5.24.b and d). In fact, in Figures 5.24 (b) and (d), the measured load stresses with the hole drilling method are near the expected values from the beam theory. At a depth of 0.1 mm, load stresses of about 7.5 MPa (graph b) and 9.5 MPa were measured for respective expected load stresses of 7.5 MPa and 8 MPa. Deeper in the material, load stresses converged with values from the beam theory with less than 0.5 MPa difference. Another possibility to avoid environmental stress cracking is to bend the sample surface of interest in the other direction. Then compressive stresses should be measured at the surface of the sample. When using this option, no environmental stress cracking was observed. Residual stresses were measured with the small strain gauge EA-031RE in an attempt to improve accuracy of the results near the surface (Figure 5.24.f). The measured residual stresses range around the expected value with an accuracy of about 2 MPa, therefore no improvement was obtained near the surface. Consequently, it is recommendable to use the medium size strain gauge EA-062RE, which provides information deeper into the material than the small strain gauge with a sufficient accuracy near the surface.

In conclusion, by means of annealing and bending samples made of polycarbonate, it is possible to measure load stresses with an accuracy of about 1-2 MPa from 0.1 mm up to 0.25 mm, and then accuracy improves to 0.5 MPa. Errors obtained during this validation procedure were mostly due to the experimental set-up. This shows that understanding the effects occurring during a measurement is the key to improving the accuracy of results.

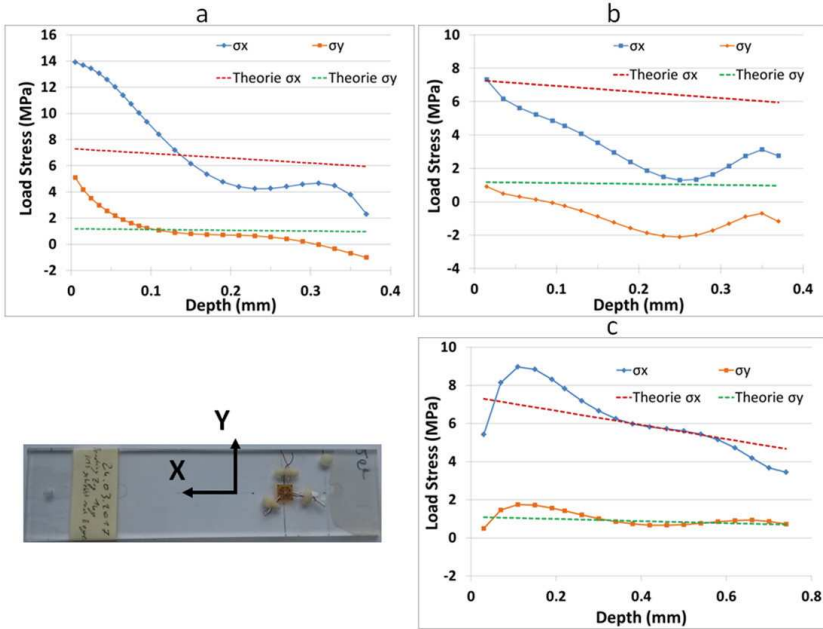


Figure 5.23: Load stress measurements performed with the hole drilling method in bent polycarbonate samples. Samples were relieved of residual stresses prior to bending by annealing. Graphs (a) and (c) show measurements with different strain gauge sizes glued onto the sample prior to bending. Graph (b) shows results where the strain gauge was applied after bending the sample. For graph (b), environmental stress cracking was observed under the strain gauge.

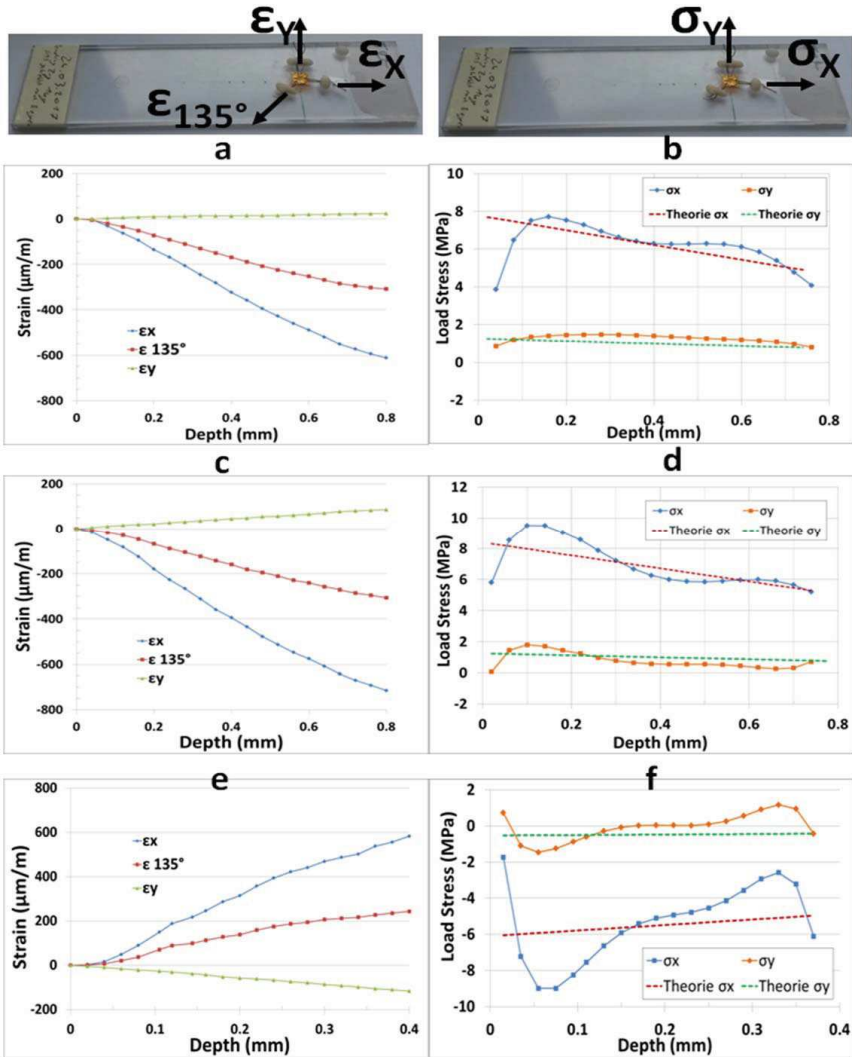


Figure 5.24: Load stress measurements in bent polycarbonate samples. Samples were relieved of stress prior to bending. Graphs a-b-c-d correspond to samples that were bent, inducing tensile stresses at the measured surface; a hole 2 mm in diameter was drilled. The last sample was bent in the opposite direction, inducing compressive stresses at the measured surface (e-f); in this case, a hole with a 1 mm diameter was drilled.



### 5.3.2 Influence of residual stresses on environmental stress cracking

During the measurements described in chapter 5.3.1, environmental stress cracking was observed in polycarbonate samples after applying a coating or glue on the tensile loaded side of bent samples. Samples were bent to about 0.3% strain and environmental stress cracking occurred after several seconds. This cracking was characterized by the propagation of a crack at the top of the sample that occurred when the area of interest was sufficiently stretched due to the bending moment. The following experiment was carried out to demonstrate that residual stresses directly influence environmental stress cracking. Four polycarbonate samples with the dimensions 160 mm x 25 mm x 4 mm were bent identically with a weight of 500 g as described in chapter 5.3.1. About 10 MPa of stress was induced at the maximum bending length of 130 mm. To induce compressive stresses which should improve the resistance to environmental stress cracking, samples were quenched from 140 °C in 20 °C or 0 °C water prior to bending. This quenching process is known to induce compressive residual stresses like those measured in chapter 5.2.1 (Figure 5.18). Since the samples could easily deform at 140 °C, samples were placed horizontally during quenching to make the handling of the samples easier. Then, one of the surfaces of the sample came into contact with the water during quenching. After quenching, little distortion of the samples was observed. For that reason, two samples were quenched from 140 °C to 0 ° and two different residual stress states were achieved on both sides of these samples.

In order to activate the environmental stress cracking, samples were bent and the strain gauge polyurethane coating M-Coat A (Vishay Micro-Measurements) was applied. Different total stress states were achieved on the surfaces of the bent samples, because the bending load was added to initial residual stresses. Therefore, different degrees of resistance to environmental stress cracking were achieved. Results are shown in Figure 5.25. Sample (a) was annealed and sample (b) was quenched from 140 °C to 20 °C. Here, a high concentration of cracks formed in sample (a) due to quenching, and the minimum bending stress that produced cracks was about 5 MPa. As the bending length, and hence, the loading stress in the sample increased, the concentration of cracks increased. In sample (b), the concentration of cracks was reduced and the minimum required stress to produce a crack was also increased (about 6.5 MPa). This confirms the effect of compressive residual stresses near the surface. Increasing the temperature difference during quenching (samples c and d) and, thus, increasing the compressive residual stresses at the surface reduced the concentration of cracks. In conclusion, compressive residual stresses on the surface help to reduce environmental stress cracking in polycarbonate materials.

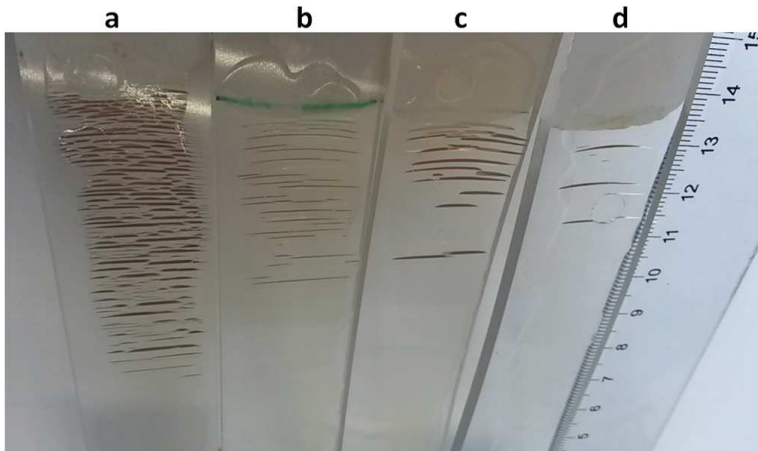


**Figure 5.25: Environmental stress cracking due to a combination of tensile bending load and a liquid applied on the surface (polyurethane strain gauge coating). Prior to bending, sample (a) was annealed. Sample (b) was quenched in water from 140 °C to 20 °C. Samples (c) and (d) were quenched in water from 140 °C to 0 °C.**

### 5.3.3 Bending of a 3 mm thick polypropylene sample

Similar to the investigations performed on the polycarbonate in chapter 5.3.1, polypropylene samples with the dimensions 180 mm x 20 mm x 3 mm were bent to induce a known load stress in the sample as explained before. It is important to point out that the measurement with the bending load was realised under constant stress, therefore, the material crept. Non-recoverable viscoelastic strain was neglected for simplification purposes. To avoid high viscoelastic strain rates during the measurement, the strain gauge was drilled 44 hours after loading the sample. Consequently, the total strain increased from 0.28 % to 0.60%, which could also have a detrimental effect on the measurement. Furthermore, since strains were small, linear viscoelastic behaviour of the material was considered. In case of linear viscoelasticity, not only the stress is a linear function of the surface distance (beam theory, Figure 5.21), but also of the viscoelastic strain. In addition, these polypropylene samples had a special structure characterized by an amorphous layer on the surface and spherulites of different sizes in the core (Figure 2.5). Owing to nano-indentation, the module of indentation varied with the depth (Figure 3.8). To conserve this specific structure, the samples were not annealed. That way, initial residual stresses were also present in the material and needed to be determined. Consequently, a measurement of an elastically bent sample with the hole drilling method should measure the total stresses, which is the sum of the bending stresses and the initial residual stresses.

Using the initial residual stresses makes it possible to carry out an estimation of the accuracy of measurements performed on polypropylene samples. Two evaluation

formalisms were used. Model 1 considers the elastic module gradient of the sample (see chapter 3.3.2) with a value of about 950 MPa at the surface and 1450 MPa at a depth of 0.8 mm. In contrast, model 2 considers the sample to be homogenous with a constant Young's modulus of 1400 MPa and a Poisson's ratio of about 0.4. Results can be seen in Figure 5.26. The graph (a) shows the initial residual stresses in the material and the graph (b) shows the total stresses measured while bending the sample. Graph (c) provides the difference between graphs (a) and (b), and corresponds to the load stress induced by the bending moment (red line). In graph (d), the bending stresses measured with the hole drilling method can also be seen, however, the load stresses were evaluated with both models 1 and 2. The theoretical bending load from the beam theory was again represented with a red line. To emphasize how the Young's modulus influences results, graph (e) shows the percentage difference between the average Young's modulus of the material and the local Young's moduli measured by means of nano-indentation (see Figure 3.8 as well for absolute values).

In Figure 5.8.a, initial residual stresses of the material have been depicted. The result shows a residual stress state similar to that of thermally induced residual stresses. Here, residual stresses were about -4 MPa in the transverse direction Y near the surface and -2 MPa in the longitudinal direction X. Then, the absolute residual stresses reduced and low tensile residual stresses between 0 and 1 MPa were present in both directions at a depth of 0.7 mm. After bending the sample (Figure 5.26.b), total stresses in the sample oscillated in both directions X and Y. This effect may be due to the load in the strain gauge, since high strain relaxations up to 120  $\mu\text{m}/\text{m}$  were measured after drilling the foil of the strain gauge (see chapter 4.3.3). The difference between graphs (a) and (b) can be seen in graph (c), where the measurement can be directly compared to the expected load stress. At a depth of 0.1 mm, a peak was observed and the difference between the measured load stress and the expected load stress was about 2 MPa. At a depth of 0.25 mm and deeper, maximum differences of 0.6 MPa were measured. In graph (d), the results again correspond to the load stress, but this time it was calculated with both models 1 and 2. Both models measured with similar accuracy as described above. The difference between the load stresses measured with both models reached its maximum at a depth of 0.04 mm and was about 2.4 MPa. Then the difference reduced to 0.7 MPa at a depth of about 0.2 mm. Deeper in the material, almost identical load stresses were measured by both models (less than 0.2 MPa difference). Furthermore, in graph (e) the elastic moduli measured by means of nano-indentation was about 65 % of the average elastic modulus at the surface of the material. Subsequently, the difference reduced and became less than 10 % at a depth of 0.1 mm.

In sum, it can be deduced that in this case, differences in the Young's moduli did not have a relevant influence on the load stress measurement at a surface distance of 0.2 mm and deeper. From 0.25 mm up to 0.7 mm, the measurement accuracy is about 1

MPa and results oscillate around the expected values. Therefore, it is not necessary to consider the gradient of the elastic properties of the material in this case.

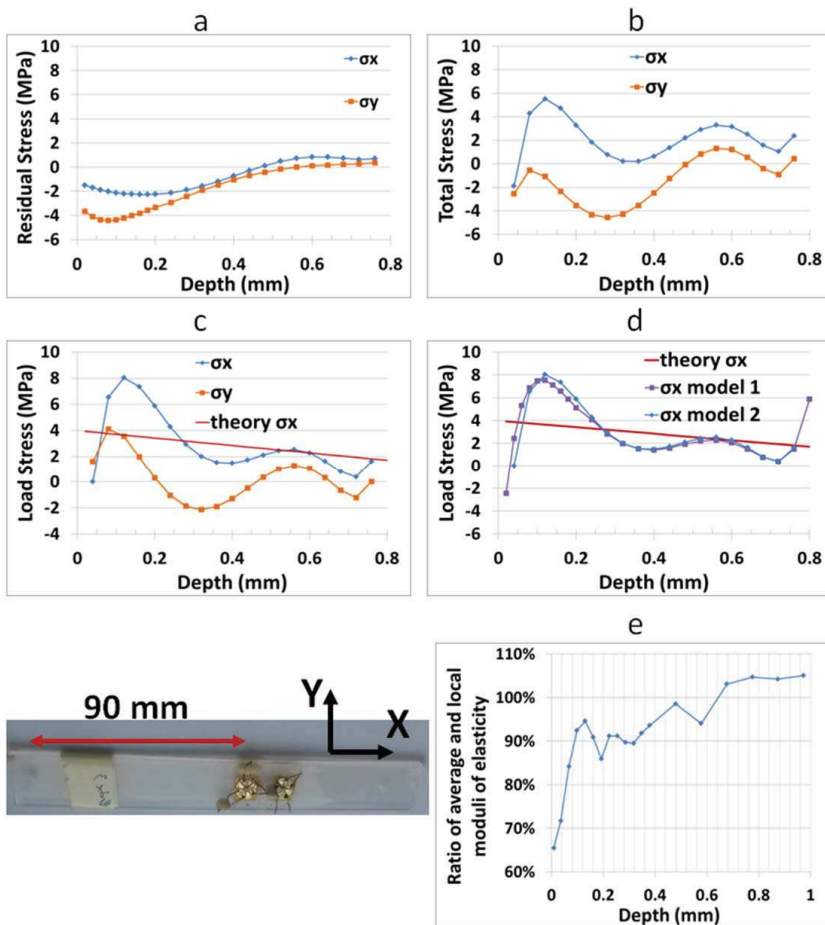


Figure 5.26: Residual stress measurements performed on polypropylene samples. Figure (a) corresponds to the initial residual stresses of the material. Figure (b) shows total stresses measured in the same sample while subject to bending. Figure (c) corresponds to the load stresses - the difference between figures (a) and (b). Figure (d) shows the same result by considering the sample to have an elastic property gradient (model 1) or the same Young's modulus in its entire structure (model 2). The ratio between the local Young's moduli and the average Young's modulus measured by nano-indentation can be seen in Figure (e).

#### 5.3.4 Bending of a 4 mm thick self-reinforced polypropylene composite

In order to evaluate the accuracy of measurements performed on self-reinforced polypropylene composites, samples with the dimensions 140 mm x 25 mm x 4 mm were bent to produce a known residual stress state in the sample. Two measurements were carried out on the same sample, which were separated by a distance of 20 mm. The first measurement was realised without loading the sample to obtain the initial residual stress state in the sample. In the second measurement, the sample was bent and the total stresses were analysed. To prevent strong viscoelastic strain rates from affecting the result, the measurement was performed two days after loading the sample, because the strain rate reduces with time. Here, the strain was about 0.2 % after loading and about 0.45 % 44 hours later. However, because the load was induced by a weight, the induced stress remained constant during the measurement.

As explained in chapter 5.1.3, a strain gauge with eight grids was used to average the scattering of data. Only the average value of residual stresses (calculated with different strain gauge configurations) is illustrated in figure 5.15. Direction X corresponds to the longitudinal direction of the sample and to the direction of the bending stress at the surface. Figures 5.27 (a) and (c) show the measured strain during the experiment. Graphs (a) and (b) correspond to the measurement of the initial residual stress state of the material (sample without loading). Graphs (c) and (d) correspond to the measurement with the same sample, but under a bending load. Graph (e) shows the difference between graphs (b) and (d) and should correspond to the bending moment induced in the sample. Graph (e) shows that the measurement in the longitudinal direction X is very close to the expected value with a loss of accuracy below a depth of 0.3 mm. This loss in accuracy may be due to defects in the material (voids) or local delamination. Load stresses along the transverse direction Y of the sample should have been zero due to the weight only having induced a bending stress in the longitudinal direction X. However, the measurement reveals an unexpected profile. High errors may be due to the woven structure of the material, because the crossing of filaments acts as a stress raiser locally.

Thus, the conclusion that measurements should be interpreted with caution was drawn. Due to material defects (delamination or voids in the material), measurements were not evaluable deeper than 0.3 mm. Residual stresses in the transverse direction Y of the material were not correctly evaluated. Therefore, the proposed experiment did not validate measurements of residual stresses in the self-reinforced polypropylene samples. Nevertheless, the residual stress measurement in the longitudinal direction X of the bending load was satisfactory. When working with woven composite structures, more statistics are required to evaluate the plausibility of measurements.

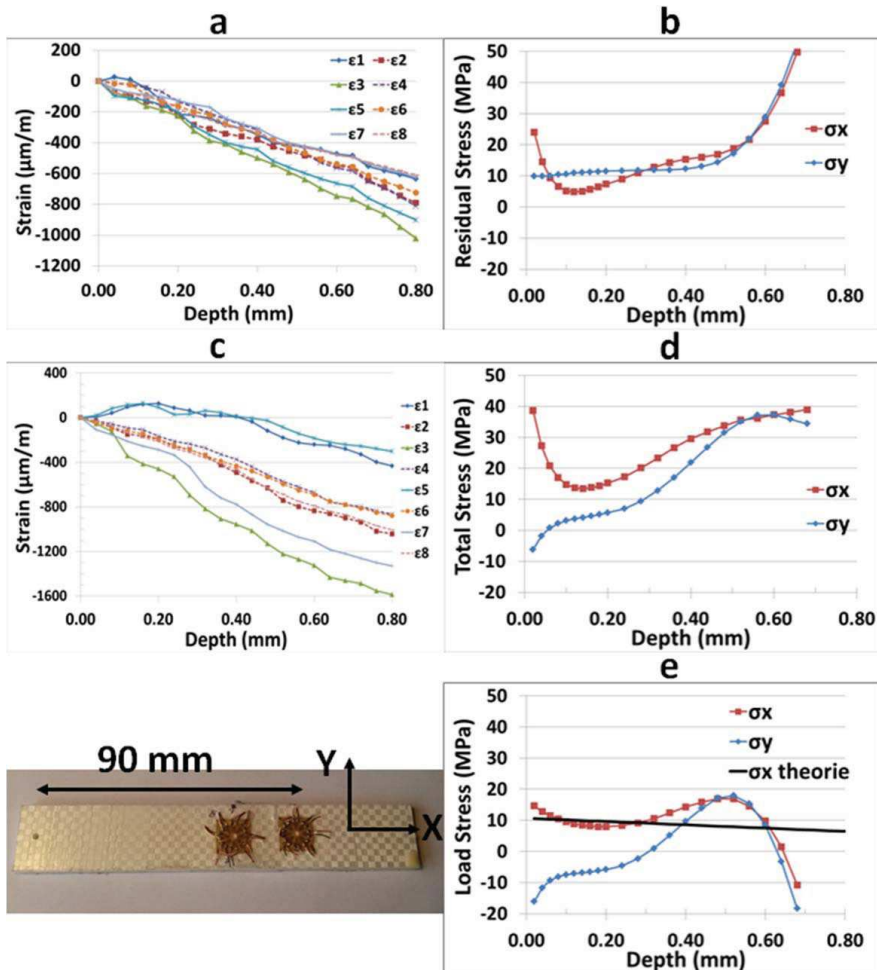
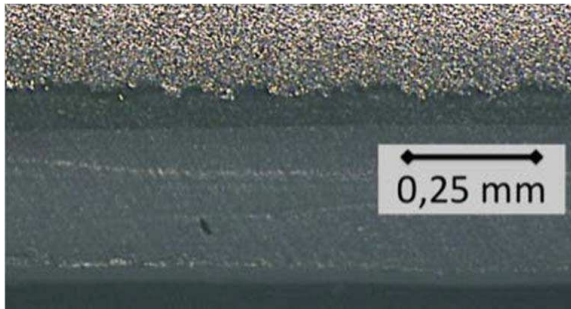


Figure 5.27: Residual stress measurements in a self-reinforced polypropylene. Graphs (a) and (b) correspond to the initial residual state of the material without a load. Graphs (c) and (d) correspond to the measurement of the total stress state in the same sample while subject to bending. A load stress of about 10 MPa was realized at a bending length of about 90 mm. Graph (e) represents the difference between graphs (b) and (d). In graph (e), the black line highlights the expected bending moment induced in the sample.

#### 5.4 Residual stress measurement in an hybrid structure made of aluminium and of a reinforced polypropylene

This example concerns a hybrid structure made of a sheet of 1 mm thin aluminium and of a 1 mm thin plate of self-reinforced polypropylene composite (Figure 3.6 and Figure 5.31). In Figure 5.28, a cross section of a similar hybrid

structure can be seen. To assure the bond between the aluminium and the self-reinforced composite, a thin polypropylene sheet was used between both materials. The aluminium surface was sand-blasted first to treat the structure. Afterward, a polypropylene foil was melted onto the aluminium plate in the oven at a temperature of about 200 °C. After melting the polypropylene foil onto the surface of the aluminium, the sample was taken out of the oven and cooled down at room temperature. Subsequently, a sheet of self-reinforced polypropylene was applied on the structure and the whole system was compressed in a press at a temperature of about 160 °C and with a pressure of about 4 MPa.



**Figure 5.28: Hybrid structure made of aluminium (top), polypropylene (middle) and self-reinforced polypropylene (bottom).**

The geometry of this structure is not covered by [ASTM 2013] because the sample is too thin and is composed of different materials. Therefore, it is necessary to verify the accuracy of hole drilling measurements (chapter 5.4.1). To demonstrate the possibility to measure thin samples, the same experiment was used as in chapter 5.3, where a known load was induced in polymer sheets by means of bending. However, in this case, a 1 mm thin steel sheet was used. In chapter 5.4.2, the real hybrid structure was measured on both sides. A residual stress equilibrium was expected to be found along the depth of sample since residual stresses are principally due to the difference in the thermal expansion coefficients between both materials. A specific finite element model was created for measurements of the self-reinforced polypropylene side of the hybrid structure in order to obtain calibration coefficient functions, which take the orthotropic properties of the material and the 1 mm the sheet of aluminium on the backside into account (chapter 3.3.1).

#### **5.4.1 Measurement validation in thin metal sheet**

To validate the accuracy of measurements in thin samples, thin steel sheets with the dimensions 140 mm x 25 mm x 1 mm were annealed prior to relieve the initial residual stresses in the material. Then, these samples were bent with a weight to induce about 110 MPa bending stress in the longitudinal direction X at the place where hole drilling measurements are realised (Figure 5.29). The yield stress of the material is

about 210 MPa, therefore, the measurements should not be influenced by plastic strain [Gibmeier 2000, Nobre 2018].

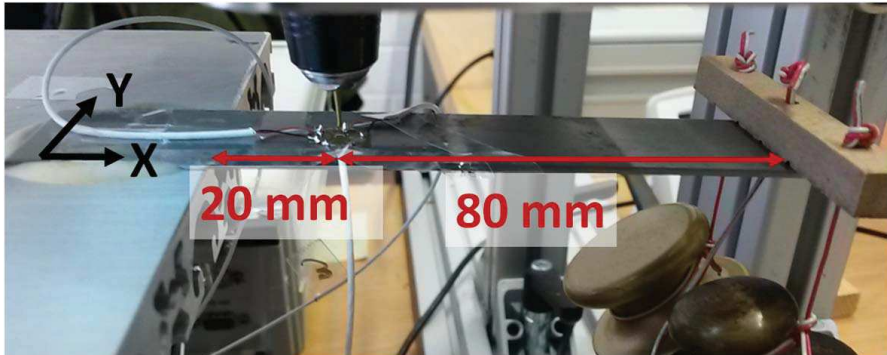


**Figure 5.29: Bent metal sheet with a weight. Bending length is about 80 mm and a bending stress of about 110 MPa is induced at the measured position. Sample is fixed by gluing.**

Results can be seen in Figure 5.30. Graph (a) shows the evaluation of stresses from the same measured strains, however the strain data was evaluated using different coefficient matrices (chapter 3.4.1). These coefficients were calculated with finite element analysis, where the thickness of the sample was varied. The dotted red line represents the expected results obtained from the beam theory. If the thickness of the sample was incorrectly considered to be thick (blue curve with thickness of 6 mm), then stresses were overestimated with errors of more than 50 % near the surface in the longitudinal direction X of the sample. Stresses in the transverse direction Y were measured even though they should have been almost zero (Figure 5.30.b). If the correct sample thickness was used (1 mm), then results correlated nicely with the theoretical curve from beam theory. This experiment was repeated three times and the difference between the theoretical values and the measured values (with the right coefficient matrices) can be seen in the longitudinal direction X in Figure 5.30.c and in the transverse direction Y in Figure 5.30.d. The results were accurate up to 0.5 mm with errors equalling less than 20 MPa. Results in metal up to 0.06 mm should be interpreted with caution. In this area, measurements with x-ray diffractions are preferred. Measurements deep in the material should also be interpreted carefully since they are influenced by special effects, such as the wearing of the drilling tool, and measurements become oversensitive to errors.

This verifies that measurements of thin metallic materials can be performed when using the precise material thickness. Regarding the hybrid structure, although it is 2 mm thick (1 mm aluminium and 1 mm self-reinforced polypropylene), the sample should not be considered to 2 mm thick for measurements performed on the



aluminium side. In fact, the stiffness of the polypropylene composite is negligible in comparison to the stiffness of the aluminium.

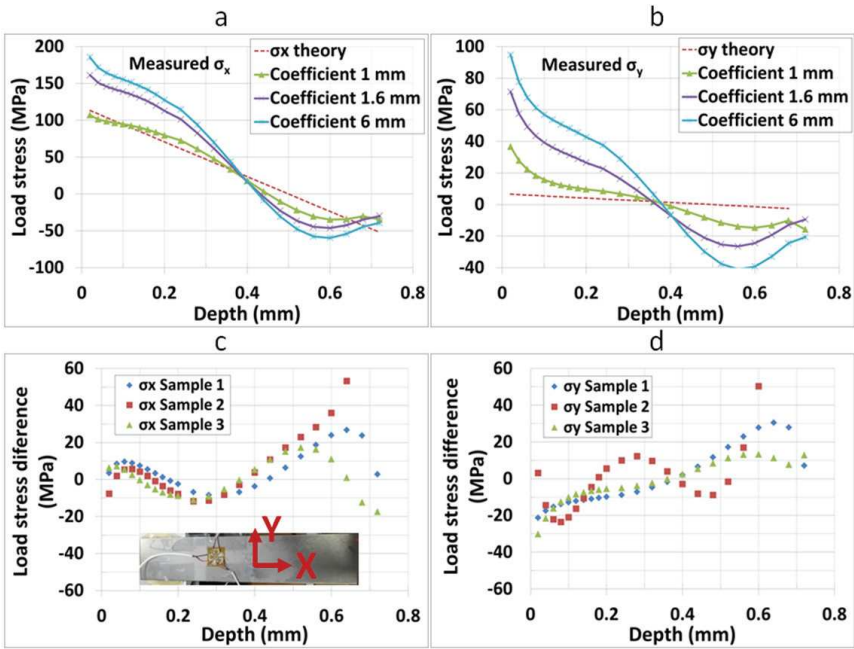


**Figure 5.30: Application of the hole drilling method on a 1 mm thin bent steel sheet. Each curve in graphs (a) and (b) corresponds to calculations of load stresses with different calibration coefficients. Dotted red lines highlight the expected load stresses from the elastic beam theory. Figures (c) and (d) show the difference between the theoretical load stresses and the measured load stresses with the correct coefficients. Experiments were reproduced three times.**

#### 5.4.2 Measurements in the hybrid structure

A hybrid structure made of self-reinforced polypropylene and aluminium was measured on both sides using the hole drilling method (Figure 5.31). An eight grid strain gauge was used for the measurement of the self-reinforced polypropylene. As mentioned before in chapter 5.1.3, the average values obtained using eight strain gauge configurations were evaluated. To increase the reliability of measurements in aluminium, X-ray diffraction was also used before drilling holes. Measurements were carried out with a copper anode and a collimator with a 2 mm diameter. The  $\sin^2 \psi$ -method was used with the lattice plane  $\{511\}$  was used for residual stress analysis. In doing so, it was possible to measure residual stresses in the aluminium on both sides. The side in contact with the polypropylene was also able to be measured since the energy absorption capacity of polypropylene is low and the X-ray penetrated through

the polypropylene. Results from X-ray measurements are represented with a blue point in Figure 5.32.

On the surface of the aluminium (2 mm), the residual stress was about -1 MPa when using X-ray diffraction and about 18 MPa when using the hole drilling method 0.05 mm deeper in the material (depth = 1.95 mm). On the other side of the aluminium (1 mm), the X-ray diffraction measured a compressive residual stress of about -70 MPa, and this compressive residual stress is probably a result of the prior sandblasting of the aluminium. Furthermore, thermal shrinkage of the self-reinforced polypropylene should also lead to compressive residual stresses in aluminium at the transition point between both materials. Tensile residual stresses were expected to form on the surface of the aluminium (2 mm) due to the bending of the plate induced by the shrinkage of the self-reinforced polypropylene. On the aluminium side, the bending of the sample can explain the overall, in-depth decrease of the residual stress, which oscillates with an amplitude of around 20 MPa. In the case of the self-reinforced polypropylene, measurements performed within the first 0.1 mm were not reliable. Tensile residual stresses of about 11 MPa were measured at a depth of about 0.1 mm. The residual stresses then slowly increased to 17 MPa at a depth of about 0.5 mm. Similar profiles were obtained and depicted in Figure 5.27.b in the case of a 4 mm thick self-reinforced polypropylene without aluminium. However, residual stresses were about 5 MPa lower. The small increase of the residual stresses is probably caused by the restrained shrinkage of the self-reinforced polypropylene. 0.5 mm away from the surface and deeper in the material, residual stresses strongly diverge, which does not seem plausible.

Measurements performed on the self-reinforced polypropylene with an eight grid strain gauge seem plausible from 0.1 mm to 0.5 mm, because residual stresses in the material could compensate the compressive residual stresses in the aluminium. Still, more measurements are necessary to confirm this assumption.

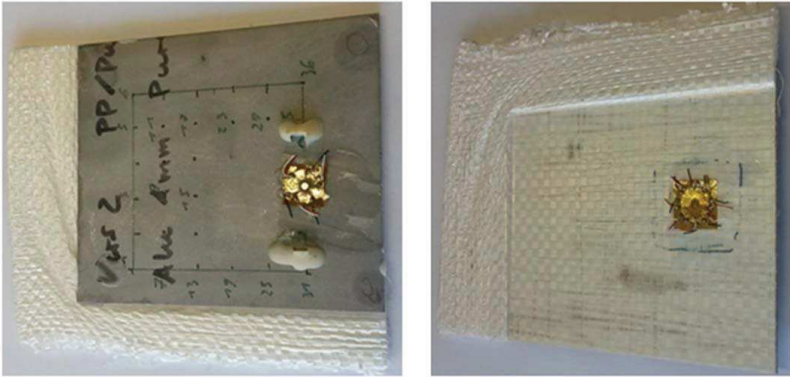


Figure 5.31: Hybrid structure composed of a 1 mm thin layer of self-reinforced polypropylene and of a 1 mm thin aluminium sheet. Strain gauges were applied on both sides of the structure.

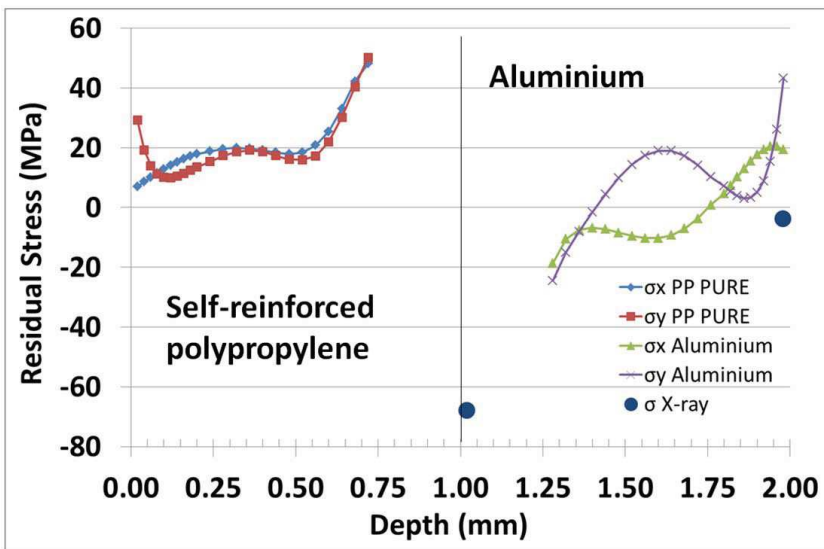


Figure 5.32: Residual stress measurements with the hole drilling method performed on a hybrid structure composed of a 1 mm thin aluminium sheet and of a 1 mm thin layer of self-reinforced polypropylene. Residual stresses were also measured by means of X-ray diffraction on both sides of the aluminium.

## 6 Conclusion and outlook

This study successfully demonstrated that the hole drilling method can be adapted to polymer materials. Two thermoplastic materials, an amorphous material (polycarbonate) and a semi-crystalline material (polypropylene), a self-reinforced polypropylene composite (PURE), and a hybrid aluminium/PURE compound were investigated.

In finite element analysis (chapter 3), calibration coefficients were calculated to expand the standard method ASTM to the specificity of the geometries and materials used. In the case of thin materials (chapter 3.4.1), calibration coefficients were calculated to take the higher deformation of the material into account during the drilling procedure. When drilling a hole 2 mm in diameter into a 1 mm thick sample, neglecting the thickness of the sample can result in errors of approximately 70 % (chapter 5.4.1). Regarding polypropylene components, it is possible to incorporate the structural gradient of the material into the finite element model, namely the thin amorphous layer on the surface and the semi-crystalline structure of the core (chapter 3.3.2). Minimum differences were found in the depth of the material, therefore it is not necessary to respect this structure specificity (chapter 5.3.3). Lastly, in order to investigate residual stresses in a composite structure, e.g. a self-reinforced polypropylene composite, a formalism was introduced to include the orthotropic elastic behaviour of the material in the evaluation (chapter 3.2). If the orthotropic behaviour of this material is neglected, significant errors of up to 200 % occur (chapter 5.1.3). In addition, the calculation formalism was also adapted to an eight grid strain gauge to average the scattering of the results.

Having already determined the calibration coefficients to calculate residual stresses from measured relieved strains, it was necessary to select a strategy to measure a correct and well-defined elastic strain. Measuring polymer materials in the same way as metallic materials leads to erroneous results (chapter 4). Indeed, polymer materials are more sensitive to thermal and viscoelastic effects (chapter 4.3.1). Therefore, it is necessary to avoid any temperature fluctuations during measurements, for example, by reducing the drilling speed to several rotations per minute. Due to the high thermal dilatation and viscoelastic behaviour of polymer materials, time-dependent effects occur during the measurements. After gaining a profound comprehension of thermal strains and viscoelastic strains measured during the experiments, a pragmatic evaluation procedure was proposed and the relieved elastic strains were able to be obtained (chapter 4.4). In doing so, it was possible to obtain reproducible residual stress measurements with the best accuracy.

An experimental set-up was proposed to demonstrate the accuracy of measurements. By means of bending samples, a known load was induced in samples. Measuring the

total stresses in the samples demonstrated that the accuracy of residual stress measurements in polycarbonate samples was at least 0.5 MPa from a surface depth of 0.25 mm up to 0.7 mm, and it reduced to about 1 MPa between 0.1 mm and 0.25 mm (chapter 5.3.1). Using the same validation procedure, the accuracy of measurements performed on polypropylene was determined to be two times lower than that of polycarbonate samples (chapter 5.3.3). Results in the first 0.1 mm are not evaluable due to residual stresses in the strain gauge (chapter 4.3.3).

Finally, the hole drilling method was employed to investigate the influence of processing parameters of injection moulding on polycarbonate and transmission laser welding of polypropylene components. When injection moulding polycarbonate, the mould temperature and the injection rate have a significant impact on the residual stress state in the material (chapter 5.1.1). Residual stresses range between -4 MPa and 2 MPa. By means of quenching the same material, it was possible to induce about -14 MPa compressive residual stresses near the surface (chapter 5.2.1). This verified that the resistance to environmental stress cracking could be improved considerably with compressive residual stresses (5.3.2). In the case of the transmission laser welding process, high tensile residual stresses were measured. This showed that melting the polypropylene leads to tensile residual stresses between 2 MPa and 9 MPa near the joint (5.1.2). In the case of a hybrid structures made of a layer of aluminium and a self-reinforced polypropylene, it was also possible to measure residual stresses, which were found in an approximate equilibrium in the depths of the material (chapter 5.4.2). However, measurements of the self-reinforced polypropylene were found to be highly erroneous when measuring deeper than 0.4 mm, which is probably due to increasing damage in the material during the drilling process.

In conclusion, the basic principles of the hole drilling method have been outlined to enable reliable local residual stress measurements to be performed on polymer materials. Furthermore, the polymer materials have the advantage of being more sensitive to measurement errors, meaning new sources of errors were able to be highlighted. The obtained results of the present study can be transferred to other investigations to increase the reliability of measurements in the case of other materials, e.g. measurements performed on metallic materials. Additionally, optic measuring systems for residual stress analysis (ESPI, DIC) can surely benefit from the results obtained in this study. Future investigations should focus on advancing the measurement principles for composite structures, i.e., carbon/epoxy composites.

## References

- Ajovalasit A., Zuccarello B. (2005): Local reinforcement effect of a strain gauge installation on low modulus materials. *Strain analysis* 40 (7), 643-653.
- Ajovalasit A., D'Acquisto L, Fragapane S. et al (2007): Stiffness and reinforcement effect of electrical resistance strain gauges. *Strain* 43, 299-305.
- Ajovalasit A. (2011): Advance in strain gauge measurement on composite materials. *Strain* 47, 313-325.
- Akbari S., Taheri-Behrooz F., Shokrieh M.M. (2014): Characterization of residual stresses in a thin-walled filament wound carbon/epoxy ring using incremental hole drilling method. *Composites Science and Technology* 94, 8-15.
- Alcock B., Cabrera N.O., Barkoula N.-M. et al. (2006): The mechanical properties of unidirectional all-polypropylene composites. *Composites: Part A Applied Science and Manufacturing* 37(5), 716-726.
- Allahkarami M., Bandla S., Hanan J.C. (2016): Residual stress in injection stretch blow molded PET bottles. Springer. Conference proceedings of the society for experimental mechanics series. Vol. 9, 285-290.
- ASTM 2013: "Standard Test Method for Determining Residual Stresses by the Hole-Drilling Strain-Gage Method", ASTM International, ASTM E837-13 (2013)
- Baaijens, F.P.T. (1991): Calculation of residual stresses in injection molded products. *Rheologica Acta* 30(3), 284-299.
- Baldi A. (2005): A new analytical approach for hole drilling residual stress analysis by full field method. *Journal of Engineering Materials and Technology* 127(2), 165-169.
- Baldi A. (2007): Full field methods and residual stress analysis in orthotropic material. I Linear approach. *International Journal of Solids and Structures* 44, 8229-8243.
- Baldi A. (2007): Full field methods and residual stress analysis in orthotropic material. II: Nonlinear approach. *International Journal of Solids and Structures* 44, 8244-8258.
- Baldi A. (2014): Residual stress measurement using hole drilling and integrated digital image correlation techniques. *Experimental mechanics* 54, 379-391.
- Bayern: Photoelastic Stress Analysis of polycarbonate medical parts. By Mark Yeager. Bayer MaterialScience LLC.
- Behnken H., Chauhan D., Hauk V. (1991): Ermittlung der Spannungen in polymeren Werkstoffen – Gitterdehnungen, Makro- und Mikro-Eigenspannungen in einem Werkstoffverbund Polypropylen/Al-Pulver. *Mat.-wiss. U. Werkstofftech.* 22, 321-331.
- Behnken H., Hauk V. (1993): Röntgenographische Elastizitätskonstanten teilkristalliner Polymerwerkstoffe. *Matt.-wiss. U. Werkstofftech.* 24, 356-361.

Casavola C., Cazzato A., Moramarco V. et Al (2017): Residual stress measurement in fused deposition modeling parts. *Polymer testing* 58, 249-255.

Flaman M.T. (1982): Brief investigation of induced drilling stress in the center method of residual-stress measurement. *Experimental Mechanics* 22, 26-30.

Garcia Sobolevski, E. (2007): Residual stress analysis of components with real geometries using the incremental hole-drilling technique and a differential evaluation method, PhD Thesis. Kassel

Gibmeier J., Kornmeier M., Scholtes B. (2000): Plastic deformation during application of the hole drilling method. *Material Science Forum* 347-349, 131-136.

Gibmeier J., Scholtes B. (2016): Fortbildungsseminar, Entstehung, Ermittlung und Bewertung von Eigenspannungen. DGM Fortbildungsseminar.

Giroud T. (2001): Mesure et calcul des contraintes résiduelles dans les pièces injectées en thermoplastiques avec et sans fibres de renfort. Dissertation, Ecole des Mines de Paris.

Guevara-Morales A., Figueroa-López U. (2014): Residual stresses in injection molded products. *Journal Material Science* 49, 4399-4415.

Heim H.-P., Ries A., Bledzki A. K. (2011): Challenge of functional gradation of self-reinforced polypropylene composites. *International Conference Seico 11 Paris 32<sup>nd</sup>*, 148-155.

Heim H.-P., Ries A., Schöppner V. et al. (2014): Eigenverstärkte Thermoplastverbunde. *Kunststoffe* 02: 35-39.

Held E. (2013): Eigenspannungsanalyse an Schichtverbunden mittels inkrementeller Bohrlochmethode. *Karlsruher Institut für Technologie*. Dissertation.

Hornberger L.E., Devries K.L. (1987): The effects of residual stress on the mechanical properties of glassy polymers. *Polymer engineering and science* 27 (19), 1473-1478.

Housmans J.-W., Gahleitner M. et al. (2009): Structure-property relations in molded, nucleated isotactic polypropylene. *Polymer* 50, 2304-2319.

Hutař P., Ševčík M., Frank A. et al. (2013): The effect of residual stress on polymer pipe lifetime. *Engineering fracture mechanics* 108, 98-108.

Isayev A. I and Crouthamel D.L. (1984): Residual stress development in the injection molding of polymers. *Polymer plastics technology and engineering* 22(2), 177-232.

Jansen J. A. (2005): Environmental stress cracking – examples from the automotive industry. *Antec proceedings, Society of plastics engineers*.

Jansen K.M.B. (1994): Residual stresses in quenched and injection moulded products. *International polymer processing IX*, 82-89.

- Jansen K.M.B. (1996): Effect of pressure history on shrinkage and residual stresses – Injection molding with constrained shrinkage. *Polymer engineering and science* 36(15), 2029-2040.
- Kim C.H., Youn J.R. (2007): Determination of residual stresses in injection-moulded flat plate: Simulation and experiments. *Polymer testing* 26, 862-868.
- Kim C.H., S. Kim, Oh H., Youn J.R. (2007): Measurement of residual stresses in injection molded polymeric part by applying layer-removal and incremental hole-drilling methods. *Fibers and polymers* 8(4), 443-446.
- Kirsch E.G. (1898): Die Theorie der Elastizität und die Bedürfnisse der Festigkeitslehre. *Zeitschrift des Vereines deutscher Ingenieure*, 42, 797-807.
- Klein J., Gibler M.J., Jacobs R. M. et Al (2016): Environmental Stress Cracking of Medical Thermoplastics: Assessing Lifetime of High Performance Amorphous Resins in Presence of Hospital Cleaners. *Antec proceedings, Society of plastics engineers* 1353-1359.
- Kornmeier M., Scholtes B. (1999): Analyse von Abschreck- und Verformungseigenstressen mittels Bohrloch- und Röntgenverfahren. Bewertung von Mikroeigenstressen und Untersuchung der Plastizierung beim inkrementellen Bohrlochverfahren.
- Kreimeier Sooriyapiragasam S., Hopmann C. (2016): Modeling of the heating process during the laser transmission welding of thermoplastics and calculation of the resulting stress distribution. *Welding in the World* 60(4), 777-791.
- Macherauch E., Wohlfahrt H. (1977): Die Ursachen des Schweißspannungszustandes. *Materialprüfung* 19, 272-280.
- Macías C., Meza O., Pérez E. (2015): Relaxation of residual stresses in plastic cover lenses with applications in the injection molding process. *Engineering Failure Analysis* 57, 490-498.
- Makino 1994: A. Makino, D. Nelson, Residual-stress determination by single-axis holographic interferometry and hole drilling – Part I: Theory
- Makino A., Nelson D. (1994): Residual-stress determination by single-axis holographic interferometry and hole drilling – Part I: Theory. *Experimental Mechanics* 34(1), 66-78.
- Nau A., Scholtes B., Nobre M. et al. (2011): Application of the hole drilling method for residual stress analyses in components made of polycarbonate. *Journal of plastics technology* 7(3), 67-85.
- Nau A., von Mirbach D., Scholtes B. (2013): Improved calibration coefficients for the hole-drilling method considering the influence of the Poisson ratio. *Experimental Mechanics* 53: 1371-1381.
- Nau A. (2015): A contribution to enlarge the application limits of residual stress analyses by the hole-drilling and the ring-core method. Kassel University. PhD Thesis.



- Nobre J.P., Oliveira M., Albertazzi A. et al. (2014): Assessing shot-peening residual stresses by using the incremental hole-drilling technique and laser interferometry (DSPI). *Advanced Materials Research* 996, 269-276.
- Nobre J.P., Kornmeier M., Scholtes B. (2018): Plasticity effects in the hole-drilling residual stress measurement in peened surfaces. *Experimental Mechanics* 58(2), 369-380.
- Pagliaro P., Zuccarello B. (2007): Residual stress analysis of orthotropic materials by the through-hole drilling method. *Experimental Mechanics* 47, 217-236.
- Parlevliet P.P., Bersee H.E.N., Beukers A. (2006): Residual stresses in thermoplastic composites-A study of the literature-Part I: Formation of residual stresses.
- Persson J., Zhou J.M. Ståhl J.E. (2014): Characterizing the mechanical properties of skin-core structure in polymer molding by nanoindentation. The 6<sup>th</sup> Swedish Production Symposium.
- Pötsch G. and Michaeli W. (2008): Injection molding. An introduction. Carl Hanser Verlag.
- Rickert T. (2016): Residual stress measurement by ESPI hole-drilling. *Procedia CIRP* 45, 203-206.
- Sánchez-Beita S., Crespo de Antonio M., Acuña L. (2015): Applicability of the Hole-Drilling procedure for stresses quantification in timber bending elements in service. *Construction and Building Materials* 93, 798-805.
- Schajer G. (1993): Use of displacement data to calculate strain gauge response in non-uniform strain fields. *Strain* 29(1):9-13.
- Schajer G.S. and Yang L. (1994): Residual-stress measurement in orthotropic materials using the hole-drilling method. *Experimental Mechanics* 34(4), 324-333.
- Schwarz T. (1996): Beitrag zur Eigenspannungsermittlung an isotropen, anisotropen sowie inhomogenen, schichtweise aufgebauten Werkstoffen mittels Bohrlochmethode und Ringkernverfahren. University of Stuttgart, PhD Thesis.
- Shokrieh M.M. (2014): Residual stresses in composite materials. Woodhead publishing in composites science and engineering 48.
- Scholtes B. (2017): Intern teaching script: Festigkeit und Versagen von Konstruktionswerkstoffen.
- Skotarek C., Brückner-Foit A. (2014): Role of bonding defects in a self-reinforced (PURE) under fatigue loading. *FDMDII-JIP* 2014, 102-104.
- Struik L. C. E. (1978): Orientation effects and cooling stresses in amorphous polymers. *Polymer Engineering and Science* 18(10).

Subramanyam Reddy M., Ramesh K. (2016): Photoelastic study on the effect of flow induced residual stresses on fracture parameters. *Theoretical and applied fracture mechanics* 85: 320-327.

Turnbull. A., Maxwell A.S., Pillai. S. (1999): Residual stress in polymers-evaluation of measurement techniques, *Journal of materials sciences* 451-459.

VanLandingham M.R., Villarrubia J.S., Guthrie W.F., et al. (2001): Nanoindentation of polymers: an overview. *Macromolecular Symposia* 167(1), 15-44.

Vishay: Introduction to stress analysis by the photostress method. Tech Note TN-702-2.

Zike S., Mikkelsen L.P. (2014): Correction of gauge factor for strain gauges used in polymer composite testing. *Experimental mechanics* 54, 393-403.

A. Elastic constants of a self-reinforced polypropylene composite.

#### A.1 Unidirectional all-polypropylene composite

A unidirectional all-polypropylene composite is depicted (Figure A.1). Elastic constants from this material will help to assume the elastic properties of the self-reinforced polypropylene composite used in this study. Since this material is orthotropic, nine elastic constants are required:  $E_{11}$ ,  $E_{22}$ ,  $E_{33}$ ,  $\nu_{12}$ ,  $\nu_{13}$ ,  $\nu_{23}$ ,  $G_{12}$ ,  $G_{13}$  and  $G_{23}$ . The coordinate system from figure A.1 is used.

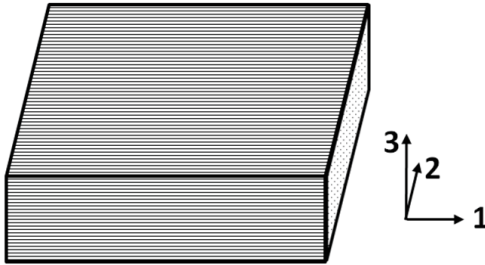


**Figure A. 1: Unidirectional composite and its corresponding coordinate system.**

In [Alcock 2006], the following properties of this structure were measured:

$$E_{11} = 12.95 \text{ GPa}; \quad E_{22} = 1.52 \text{ GPa}; \quad \nu_{12} = 0.38; \quad G_{12} = 0.8 \text{ GPa}.$$

To further characterize this structure, some assumptions are necessary. Due to  $E_{33}$  also being located in the transverse direction of the fibre, it is assumed that  $E_{22} = E_{33}$ . For the same reason, we have  $\nu_{13} = \nu_{12}$  and  $G_{13} = G_{12}$ . A property of common polypropylene was also used for  $\nu_{23}$ , because it does not belong to the fibre direction:  $\nu_{23} = 0.38$ . Lastly, a transverse isotropy is assumed for the shear modulus  $G_{23}$ :  $G_{23} = E_{22} / 2 \cdot (1 + \nu_{23})$ . The elastic properties are listed in Table A.1, the asterisk \* corresponds to assumed and calculated values.

| Sample                                     | Tensile Modulus (GPa) |          |          | Poisson's Ratio |            |            | Shear Modulus (GPa) |          |          |
|--|-----------------------|----------|----------|-----------------|------------|------------|---------------------|----------|----------|
|  | $E_{11}$              | $E_{22}$ | $E_{33}$ | $\nu_{12}$      | $\nu_{13}$ | $\nu_{23}$ | $G_{12}$            | $G_{13}$ | $G_{23}$ |
| Unidirectional all-polypropylene composite | 12.95                 | 1.52     | 1.52     | 0.38            | 0.38*      | 0.38*      | 0.8                 | 0.8*     | 0.55*    |

**Table A. 1: Elastic properties of an orthotropic, unidirectional self-reinforced polypropylene composite.**

## A.2 [0°/90°] Self-reinforced polypropylene composite

Figure A.2 shows a simplified [0°/90°] structure of a self-reinforced polypropylene composite. The real structure used in this study was 4 mm thick and composed of 32 plies of the [0°/90°] fabrics. For the purpose of simplification, the real woven structure is composed of different layers of the unidirectional composite shown in Figure A.1. In order to differentiate the properties of the [0°/90°] woven structure and the unidirectional structure, the following elastic constants were used for the woven structure depicted in Figure A.2:  $E_{11}$ ,  $E_{22}$ ,  $E_{33}$ ,  $\nu_{12}$ ,  $\nu_{13}$ ,  $\nu_{23}$ ,  $G_{12}$ ,  $G_{13}$  and  $G_{23}$ . The following notations were used for the elastic constants of the unidirectional layer (Figure A.1):  $E_{LL}$ ,  $E_{TT}$ ,  $\nu_{LT}$ ,  $\nu_{TT}$ ,  $G_{LT}$ ,  $G_{TT}$ , with L as the longitudinal direction (fibre direction) and T as the transverse direction.

Different elastic constants were measured in this study:  $E_{11} = E_{22} = 5.5$  GPa,  $\nu_{12} = 0.1$ ,  $G_{12} = 0.95$  GPa. Other constants need to be assumed or calculated. Since there is no reinforcement in the direction 3, it was assumed that  $E_{33} = E_{TT} = 1.5$  GPa.

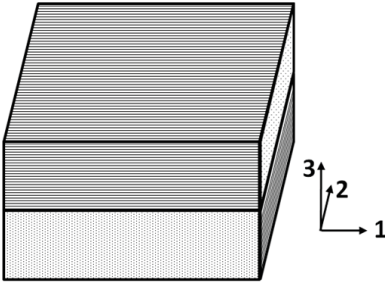


**Figure A. 2: Self-reinforced [0°/90°] polypropylene composite and its corresponding coordinate system.**

### A.2.1. Poisson's ratio $\nu_{13}$ and $\nu_{23}$

To calculate Poisson's ratio for  $\nu_{13}$  and  $\nu_{23}$ , the model in figure A.3 is considered where a composite structure is stretched (Voigt model). Due to the force  $F$  applied on the structure, the sample retracts  $\Delta H$  in the direction 3 with  $H$  the initial height of the structure. In a similar way,  $H_A$  represents the height of the unidirectional layer A and  $H_B$  the height of the unidirectional B. Furthermore, in the case of this structure  $H_A$  equals  $H_B$ .

Following equalities were obtained:

$$\varepsilon_3 = \frac{\Delta H}{H} = \frac{\Delta H_A + \Delta H_B}{H} = \frac{\Delta H_A}{H_A} \cdot \frac{H_A}{H} + \frac{\Delta H_B}{H_B} \cdot \frac{H_B}{H} = \varepsilon_{3A} \cdot \frac{1}{2} + \varepsilon_{3B} \cdot \frac{1}{2}$$

Using Poisson's ratio and considering that the strains in the longitudinal direction of the structure and of each layer are the same, the following results:

$$\varepsilon_1 \cdot \nu_{13} = \frac{1}{2} \cdot (\nu_{LT} \cdot \varepsilon_{1A} + \nu_{TT} \cdot \varepsilon_{1B}) = \frac{1}{2} \cdot (\nu_{LT} + \nu_{TT}) \cdot \varepsilon_1$$

$$\nu_{13} = \frac{1}{2} \cdot (\nu_{LT} + \nu_{TT})$$

In a similar way,  $\nu_{23} = \nu_{13} = 0.5 \cdot (0.38 + 0.038) = 0.38$

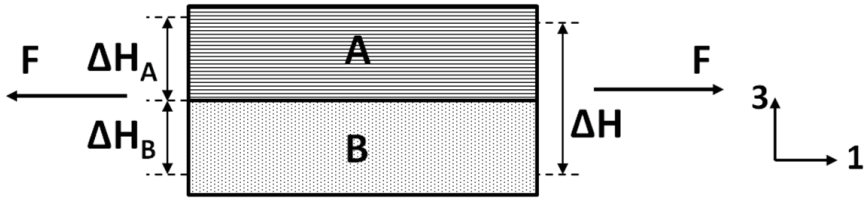


**Figure A.3: Voigt model for a transverse contraction of a two layer system applying force in the longitudinal direction 1.**

#### A.2.2. Shear moduli $G_{13}$ and $G_{23}$ and $G_{12}$

To calculate the shear modulus  $G_{13}$ , a Reuss model was used where a response in series is expected for the structure shown in Figure A.4. The same shear stress  $\tau$  is applied in each layer A and B and the global shear strain  $\gamma$  is the sum of the shear strains of layers A and B -  $\gamma_A$  and  $\gamma_B$ . The following equations are obtained:

$$\Delta L = \Delta L_A + \Delta L_B$$

$$H \cdot \tan \gamma = H \cdot \gamma = H_A \cdot \tan \gamma_A + H_B \cdot \tan \gamma_B = H_A \cdot \gamma_A + H_B \cdot \gamma_B = \frac{H}{2} \cdot (\gamma_A + \gamma_B)$$

Using the Hooke's law, it follows:

$$H \cdot \frac{\tau}{G_{13}} = \frac{H}{2} \cdot \left( \frac{\tau}{G_{LT}} + \frac{\tau}{G_{TT}} \right)$$

After simplification, it reduces to:

$$G_{13} = 2 \cdot \left( \frac{G_{LT} \cdot G_{TT}}{G_{LT} + G_{TT}} \right) = 0.64 \text{ GPa}$$

In a similar way  $G_{23} = G_{13} = 0.64 \text{ GPa}$ . The shear modulus  $G_{12}$  was measured with a tensile test and equals 0.95 GPa.

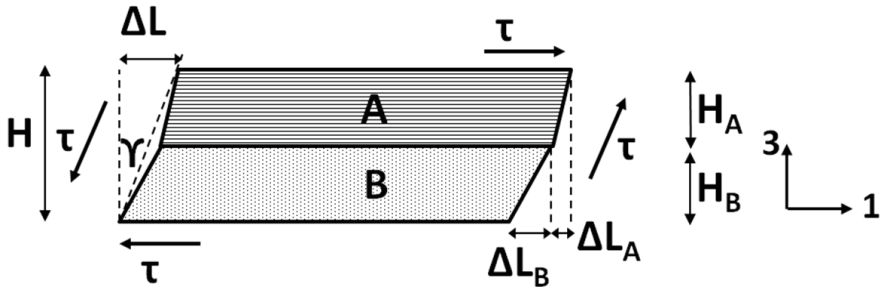


Figure A.4: Deformation of a composite tape following a pure shear stress.

Elastic constants are listed in the following table.

| Sample   | Tensile Modulus (GPa) |          |          | Poisson's Ratio |            |            | Shear Modulus (GPa) |          |          |
|--|-----------------------|----------|----------|-----------------|------------|------------|---------------------|----------|----------|
|  | $E_{11}$              | $E_{22}$ | $E_{33}$ | $\nu_{12}$      | $\nu_{13}$ | $\nu_{23}$ | $G_{12}$            | $G_{13}$ | $G_{23}$ |
| [0°/90°] self-reinforced polypropylene composite | 5.5                   | 5.5      | 1.5*     | 0.1             | 0.38*      | 0.38*      | 0.95                | 0.64*    | 0.64*    |

Table A.2: Elastic constants of a self-reinforced polypropylene composite.



### Acknowledgment

Die vorliegende Arbeit wurde während meiner Tätigkeit am Institut für Werkstofftechnik – Metallische Werkstoffe der Universität Kassel entstanden.

Mein besonderer Dank gilt Herrn Prof. Dr.-Ing. B. Scholtes für die Möglichkeit, die mir gegeben wurde, eine Doktorarbeit mit so vielen Freiheiten durchführen zu dürfen. Desweiteren bedanke ich Ihm für Seine Anmerkungen bei der Durchsicht des Manuskripts.

Außerdem möchte ich Herrn C. Scholtes, A. Fischer, B. Aminforoughi, T. Wegener für die Revision des Manuskripts bedanken.

I would like to express my sincere thanks to all my fellows at the Institut für Werkstofftechnik and the French German and International communities of Kassel for the 6 amazing years I spent here.

Enfin je voudrais remercier Messieurs B. Scholtes, B. Aminforoughi, R. Diederich et Madame H. Hammann pour les quelques conversations en français !





In der Reihe

Forschungsberichte  
aus dem



Institut für Werkstofftechnik  
Metallische Werkstoffe

**U N I K A S S E L**  
der **V E R S I T Ä T**

ist bisher erschienen:

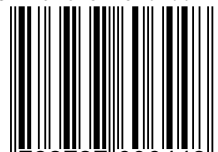
|                           |  |
|---------------------------|--|
| Stefan Jägg               | Rissspitzennahe Eigenspannungen und Ermüdungsrissausbreitung des Stahls S690QL1 bei unterschiedlichen Beanspruchungsmoden                                  |
| Martin Kornmeier          | Analyse von Abschreck- und Verformungseigenspannungen mittels Bohrloch- und Röntgenverfahren   |
| Igor Altenberger          | Mikrostrukturelle Untersuchung mechanisch randschichtverfestigter Bereiche schwingend beanspruchter metallischer Werkstoffe                                |
| Gerd Zöltzer              | Einfluss von Mikro- und Makro eigenspannungen auf das Deformationsverhalten bauteilähnlicher Proben  |
| Ulf Noster                | Zum Verformungsverhalten der Magnesiumbasislegierungen AZ31 und AZ91 bei zyklischen und quasistatischen Beanspruchungen im Temperaturbereich von 20-300 °C |
| Jens Gibmeier             | Zum Einfluss von Last- und Eigenspannungen auf die Ergebnisse instrumentierter Eindringhärteprüfungen  |
| Juijerm Pathiphan         | Fatigue behaviour and residual stress stability of deep-rolled aluminium alloys AA5083 and AA6110 at elevated temperature                                  |
| Martin Krauß              | Zur thermischen Ermüdung der Magnesiumbasislegierung AZ31 und AZ91   |
| Enrique Garcia-Sobolevski | Residual Stress Analysis of Components with Real Geometries Using the Incremental Hole Drilling Technique and a Differential Evaluation Method             |

|                   |   |
|-------------------|---|
| Ivan Nikitin      | Zur Verbesserung des Ermüdungsverhaltens des austenitischen Stahls X5CrNi18-10 im Temperaturbereich 25-600°C durch mechanische Randschichtverfestigungsverfahren              |
| Thorsten Manns    | Analyse oberflächennaher Eigenspannungszustände mittels komplementärer Beugungsverfahren  |
| Anis Cherif       | Analyse und Beurteilung gekoppelter thermisch-mechanischer Prozesse zur Randschichtverfestigung   |
| Thomas Stange     | Positionsgenaue Herstellung einer Fügeverbindung aus Stahl- und Sphärogussvierkanthohlprofilen  |
| Klaus Timmermann  | Zur Schädigungsentwicklung bei der Korrosionsermüdung von Aluminiumbasislegierungen mit definierten fertigungsbedingten Randschichtzuständen                                  |
| Arne Ellermann    | Der Bauschingereffekt bei vergüteten, bainitischen und normalisierten Zuständen der Stähle 42CrMoS4 und 100Cr6  |
| Alexander Grüning | Thermo-mechanisch gekoppelte Experimente zur Beurteilung der Schädigungsentwicklung an Werkzeugen zur Warmumformung   |
| Jens Röse         | Untersuchung der anwendungstechnischen Eigenschaften des Formsprühens von wasserbasierten Trennstoffen in Abhängigkeit der Applikationstechnik für den Leichtmetall-Druckguss |
| Siegfried H. Wüst | Zum Temperaturwechselverhalten von Werkzeugstählen für das Druckgießen  |
| Markus Lebsanft   | Untersuchung des Wechselverformungsverhaltens von Werkzeugstählen bei isothermer und thermomechanischer Ermüdung im Temperaturbereich von RT bis 650 °C                       |
| Ralf Weber        | Auslegungskonzept gegen Volumenversagen bei einsatzgehärteten Stirnrädern   |
| Wolfgang Römer    | Tragfähigkeitsberechnungen für Kehlnähte auf Grundlage experimentell gestützter Werkstoffmodellierung   |
| David von Mirbach | Beitrag zur Ermittlung von Eigenspannungen nahe der Streckgrenze mittels mechanischer Prüfmethode   |
| Kerstin Anten     | Zum Verformungsverhalten der Magnesiumknetlegierung AZ31 unter homogener und inhomogener Belastung  |

|                 |   |
|-----------------|---|
| Andreas Nau     | A Contribution to Enlarge the Application Limits of Residual Stress Analyses by the Hole-Drilling and the Ring-Core Method  |
| Philipp Krooß   | Einfluss elementarer Mechanismen auf das funktionale Ermüdungsverhalten von Formgedächtnislegierungen   |
| Alexander Liehr | Beitrag zur randnahen Struktur- und Eigenspannungsanalyse in polykristallinen Werkstoffen mit energiedispersiven röntgenografischen Verfahren   |
| Django Baunack  | Induktives Stumpfschweißen metallischer Mischverbindungen   |
| Florian Brenne  | Selektives Laserschmelzen metallischer Materialien. Einfluss von Prozessparametern und Miniaturisierung auf Mikrostruktur und mechanisches Verhalten geometrisch komplexer Strukturen |
| Arnaud Magnier  | Residual stress analysis in polymer materials using the hole drilling method – basic principles and applications  |

---

ISBN 978-3-7376-0644-8



9 783737 606448 >